Physics and Technology of small Josephson junctions

Simon Schmidlin

Department of Physics

Royal Holloway, University of London

A thesis submitted to the University of London for the

Degree of Doctor of Philosophy

October 27, 2013

Supervisor: Dr Phil Meeson.

Advisor: Dr James Nicholls.

Moderator: Dr Nikolas Kauer.

Examiners: Professor Victor Petrashov and Dr Richard Haley.

To my parents

Abstract

The recent interest in developing highly controllable quantum bits (qubits) based on superconducting circuits makes it necessary to get a deeper understanding of the physics of small Josephson junctions. Such devices have to be wisely engineered and well isolated from the noisy environment to observe non-classical physics. In this thesis, a real-time noise analysis was implemented by an autocorrelation calculation to identify the type of environmental effects affecting a superconducting circuit. This was used during switching current measurements of small Josephson junctions to track the effects of unwanted signals and identify their frequency components. The temperature dependence of the switching current distribution was used to further characterise the small Josephson junctions. Furthermore the fabrication of small Josephson junctions is further developed by analysing the reliability and reproducibility of them. A systematic approach is shown to solve typical fabrication problems for example identifying and reducing mechanical stress between resist layers. As Josephson junctions show quantum mechanical effects on a macroscopic scale they are used in a wide range of applications especially in superconducting circuits.

The commissioning of a dilution refrigerator is described which includes the programming of a full control of the valve and pumping system to perform a smooth cool down where all important parameters can be monitored remotely. A low temperature setup was built to create a noise suppressed environment to perform fundamental device characterisation and measurements. The main development in creating such an environment was the design and production of low temperature microcoaxial filters which were made

of stainless steel to block the high frequency components of black body radiation from room temperature. These filters show a predictable frequency dependence of the damping which was also verified.

DECLARATION

I confirm that the work presented in this thesis is my own. Where information has been derived from other sources, I confirm that this has been indicated in the document.

Simon Schmidlin

Contents

List of Figures

List of Tables

Chapter 1

Introduction

This thesis focuses on the fabrication and measurement of small Josephson junctions. Small tunnel junctions are characterised by a very low capacitance such that the charging energy ($E_c \equiv e^2/2C_J$) is considerably larger than the thermal energy $k_B T$ at the experimental temperature ($C_J \lesssim 50\,\text{fF}$ for $T = 20\,\text{mK}$). Furthermore, the tunneling resistance of a small Josephson junction has to be around the quantum resistance $R_Q \equiv h/4e^2 = 6453.2\,\text{k}\Omega$ to avoid quantum fluctuations [1]. The study of such devices is interesting because they are used in a wide range of applications, among which the realisation of superconducting qubits is one of the main implementations. Low-frequency charge fluctuations are one of the main issues for small Josephson junction measurements as they are more sensitive to charge noise due to their small size and it became even more relevant after the introduction of superconducting qubits. A lot of effort has been invested in studying the cause and effect of fluctuations in those systems and a detailed description is still not available.

In this thesis, the voltage-current curves and the switching probability measurements of a small Josephson junction are analysed and the relevant information extracted. A new technique was implemented to assess the environmental noise on this type of device. This new technique was successfully applied to a small Josephson junction. This allows to calculate the autocorrelation of the switching events in real time and allows to directly

observe the effect of noise reduction onto the autocorrelation and also the relevant frequency component of the noise source. The results are discussed in chapters 5 and 6.
The project also required the full commissioning of a new dilution refrigerator. A detailed description of the installed and tested setup of the measurement can be found in chapter 4.
Chapter 2 gives an overview of the basic theory of a Josephson junction in different damping limits as well as the effect of temperature on the switching probability of such a junction.
The original plan of this thesis was to detect the effect of quantum phase slips [2] in either a nanowire, which is embedded in a highly resistive environment [3], or in an array of small Josephson junctions [4]. This project was in collaboration with the National Physical Laboratory (NPL) in Teddington (United Kingdom) under the guidance of Dr Carol Webster. In order to learn the basic processes needed to fabricate such a device, I spent 3 months at the University of Jyvaskyla (Finland) in the group of Dr Konstantin Arutyunov. I then established a fabrication process for an array of small Josephson junctions in the cleanroom facility at Royal Holloway University of London. Chapter 3 will explain in the detail the fabrication and room temperature testing of Josephson junctions.
I will first give an introduction and overview of the relevant field of superconducting devices that have Josephson junctions as the basic components. This includes a short introduction to superconductivity and an extended description of the relevant applications.

1.1 Superconductivity

Superconductivity is a quantum-mechanical effect which is even present on a macroscopic scale and therefore special in the sense that it does not disappear when the system size is enlarged. The phenomenon of superconductivity is characterized by an exactly zero electrical resistance and a complete ejection of any externally applied magnetic field from the

inside of the superconducting material. It was first discovered in 1911 by H. Kamerlingh Onnes [5] but it took until 1957 before a microscopic theory was laid out by Bardeen, Cooper and Schriefer (BCS theory) [6]. The fundamental cause of this state is the attractive interaction of the electron-phonon coupling which is able to overcome the screened repulsive Coulomb interaction between two electrons. In this way two electrons can, under certain spin and momentum configuration, form a so-called Cooper pair. The Cooper pairs can carry an electrical current without dissipation, which is the defining property of a superconductor. The BCS theory indicates that a gap in the density of electron states starts to appear at the Fermi surface at the critical temperature. The energy needed to create a single Cooper pair is given by $2\Delta(T)$ in terms of the superconducting gap $\Delta(T)$. This attractive coupling opens up a gap in the density of states for the quasiparticle excitations in the range of $[-\Delta, \Delta]$ for which no quasiparticle states are available and diverges at $E = |\Delta|$, see figure 1.1 a). An important characteristic length scale in superconducting materials, especially at interfaces between different type of materials, is the so-called coherence length which is the length scale within which the density of Cooper pairs regains its bulk value. The coherence length of pure aluminium is approximately 200 nm which compares to a typical mean free path of an electron in the normal conducting state at low temperatures of 30 nm [7].

1.1.1 The Josephson equations

In 1962, Brian David Josephson stated two basic equations that describe the dynamics of a Josephson junction [10]. The first equation describes the relation between the voltage $V(t)$ across the junction and the dynamics of the gauge-invariant phase difference $\phi(t)$ of the two superconducting electrodes

$$V(t) = \frac{\hbar}{2e}\frac{\partial\phi(t)}{\partial t}, \tag{1.1}$$

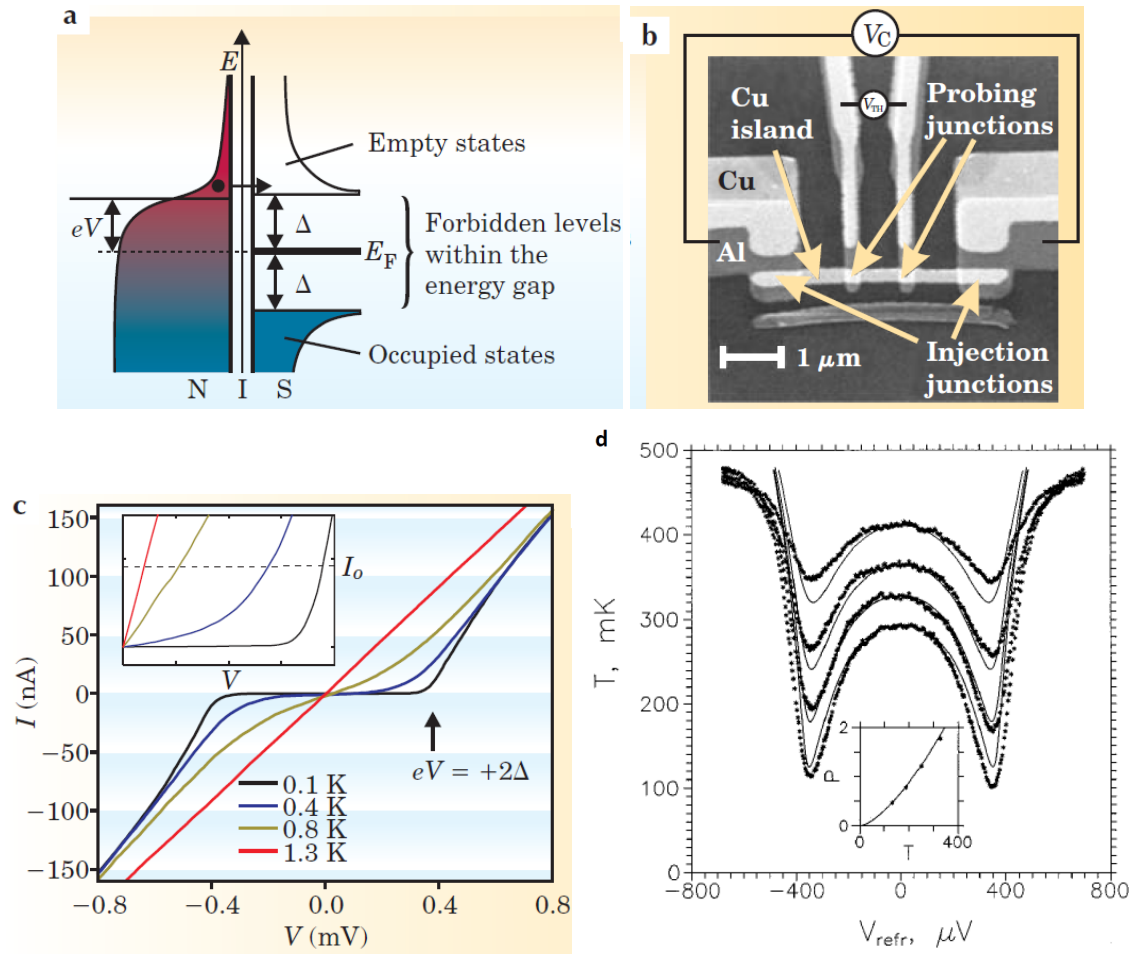

Figure 1.1: a) In this energy-level diagram of a NIS tunnel junction, the energy gap around the superconductor's Fermi level forbids electrons from tunneling between the normal metal and the superconductor at the energy levels shown. A bias voltage V across the junction separates the chemical potentials by eV. b) A hybrid electronic cooler is formed from two NIS junctions connected in series: The central part is a copper island, coupled to NIS probing junctions and large NIS injection junctions. The thermometer's voltage V_{TH} is measured across the NIS probing junctions in a circuit biased at constant current. The control voltage V_c is applied across the injection junctions. c) The current-voltage curves indicate the monotonic decrease in voltage as the temperature rises in such a device biased at constant current I_0, an effect that makes the device a thermometer. Taken from [8]. d) SINIS refrigerator performance at various starting temperatures. Dots are the experimental data, while the solid lines show the theoretical fit with one fitting parameter for all curves. The inset shows the cooling power P [pW] from the fits (dots). Taken from [9]

where e is the elementary charge and $\hbar$ is the reduced Planck constant. The superconducting current I_s which can be carried by the Josephson junction depends non-linearly on the phase difference across it and is limited by a critical current I_c which is described by the second Josephson equation

$$I_s(t) = I_c \sin(\phi(t)). \tag{1.2}$$

The critical current itself depends on the temperature as well as the magnetic field in the case of a SQUID design (see figure 1.2). These two equations describe the full dynamics of a Josephson junction in a remarkably simple way and will be discussed in detail in chapter 2.

1.2 The Josephson effect and flux quantisation

A Josephson junction is formed of two superconducting leads which are separated by a weak link. This link isolates the two leads and only allows Cooper pairs to tunnel across it [1]. This device is of fundamental interest as it shows a non-linear relation (the Josephson effect) between the gauge-invariant phase difference of the two superconductors and the Cooper pair tunneling current. The gauge-invariant phase of the superconducting state is connected to the momentum of the condensate and is defined via the line integral of the vector potential between two points. The simplest way to see the effect of the vector potential is by considering a closed superconducting loop which is interrupted by two Josephson junctions, a so-called Superconducting Quantum Interference Device (SQUID), see left panel in figure 1.2. By applying an external magnetic field onto the loop it can be shown that the total magnetic flux in the ring is quantized in integer values of the flux quantum $\Phi_0 = h/2e$. This quantization arises from the requirement that the wavefunction of the superconducting state has to be single valued. This effect can be seen for a

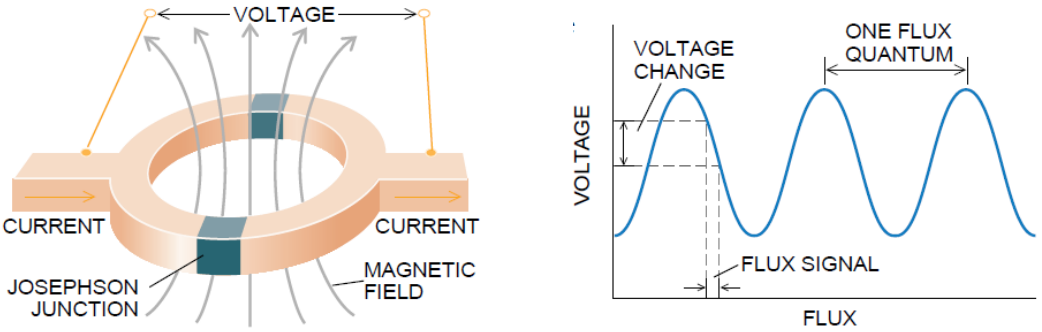

Figure 1.2: Left: The direct-current SQUID. A bias current creates a voltage over the two electrodes as soon as it exceeds the critical current. Right: The critical current depends periodically on the magnetic flux with a period of one flux quantum. Taken from [11].

SQUID if a bias current is applied and a voltage appears as soon as this current exceeds a critical current. An induced magnetic flux in the ring causes a periodic dependency of the critical current as shown in the right panel of figure 1.2. These two effects (nonlinearity and flux quantisation) are the basic properties of Josephson junctions and are often the main ingredients to build a superconducting circuit.

1.3 Quantum effects in small Josephson junctions

As superconductivity is a quantum mechanical phenomenon it is necessary to describe the Josephson junction in the Hamiltonian form. So far only the gauge-invariant phase has been introduced but this only describes the potential energy and it is therefore necessary to identify a canonical conjugate variable to it. This is the polarization charge on the junction and is used to describe the kinetic energy that corresponds to the charging energy of the capacitor. After defining a commutation relation between those two operators, a total Hamiltonian for the Josephson junction can be written down. Hamilton's equations then produce the Josephson equations. The eigenstates and energy spectrum of this Hamiltonian can be calculated analytically in two different limits of the relevant energy scales. Figure 1.3 shows the energy diagram in the two limits. In the case where the Cooper pair tunneling energy E_J (Josephson energy) is much larger than the charging

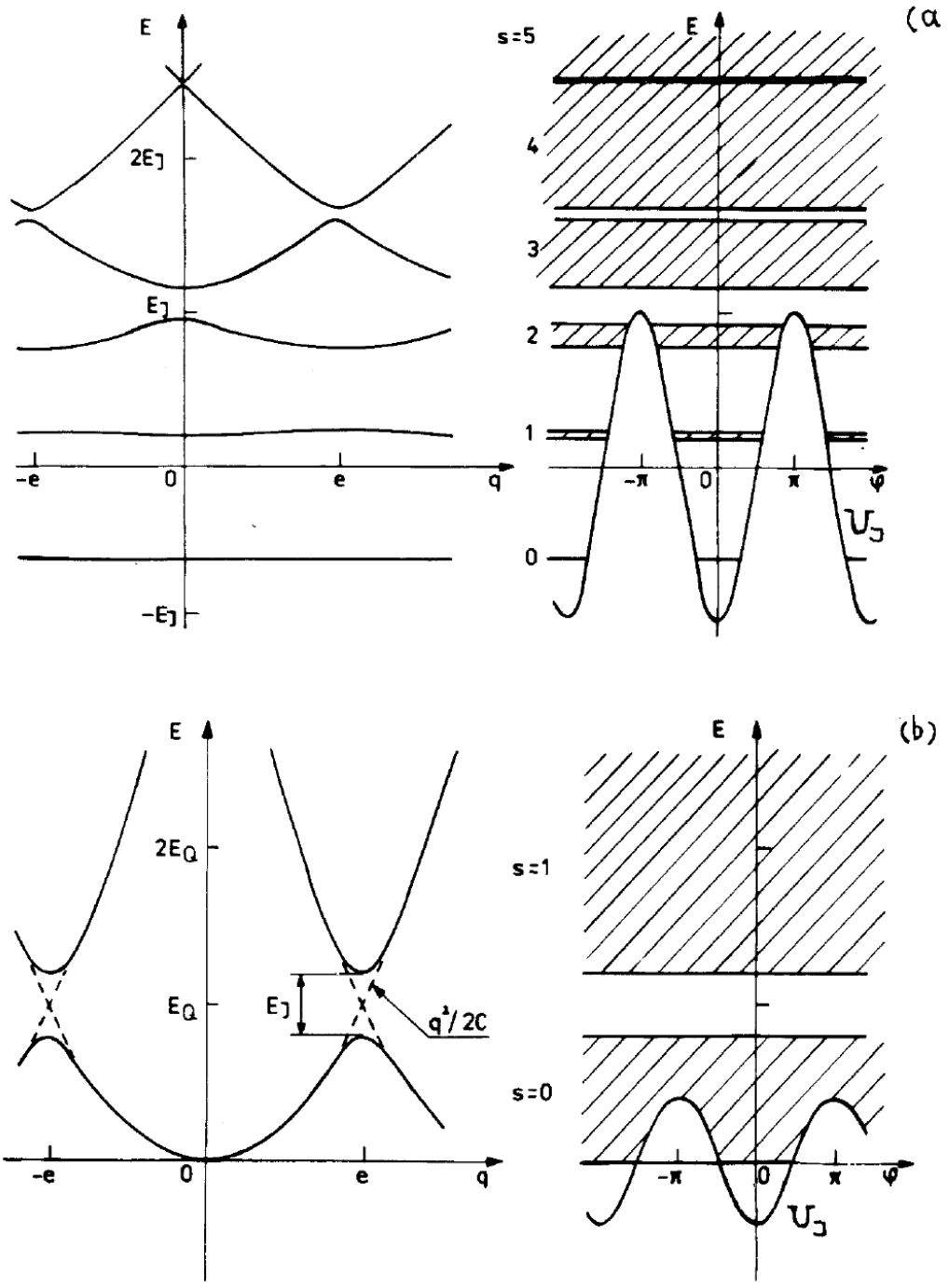

Figure 1.3: Energy level diagram of a Josephson junction in the RCSJ-model for two distinct limits with $E_Q \equiv E_c$. a) Tight-binding limit $E_Q/E_J = 0.1$. Narrow energy bands are closely located to energy levels of a harmonic oscillator. b) Nearly free-electron limit $E_Q/E_J = 2.5$. The parabolic dispersion relation shows the avoided crossing near $(2n+1)e$ values. The diagrams on the right hand side show the band structure corresponding to the energy levels on the left diagrams. Taken from [12].

energy E_c of the capacitor the Hamiltonian is in the "tight-binding limit" and it is useful to describe the solutions in terms of the phase variable. In this limit the Hamiltonian is the one of a harmonic oscillator in the phase variable with 2π periodic solutions. In the opposite limit where the charging energy is much larger than the Josephson energy it is easiest to describe the system in the polarisation charge variable as the Hamiltonian is in the "nearly free-electron limit". Again, the system is similar to a harmonic oscillator, this time in terms of the polarization charge, but with the difference that the $2e$ periodic solutions show an avoided crossing at odd numbers of the charge variable, i.e. $2n + 1$. An odd number means that the two charge states with $2ne$ and $(2n + 2)e$ are separated by the Josephson energy at $2n + 1$. The energy spectrum is divided into different bands due to the avoided crossing at the degeneracy points and within each band the electrons are weakly coupled and almost free.

1.4 Applications of tunnel junctions with superconductors

The very first applications of tunnel junctions was a SQUID that builds a highly sensitive magnetometer and is used in a wide range of applications to detect magnetic fields (the critical current of the loop depends periodically on the induced magnetic flux) [11].
Another important application is the definition of the Volt by using a large array of Josephson junctions that are excited by microwaves as the array acts as a voltage-to-frequency converter (this works because frequency is already precisely measurable). An extended review about the voltage standard can be found in chapter 11 of reference [13]. At the moment, a similar experiment tries to use a dual effect to define the electrical current in a more precise way based on a theoretical description in 2006 by Mooij and Nazarov [2] (coherent quantum phase slips). The first experimental results look promising [3, 4]. The realisation of a current standard based on an array of small Josephson junctions is chal-

lenging as the predicted duality can only be obtained if the consisting junctions are small and at the same time the electric environment shows a high impedance. This makes it necessary to study the fabrication and measurement of small Josephson junctions.

Besides the already mentioned superconducting-insulating-superconducting (SIS) version of the Josephson junction it is possible to build a superconducting-insulating-normal conducting junction (NIS). The schematic of the bandstructure for a NIS junction is shown in figure 1.1 a). This figure shows the well-known Fermi-Dirac distribution of the electrons in the normal conducting electrode as well as the gap in the density of states in the superconducting electrode. This type of junction can be used to measure the superconducting density of states via the differential conductance [7]. However the main applications are local electron thermometry and cooling or heating of the normal conducting island and of whatever is attached to it, see figure 1.1 b). The thermometry is based on the temperature dependent voltage-current curve of NIS junctions as can be seen in figure 1.1 c) which shows, for a fixed bias current I_0, a decrease of the voltage across it as the temperature is increased. By applying a bias voltage below the superconducting gap ($e\,|V| < |\Delta|$ only the hot electrons can tunnel into empty states of the superconducting electrode. On the other hand, no quasiparticle can be created to tunnel from the superconducting- to the normal conducting electrode as they lie below the Fermi-level E_F. This indicates a cooling effect with a heat flow from N to S. As soon as the applied voltage exceeds the gap voltage the direction of the heat flow changes because the Fermi-level exceeds the superconducting gap and there is no more selective tunneling of the hot electrons.

By adding two NIS junctions in series the associate cooling power is doubled. Such a device is known as SINIS. Figure 1.1 d) shows the electron temperature of the normal-metal island N as a function of the applied voltage V_{ref} for different starting temperatures. The inset shows the cooling power in pW for the different starting temperatures [9]. This measurement clearly shows the cooling effect given by the selective tunneling of the hot electrons of the island N. Notice that the heat current is independent of the sign of the

bias voltage which is different from the Peltier effect [7]. This type of micro refrigerator is highly efficient in lowering the electron temperature of the normal-metal island whereas the lattice temperature is hardly affected by the cooling as it is strongly coupled to the substrate of the device. Part of the research at the moment in this field is to electrically isolate the sample from the cooler structure (in order to only perform electronic measurements on the sample) but keeping the thermal coupling to the island N. This is achieved by putting the cooler on bulk and having an additional, micromachined membrane on top of which devices can be fabricated. The membrane itself is cooled with normal metal leads which are extensions of the island N [7]. As will be seen later in the experimental result chapter 5 and 6, some small Josephson junctions were fabricated on top of a SiN membrane as they are part of a different ongoing research project which focuses on the characterisation of the suspended membrane. The characterisation of the membrane is not part of this thesis but the realisation of on-chip refrigeration by SINIS junctions is mentioned for completeness.

A similar, theoretically predicted device is the Brownian refrigerator which shows an almost identical cooling power but instead of depending on the the bias voltage it depends on the temperature of a nearby resistor. So far, this has not been experimentally measured [14, 15]. An extended review about mesoscopic thermometry and refrigeration can be found in references [16, 17].

Another application is the use of a NSN junction as an accurate electron pump [18].

In this device an ultra small NSN junction is biased by a constant voltage V to break the left-right symmetry ($k_BT < e\,|V| < |\Delta|$), and an additional gate electrode allows the application of a DC offset voltage with a superposed sinusoidal signal to induce charges onto the superconducting island. The DC offset voltage makes it possible to operate the device at an optimal working point whereas the AC signal relates the current I through the device to the frequency f as $I = Nef$ for an integer number N of injected electrons per cycle. This charge pump is an alternative candidate to the quantum phase slip device

for a current standard in metrology. Several advantages, due to the implementation of a superconducting island, make this configuration promising compared to normal metal tunnel junctions used as an electron pump. First, it is a simple device, as it only consists of two junctions. Second, the operational frequency is higher as the superconductor and the small dimension of the junctions prevents uncontrolled cotunneling. Third, the DC offset gate voltage can be used to compensate the influence of background charges, which is probably the main advantage over any other single-electron pump as background chargers are usually the limiting factor of charge-based devices. On the other hand, the drawback of the superconducting charge pump is the subgap leakage that contributes to the transferred current.

1.5 Superconducting quantum bits

As mentioned in section 1.2, flux quantisation and Josephson tunneling can be used to build a so-called superconducting quantum bit (sQubit). A qubit is analogous to the classical bit but instead of taking two possible values (0 and 1) it can also take any superposition state. The realisation of such a qubit can only be done by describing the system in a quantum mechanical state. As a simple visualisation of a single qubit state one can use the *Bloch sphere* representation as shown in figure 1.4. The two poles of the Bloch sphere correspond to the pure $|0\rangle$ and $|1\rangle$ states and any other state $|\Psi$ can be described by the two polar angles ϕ and θ. The Bloch sphere model is helpful in understanding the effect of quantum operations on qubits [7]. There are three fundamental types of superconducting qubits: charge, phase and flux [21], see figure 1.5. The charge qubit was the first realisation of a superconducting qubit by Nakamura in 1999 [22]. It consists of a SQUID loop which is capacitively coupled to a gate onto which a gate voltage can be applied in order to change the polarisation charge. This so-called *Cooper pair box (CPB)* is operating in the charging limit $E_J \ll E_c$. As the polarisation charge is the canonical conjugate

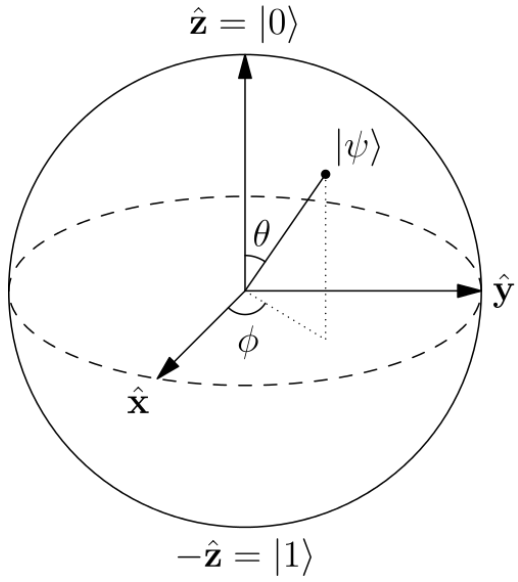

Figure 1.4: The Bloch sphere as a simple representation of a single quantum bit. Each point on the surface represents a pure state defined by the azimuthal- (ϕ) and polar angle (θ) of the spherical coordinates. The North and the South pole are chosen to represent the states $|0\rangle$ respectively $|1\rangle$. Taken from [19].

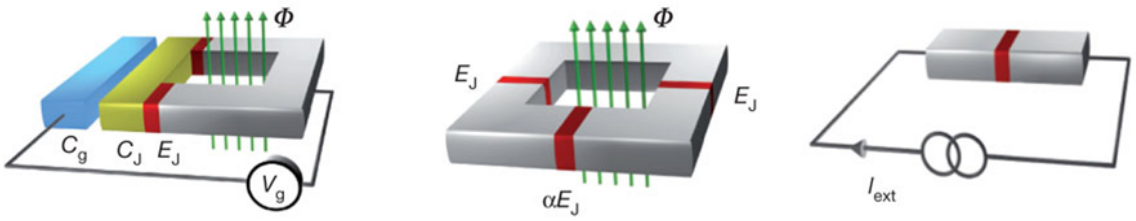

Figure 1.5: Left: A Cooper-pair box biased by a gate voltage V_g and implemented in the charge regime, $E_J/E_c \ll 1$. The SQUID loop provides an effective Josephson coupling energy tuned by the threading magnetic flux Φ. The blue, gold and grey components denote, respectively, a plate of the gate capacitor, a superconducting island acting as a box of Cooper pairs, and a segment of a superconducting loop. Each red component denotes the thin insulating layer of a Josephson junction. Middle: A superconducting loop interrupted by three Josephson junctions and implemented in the phase regime, $E_J/E_c \gg 1$. The two identical Josephson junctions have coupling energy E_J and capacitance C, while both the Josephson coupling energy and the capacitance of the smaller junction are reduced by a factor α, where $0.5 < \alpha < 1$. The three-junction loop is biased by a flux Φ such that $f \equiv \Phi/\Phi_0 \approx$1/2. Right: A Josephson junction biased by a current I_{ext}, which is also implemented in the phase regime and has a much larger ratio E_J/E_c. Taken from [20].

of the gauge-invariant phase they are subject to Heisenberg's uncertainty principle which means, in this limit, that the charge is a good quantum number whereas the phase has large quantum fluctuations, which explains the name of the charge qubit. The CPB is particularly sensitive to low-frequency charge noise as it is based on the direct manipulation of the charge which is still an outstanding problem [7] due to control of the environmental charge noise although different developments of more advanced charge qubits have greatly reduced this effect (e.g. the Fluxonium [23]).

The flux qubit works in the opposite limit, namely $E_J \gg E_c$. It consists of a superconducting loop interrupted by one [24] or three [25] Josephson junctions. The quantum states are the magnetic flux pointing up or down and are caused by the superconducting current flowing in either clockwise or anticlockwise direction. By surrounding the flux qubit by a SQUID one can manipulate and readout the state of the qubit via the flux. The energy spectrum of a Josephson junction in this limit is similar to that of a harmonic oscillator (see appendix 7.1), i.e. the energy levels are almost equally separated which would make it impossible to only use two quantum states necessary for any qubit realisation. By adding an extra non-linear inductance into the loop of the qubit the potential has an asymmetric double-well shape with a non-linear energy spectrum. This additional non-linear inductance is either realised by the inductance of the loop in the case of the single Josephson junction or by the inclusion of two larger junctions in the loop. The three junction design is presently more widely used.

The simplest possible implementation of a superconducting qubit is the phase qubit as it only consists of a current biased Josephson junction [26]. The original, almost harmonic potential becomes more anharmonic by biasing the junction with a DC current. The state of the qubit is manipulated by applying microwave pulses on top of the DC current which are in resonance with the energy splitting of the two relevant eigenstates. To read out the state of the phase qubit, short DC pulses are applied. If a voltage can be measured over the junction after the DC pulse has been applied, the phase qubit was in the excited state and

the absence of a voltage over the junction indicates the ground state of the phase qubit. The main advantage of the superconducting qubit is its relatively good scalability. On the other hand, the relatively short time over which the quantum state loses its coherence (*decoherence times* are in the range of 10-100 µs [27–29]) limits the number of useful operations which can be performed. The short coherence time is the main limitation of superconducting qubits, because strong interaction between the system state and the environment makes them strongly affected by noise. The new technique which was implemented in this thesis (see chapter 6) assesses the environmental noise on this type of device.

1.5.1 Quantum computing

In 1965, Gordon Moore, who co-founded the *Intel Corporation*, observed that the number of transistors on a chip will double every 18-24 months [30]. Moore also expects that this rapid miniaturisation will come to an end by 2020 as the effects of quantum physics become more and more important. This happens either because the size of the transistors become comparable to the *de Broglie wavelength* of electrons such that *Ohm's law* no longer holds or because the size of the transistor becomes comparable to the size of an individual atom [7]. Besides this inevitable limit of miniaturisation, a general curiosity of how a computer could run according to the laws of quantum mechanics was discussed by Feynman in 1982 [31]. Soon after Feynman's proposal, a theoretical outline on the basic principles of a quantum computer was published by David Deutsch [32]. The main idea was to encode the information itself as quantum states and he introduced the notion of a universal quantum computer. So far, quantum computing was only an idea, but a breakthrough was made in 1994 by Peter Shor who showed that the factorising of a large number could be performed in a shorter time by a quantum computer compared to the classical algorithm [33]. Another important quantum algorithm was formulated by Lov Grover in 1996 which concerns the efficient searching of an unsorted database which

would need less operations compared to the classical algorithm [27, 34]. It has to be mentioned that the numbers of qubits required to be useful for such a quantum algorithm is of order 1000 [27] which is much larger than what exists today in this field. However, a simple test was performed of Shor's algorithm on a nuclear magnetic resonance (NMR) system [35].

1.5.2 Quantum optics using superconducting circuits

Josephson junctions can be thought of as artificial atoms due to the unequal spacing of hydrogen-like energy levels given by the non-linear inductance. It is therefore possible to implement atomic-physics and quantum-optics experiments with superconducting circuits [20]. The main differences between such artificial atoms and natural ones are the different energy scale, the fixed location of the artificial atom, and its coupling strength to the environment, which is both stronger and tunable for the superconducting implementation. Besides the relatively large freedom of designing the parameters of the Josephson junction, superconductivity allows low dissipation and external noise can be greatly suppressed.

By coupling the artificial atom to a quantised electromagnetic field, which can be realised by fabricating a coplanar waveguide next to the Josephson junction (or CPB) it is possible to perform cavity quantum electrodynamics (cQED) on a chip, see figure 1.6. The experiments follow the same models and ideas as already known from quantum optics [20] which include: Rabi oscillations, selecting quantum transitions, state population inversion, lasing, different types of cooling (Doppler-, Sisyphus-, sideband- and evaporative cooling), photon generation, quantum state tomography, squeezed state generation and so on. An excellent review can be found in reference [20].

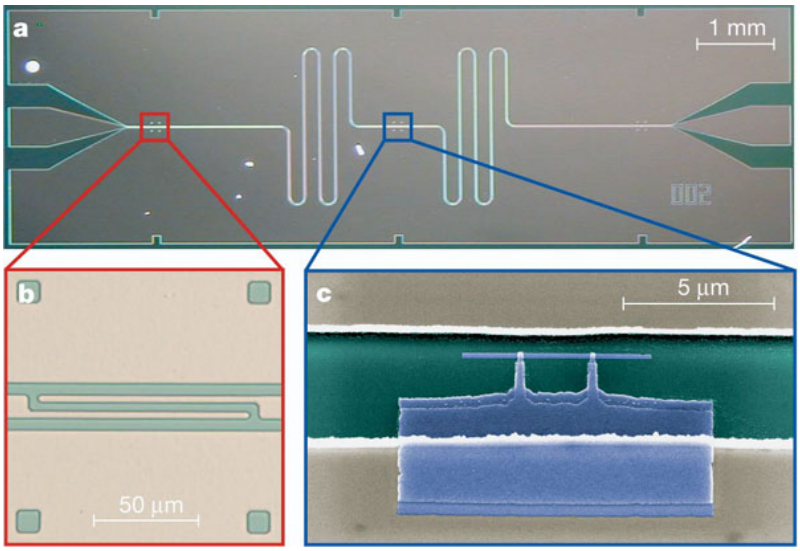

Figure 1.6: a) The superconducting niobium coplanar waveguide resonator is fabricated on an oxidized silicon chip. The length of the meandering resonator is 24 mm. It is coupled by a capacitor at each end of the resonator (see b) to an input and output feed line, fanning out to the edge of the chip. b) The capacitive coupling to the input and output lines and hence the coupled quality factor Q is controlled by adjusting the length and separation of the finger capacitors formed in the centre conductor. c) False colour electron micrograph of a Cooper pair box (blue) fabricated onto the silicon substrate (green) into the gap between the centre conductor (top) and the ground plane (bottom) of a resonator (beige). The Josephson tunnel junctions are formed at the overlap between the long thin island parallel to the centre conductor and the fingers extending from the much larger reservoir coupled to the ground plane. Taken from [36].

1.6 Experimental issues

There are some experimental issues regarding superconducting circuits. First of all is the difficult fabrication process especially of small Josephson junctions as needed, for example, for superconducting electron pumps and charge/flux qubits. Small Josephson junctions ($\ll 1\,\mu m^2$) have to be fabricated using electron-beam lithography and a shadow-evaporation technique which is still challenging to fully control (for example, the oxidation to form an insulating layer between the two superconducting electrodes). The fabrication of larger junctions as needed for the phase qubit or a range of other devices is more or less a standard procedure, as photolithography can be used instead of the much more complicated and expensive electron-beam lithography.

On the measurement side, one has to keep in mind that most of the superconducting circuits have to be cooled down to cryogenic temperatures (mK range) to make them superconducting, to reduce the effect of thermal fluctuations and to reach the ground state in the case of qubits. But although dilution refrigerators for this temperature range are commercially available, seting them up is still not a straightforward task and depends on the what the experiment needs. The main issue for superconducting circuits which contain Josephson junctions is the electromagnetic environment, especially low-frequency charge offsets and charge fluctuations [7,21]. Low-frequency bias currents (from DC to the MHz range) usually have low-pass filters installed at different temperature stages of the dilution refrigerator which are usually made of LC, RC and/or skin-effect filters. The overall attenuation is typically 200 dB [21] which therefore needs relatively large input powers on the input lines. Furthermore as the measurement leads are the main connection between the room temperature stage and the device under test, they have to be well thermalised. Another possibility to avoid this low-frequency noise is to make the superconducting circuits less sensitive to offset charges or magnetic flux by redesigning the circuit (adding

L, C and R components) and optimising the measurement process (e.g. using sweet-spot and echo techniques). But this always comes with a drawback, for example, more equal energy spacings in the spectrum or slower read-out times. The main issue with this type of low-frequency noise is that their cause is mostly unknown. For example, it is still not known today what the mechanism of 1/f magnetic-flux noise is [21]. This issue becomes critical for superconducting qubits as quantum applications rely on coherent quantum states which decohere due to the environmental noise. In this content, the key parameter is the dephasing time [27] which, together with the required time to perform an operation, sets the limit of the maximal number of quantum operations before the quantum state loses its coherence. This is at the moment in the range of $\approx 10^{-8}/10^{-10} = 10^{2}$ for superconducting qubits which is still far away from any possible implementation of any quantum algorithm [27, 37].

1.6.1 Fluctuations and correlations

Electrical noise in any circuit limits the accuracy for detecting a desired signal but can even destroy the quantum mechanical coherence of a system. This is already an important motivation to study the cause and effect of noise. Furthermore, noise can also contain information about the interaction between the quantum system and the (classical) environment and is especially important when performing a quantum measurement. In this context a fundamental discovery is the *fluctuation-dissipation theorem* [38, 39] which states that any dissipative process is accompanied by fluctuations. Moreover it states that the linear response of a system in non-equilibrium is connected to the statistical fluctuation when the system is in its equilibrium [7].

The main types of current fluctuations for such systems are thermal noise, shot noise, vacuum fluctuations, flicker noise (1/f-noise) and resonant correlations [7]. Each of these fluctuations offers information about the system and its interaction to the environment. For example, the shot noise in electrical circuits, which is due to the discreteness of elec-

trons, can tell something about the transmission distribution of a two-terminal geometry such as a diffusive wire or NIS tunnel junction. The cross-correlation in multiprobe geometries can also reveal some information about the charge transport properties in the device. Furthermore the study of higher moments of current fluctuations will ultimately lead to a full counting statistics (FCS). The point in describing a probability distribution of charge fluctuations via higher moments is that they show how a given distribution deviates, unlike Gaussians which only have an average value and a variance [7]. Experimentally, the measurement of the FCS is far away from being accomplished as already measuring the third cumulant was a difficult task [40–42].

Chapter 2

Theoretical and experimental background

2.1 Josephson Junction

An SIS Josephson Junction (JJ) consists of two superconductors (S) separated by a thin, electric insulating barrier (I). Depending on the thickness of the barrier it is possible that the macroscopic wave functions of each superconducting lead overlap and Cooper pairs can coherently tunnel through it. This effect was predicted by B. D. Josephson in the year 1962 [10], see section 2.1.1. A JJ can be described by an equivalent circuit consisting of a capacitor in parallel with a resistor and a non-linear inductor as described in section 2.1.3 together with section 2.1.4 and 2.1.5.

Section 2.2 is fundamental for the interpretation of the experimental data as it describes the theoretical model of the switching current measurement. The theoretical background is needed to understand the current experimental implementations of small Josephson junctions which is described in section 2.4.

2.1.1 Josephson equations

There are two fundamental equations, known as *Josephson equations*, that describe the basic behaviour of a Josephson junction. The first Josephson equation gives the relation

between the Josephson supercurrent $I_s(t)$ and the gauge-invariant phase $\phi(t)$ across the two macroscopic wave functions in a weak-linked JJ

$$I_s(t) = I_c \sin \phi(t), \tag{2.1}$$

with

$$\phi(t) = \phi_2(t) - \phi_1(t) - \frac{2\pi}{\Phi_0} \int \vec{A} \cdot d\vec{s}. \tag{2.2}$$

The integration of the vector potential $\vec{A}$ in equation (2.2) is from one electrode (with phase $\phi_1(t)$) of the weak link to the other one (with phase $\phi_2(t)$). The critical current I_c is a time independent constant which is affected by temperature and describes the maximum current that can be carried by the supercurrent. The full temperature dependence of the critical current is given by the so called Ambegaokar-Baratoff formula [43, 44]

$$I_c = \frac{\pi \Delta(T)}{2eR_n} \tanh\left(\frac{\Delta(T)}{2k_B T}\right), \tag{2.3}$$

which connects the critical current to the BCS energy gap $\Delta(T)$ and the tunnel resistance of the normal state R_n. The elementary charge e and the Boltzmann constant k_B were used in equation (2.3). It is important to stress that the DC resistance of a tunnel barrier with a uniform cross section is inversely proportional to its cross section A (i.e. $R_n \propto 1/A$). This means that the critical current of a JJ depends on its geometry and can be difficult to measure in small Josephson junctions.

The second Josephson relation predicts a phase evolution if a voltage V is maintained across the junction

$$\frac{d\phi(t)}{dt} = \frac{2\pi}{\Phi_0} V(t). \tag{2.4}$$

If the phase of the superconducting state changes for example by 2π, a voltage pulse of a characteristic time τ and averaged height Φ_0/τ occurs. The characteristic time τ depends on the damping of the junction and is calculated in two distinct limits in section 2.1.4 (with $\tau \equiv T_{od}$) and 2.1.5 (with $\tau \equiv \tau_{RC}$).

These two Josephson equations can be used to calculate the total energy of the Josephson junction $E = E_{\text{J}} + E_{\text{C}}$.

The first term, E_{J}, is associated to the tunneling of Cooper pairs through the insulating barrier and describes the kinetic energy term

$$E_{\text{J}}^{\phi} = \int_0^t V(\tau) I_s(\tau) d\tau = \int_0^t \frac{\Phi_0}{2\pi} \dot{\phi}(\tau) \cdot I_c \sin\phi(\tau) d\tau = \underbrace{\frac{\Phi_0 I_c}{2\pi}}_{E_{\text{J}}} (1 - \cos\phi)\,, \tag{2.5}$$

given the assumption that $\phi(0) = 0$. The average value is given by E_{J} and sets the characteristic tunneling energy.

The second term E_{C} is associated to the energy stored in the capacitor (of capacitance C) formed by the two overlapping metal electrodes. This electrostatic energy arises from N Cooper pairs (each of charge $2e$) located on each superconducting electrode

$$E_{\text{C}}^{N} = \frac{1}{2} C V^2 = \frac{1}{2} C \left(\frac{2eN}{C} \right)^2 = 4N^2 \underbrace{\frac{e^2}{2C}}_{E_{\text{C}}}, \tag{2.6}$$

where E_{C} is the charging energy of a single electron.

The energy needed to add a Cooper pair is therefore

$$\Delta E_{\text{C}} \equiv E_{\text{C}}^{N+1} - E_{\text{C}}^{N} = 4(2N+1) E_{\text{C}}. \tag{2.7}$$

2.1.2 Josephson inductance

When a Josephson junction is biased by an external current it will carry the current as a supercurrent (i.e. no voltage drop) up to the maximal value I_c (as given by the first Josephson equation (2.1)) and will then switch to the resistive branch by producing quasi-particles (single electron excitations) which give rise to a voltage across the junction. In fact, the current in the resistive regime is carried by single electrons rather than Cooper pairs.

The first Josephson equation (2.1) even allows one to extract a kinetic inductance related to the kinetic energy of the Cooper pairs. This can be seen by taking the time derivative of the first Josephson junction equation (2.1)

$$\frac{dI_s}{dt} = I_c \cos(\phi) \frac{d\phi}{dt} = I_c \cos(\phi) \frac{2\pi}{\Phi_0} V(t), \tag{2.8}$$

where the last step makes use of the second Josephson equation (2.4). Comparing equation (2.8) with the general induction law $dI/dt = V/L$ shows the non-linear inductance of a JJ is

$$L_s = \underbrace{\frac{\Phi_0}{2\pi I_c}}_{L_c} \frac{1}{\cos\phi}. \tag{2.9}$$

In summary, the charging energy E_c is associated to a capacitance, the coupling energy E_J is associated to a non-linear inductance while the creation of quasi particles can be described by a resistor. This leads to the electric circuit model of a Josephson junction consisting of a current/voltage biasing source, a capacitance, a nonlinear inductance and a resistance.

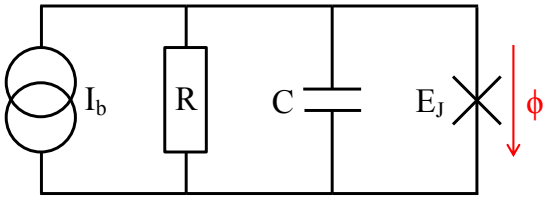

Figure 2.1: The RCSJ-model with the phase difference ϕ across the junction.

2.1.3 The RCSJ model

A simple electrical circuit model of a JJ is the so called RCSJ-model. It consists of the junction (described by the non-linear inductance) which is in parallel with a biasing current I_b, a capacitor and a resistor as shown in figure 2.1. The value of R will be close to the normal state resistance R_n at T_c of the JJ (associated to the quasi particle current $I_n = V/R$) whereas the capacitor simply corresponds to the parallel plates of the JJ which are separated by the insulating layer. In the finite voltage regime, a displacement current penetrates the capacitor, $I_d = C \cdot dV/dt$.

Within this so called RCSJ model one can use Kirchhoff's rules, such that the total current is equal to the biased one

$$I_b = I_s + I_d + I_n = I_c \sin\phi + C\frac{dV}{dt} + \frac{V}{R}. \tag{2.10}$$

This inhomogeneous second order differential equation can be rewritten by using the second Josephson equation (2.4)

$$0 = \left(\frac{\hbar}{2e}\right)^2 C\ddot{\phi} + \left(\frac{\hbar}{2e}\right)^2 \frac{1}{R}\dot{\phi} + \frac{\partial U(\phi)}{\partial\phi}, \tag{2.11}$$

$$U(\phi) = -E_J \cos\phi - \frac{\hbar}{2e} I_b \phi, \tag{2.12}$$

where $E_J = \frac{\Phi_0 I_c}{2\pi}$ is the Josephson coupling energy. The potential $U(\phi)$ is plotted for three different biasing currents in figure 2.2 and is called a *tilted washboard potential*. Notice the similarity to the standard equation of motion for a particle of mass m moving in one

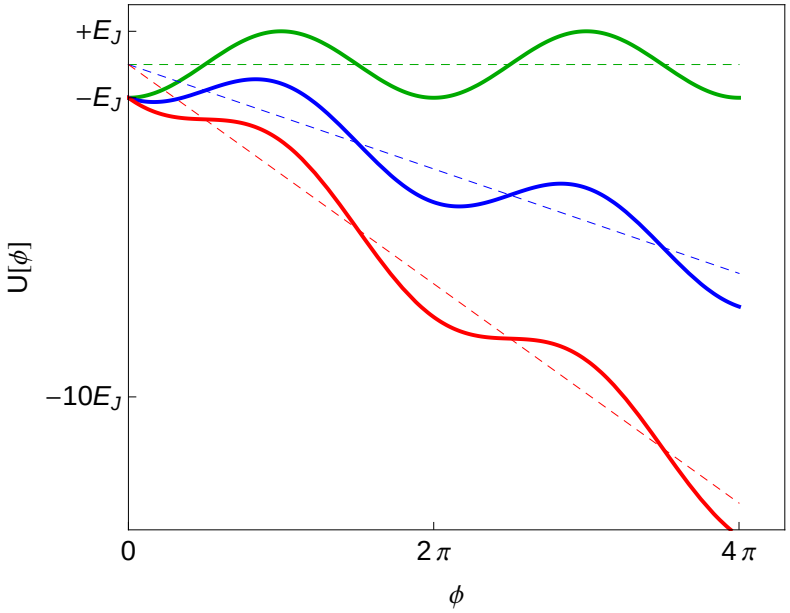

Figure 2.2: Washboard potential for different biasing currents. From top to bottom: $I_b/I_c = 0, 0.5, 1.05$. The dashed lines indicate the I_b-dependent part of the tilted washboard potential.

dimension and affected by a potential U and damping κ

$$0 = m\ddot{x} + \kappa\dot{x} + \nabla U. \tag{2.13}$$

The mass of the "phase particle" can be identified with the capacitance C, i.e. $m \rightarrow (\hbar/2e)^2 C$. The damping is inversely proportional to R, i.e. $\kappa \rightarrow (\hbar/2e)^2/R$, as the resistor is in parallel to the junction.

In order to further analyse the dynamics of the RCSJ model, it is necessary to calculate the potential differences ΔW_- and ΔW_+ as indicated in figure 2.3

$$\Delta W_- = 2E_\mathrm{J}\left(\sqrt{1-\left(\frac{I_b}{I_c}\right)^2} - \frac{I_b}{I_c}\arccos\frac{I_b}{I_c}\right) \approx 2E_\mathrm{J}\left(1-\frac{I_b}{I_c}\right)^{3/2}, \tag{2.14}$$

$$\Delta W_+ = 2\pi\hbar I_b/2e + \Delta W_-. \tag{2.15}$$

Furthermore, the differential equation (2.11) for $I_b = 0$ may be compared to a damped harmonic oscillator, allowing tor the definition of a quality factor Q and a plasma fre-

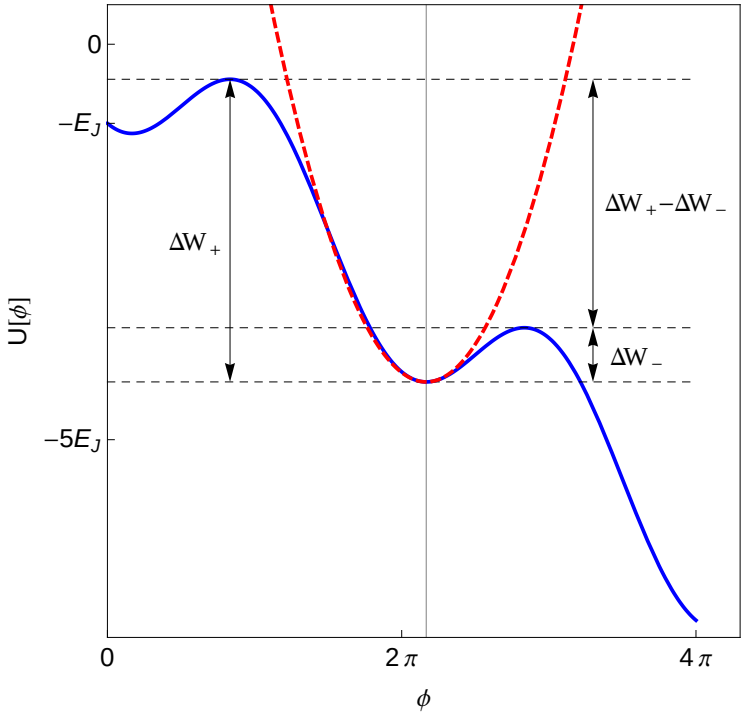

Figure 2.3: Washboard potential for $I_b = 0.5I_c$ and its relevant potential differences. The red, dashed curve shows the harmonic approximation near a minimum.

quency ω_p in the linear regime (i.e. $\sin(\phi) \approx \phi$) as

$$\omega_p = \sqrt{\frac{2eI_c}{\hbar C}}, \tag{2.16}$$

$$Q = \omega_p RC \equiv \sqrt{\beta_c}. \tag{2.17}$$

where β_c is the so called *Stewart-McCumber parameter* [1]. To understand the meaning of β_c it is useful to look at the RCSJ circuit as a RC element coupled to a RL element (with inductance $L \to L_c$) with each a resistance of $R \to R/2$. The ratio between the typical time constants is then the unitless Stewart-McCumber parameter

$$\beta_c = \frac{\tau_{\mathrm{RC}}}{\tau_{\mathrm{RL}}} = \frac{RC/2}{2L_c/R} = \frac{2\pi I_c R^2 C}{\Phi_0} = \pi^2 \left(\frac{R}{R_q}\right)^2 \frac{E_J}{2E_c}. \tag{2.18}$$

R_q is the so called resistance quantum with the value $R_q = h/4e^2 = 6453.2\,\Omega$. The Stewart-McCumber parameter helps to illustrate the meaning of the quality factor $Q =$

$\sqrt{\beta_c}$ of a Josephson junction. In the presence of a bias current $I_b \neq 0$ the oscillation frequency, in the harmonic potential approximation, becomes I_b-dependent

$$\omega_a \equiv \sqrt{\frac{1}{C}\left(\frac{2e}{\hbar}\right)^2 \frac{\partial U(\phi_{min})}{\partial \phi_{min}}} = \omega_p \left(1 - \left(\frac{I_b}{I_c}\right)^2\right)^{1/4}. \tag{2.19}$$

The quality factor can be used to distinguish between the overdamped ($Q, \beta_c \ll 1$) and the underdamped ($Q, \beta_c \gg 1$) limit of the junctions dynamics. In the following two subsections these two cases will be analysed in more detail.

2.1.4 Overdamped JJ at T=0

Although the main body of this thesis concerns underdamped Josephson junctions, it is insightful to first consider the overdamped junction. Independent of the damping, the voltage across the junction is zero as long as $I_b < I_c$, which implies a time independent phase given by the Josephson relation $\sin(\phi) = I_b/I_c$. If the biasing current is greater than the critical current, the phase becomes a function of time, even if the applied current is constant with time. Thermal fluctuations, which are treated in section 2.1.7, are neglected in this subsection (i.e. $T = 0$).

For a biasing current I_b greater than the critical current, the second derivative of the phase can be neglected (see equation (2.11)) compared to the damping term for a low quality factor ($Q \ll 1 \Leftrightarrow \tau_{\text{RC}} \ll \tau_{\text{LC}}$). The reason is that the displacement current I_d is negligibly small. The differential equation (2.11) for the phase reduces to

$$\dot{\phi} = \frac{2eI_cR}{\hbar}\left(\frac{I_b}{I_c} - \sin\phi\right) \equiv \frac{2e}{\hbar}V. \tag{2.20}$$

Note that the change of the phase is always positive if $I_b > I_c$, but varies periodically with $\sin\phi$, i.e. the supercurrent changes its direction relative to the applied dc current.

The solution of equation (2.20) is given by (up to an additive constant)

$$\phi(t) \;=\; 2\arctan\left(\frac{I_c}{I_b}+\sqrt{1-\left(\frac{I_c}{I_b}\right)^2}\tan\left(\frac{eR\sqrt{I_b^2-I_c^2}}{\hbar}\,t\right)\right). \qquad (2.21)$$

This shows that $\phi(t)$ has a time periodicity of $T_{od} \equiv \pi\hbar/(eR\sqrt{I_b^2 - I_c^2})$. Therefore, the voltage $V(t) = R(I_b - I_c \sin\phi(t))$ consists of pulses which are separated by the same time periodicity and occur with a frequency of $f_{od} \equiv 1/T_{od} = 2eR\sqrt{I_b^2 - I_c^2}/h$ as shown in figure 2.4. The time averaged voltage of a single pulse is

$$\bar{V} \equiv \langle V(t)\rangle \;=\; \frac{1}{T_{od}}\int_0^{T_{od}} V(t)dt \qquad (2.22)$$

$$\;=\; \frac{\Phi_0}{T_{od}} \qquad (2.23)$$

$$\;=\; R\sqrt{I_b^2 - I_c^2}. \qquad (2.24)$$

It is important to stress that $\bar{V}$ can also be calculated by using the second Josephson relation (2.4), where the phase difference is 2π and the time interval is just the period T_{od}:

$$\frac{2\pi}{T_{od}} = \frac{2e}{\hbar}\bar{V}. \qquad (2.25)$$

This shows that the phase slip by 2π is the elementary resistive process in a JJ [1] for $I_b > I_c$.

The IV curve ($\bar{V} = R\sqrt{I_b^2 - I_c^2}$) smoothly interpolates the zero voltage state for $I_b < I_c$ and Ohm's law $V = I_b R$ for $I_b \gg I_c$, see figure 2.5. By considering again the picture of the tilted washboard potential, the phase particle slowly slides down and each time it overcomes a "hill" its phase changes by 2π and causes a voltage pulse as shown in the top panel of figure 2.4. The time integral of the voltage over one period is proportional to $1/T_{od}$ and therefore becomes larger for higher bias currents I_b. Furthermore, an increase in the bias current also causes an increase of the time between the discontinuous phase

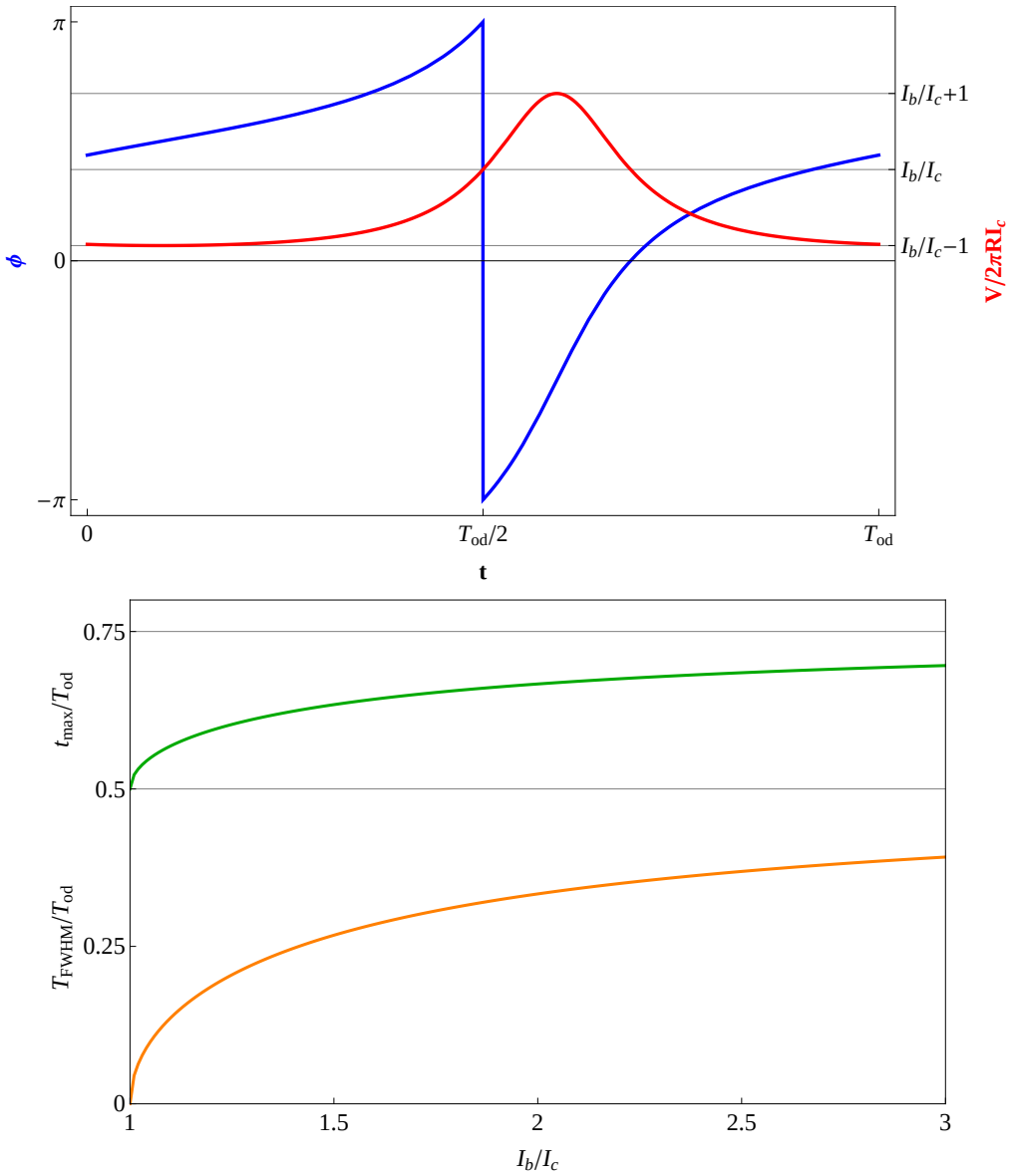

Figure 2.4: Top: Overdamped Josephson junction in the resistive regime ($I_b/I_c = 1.2$). Blue: Time-dependence of the phase during one period (T_{od}), indicating a phase-change of 2π. Red: Resulting voltage pulse as a function of time which is proportional to the time-derivative of the phase. Bottom: Full width at half maximum (T_{FWHM}) of the voltage pulse, normalised to one period of the phase (T_{od}), as a function of the relative bias current shown in orange. The green curve shows the time at which the voltage pulse reaches its maximum (t_{max}), relative to T_{od}, as a function of bias current.

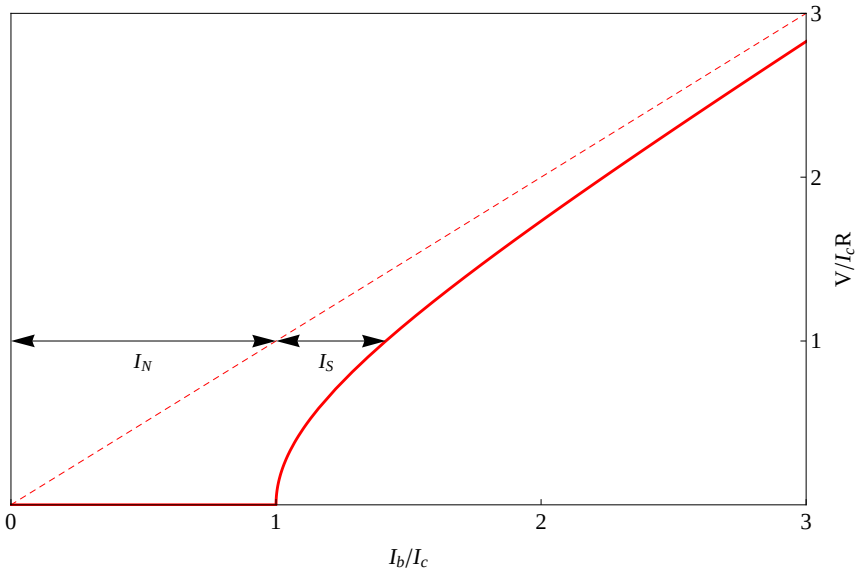

Figure 2.5: The plot shows the time-averaged voltage as a function of the applied current of an overdamped Josephson junction. Zero voltage regime for $I_b < I_c$ and square-root dependence in the resistive branch. The dashed line indicates the ohmic law which is the asymptotic solution for $I_b \gg I_c$. The current in the resistive branch consists of a normal- and supercurrent (I_N respectively I_S).

change and the maximum of the voltage pulse, as can be seen by green line in the bottom panel of figure 2.4. Another effect of the increase of I_b is a simultaneous increase of the width of the voltage pulse (defined by the full width at half maximum (FWHM)) relative to the time period (T_{od}), shown by the orange line in the bottom panel of figure 2.4. Ultimately ($I_b/I_c \to \infty$), the maximum of the voltage pulse is reached at $0.75T_{od}$ with a FWHM of $0.5T_{od}$. The maximum of the voltage peak is $V_{max} = 2\pi R(I_b + I_c)$ and the minimum is $V_{min} = 2\pi R(I_b - I_c)$.

2.1.5 Underdamped JJ at T=0

When the junctions capacitance C is large enough such that $Q \gg 1$ respectively $\tau_{\mathrm{RC}} \gg \tau_{\mathrm{LC}}$, the junction is in the underdamped limit. This is usually reached in small Josephson junctions and, in contrast to the overdamped case, the V(I)-curve shows hysteresis, as will be seen later.

The differential equation (2.11) can be simplified in the underdamped limit by neglecting

the oscillating supercurrent I_s and the solutions of the associated RC-circuit are easy to calculate:

$$I_b = \frac{C\hbar}{2e}\ddot{\phi} + \frac{\hbar}{2eR}\dot{\phi}, \tag{2.26}$$

$$\phi(t) = \frac{2eI_bR}{\hbar}\left(t + RCe^{-t/RC}\right), \tag{2.27}$$

$$V(t) = RI_b\left(1 - e^{-t/RC}\right). \tag{2.28}$$

The additional constant for the solution $\phi(t)$ was set to zero and the boundary condition $\dot{\phi}(0) = 0$ was used. The time averaged voltage is therefore given by Ohm's law

$$\bar{V} \equiv \langle V(t)\rangle = \lim_{\Delta t\to\infty}\frac{1}{\Delta t}\int_0^{\Delta t} V(t)dt = RI_b. \tag{2.29}$$

As already mentioned, the V(I)-characteristic of an underdamped JJ shows a hysteric behavior as shown in figure 2.6. Increasing I_b from zero, the phase particle is trapped in the local minimum until the bias current reaches the critical current. At $I_b = I_c$ the voltage jumps discontinuously up to the finite voltage $V = RI_c$, such that the phase particle is now in the so called "running state", i.e. the particle is now sliding down in the washboard potential. As the current is further increased, the voltage increases linearly, $V = RI_b$. If, from this state, I_b is now decreased to just below I_c it is found that the voltage will not drop to the zero state until I_b reaches the so called *retrapping current* $I_r \leq I_c$. The effect is caused by the small damping. In terms of the washboard analogy this means that the energy which is supplied by the bias current is not fast enough dissipated by the phase particle due to the small damping. The retrapping current is defined as the maximum current at which the dissipated energy of the particle from one maximum of the washboard to the next maximum is equal to the work done by the source [1], this is given by

$$I_r = \frac{4I_c}{\pi Q}. \tag{2.30}$$

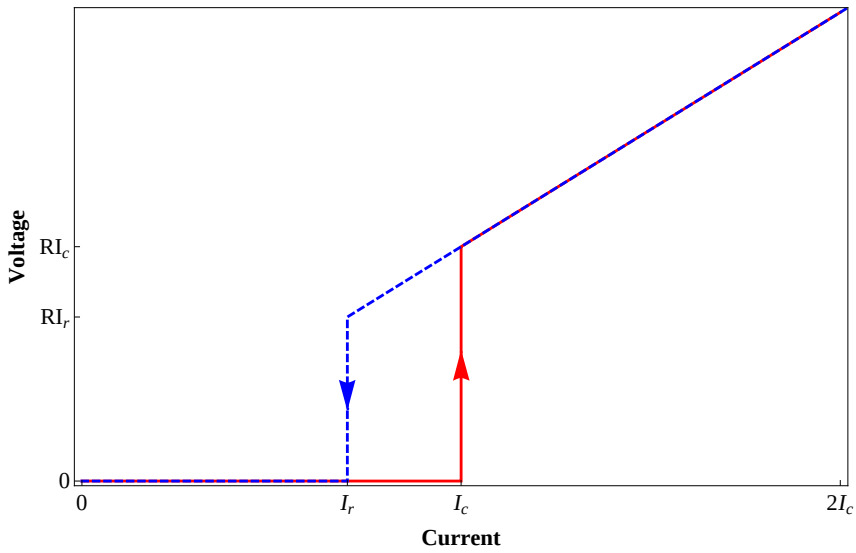

Figure 2.6: The plot shows the time-averaged voltage as a function of the applied current for an underdamped Josephson junction. The V(I)-characteristic will follow the red line during the increase of the bias current from 0 to $> I_c$ and follows the blue, dashed line when decreasing I_b again and will ultimately switch to the zero-voltage state if $I_b < I_r$.

In fact, this retrapping current only plays a role for the underdamped circuit since it is only smaller than I_c if $Q > \pi/4$. If there was no damping, i.e. $Q \to \infty$, the phase particle could not be stopped until $\Delta W_- = \Delta W_+$ which is only fulfilled for $I_b = 0$, see equations (2.14) and (2.15).

So far, the impedance of the bias current source was assumed to be infinite in the RCSJ-model, but this assumption only holds for DC-signals due to the usually large bias resistor (in our case R_b =1 MΩ). As the bias resistor is in parallel to the much smaller junction resistance R_n, its influence can be neglected for low frequencies. However, the characteristic frequency of the junction $\omega_J \equiv 2\pi\langle V(t)\rangle/\Phi_0$ (second Josephson equation (2.4)), is in the 10^{10} GHz range, such that the typical lead impedance is around 50-100 Ω [1]. The impedance seen by the junction at frequencies around ω_J is therefore much larger than R_n and has a major impact on the retrapping current [45]. For small Josephson junctions with a typical R_n in the kΩ range, the damping effect of the lead impedance has therefore to be taken into account [1].

Equation (2.30) shows the dependency of the retrapping current I_r on the quality factor

Q which itself depends on the resistance R as given in equation (2.17). By taking into account a temperature dependent resistance associated with the freezing out of the quasi-particle damping, given by $R \rightarrow R^* \equiv R_n \exp(-\Delta/k_B T)$, the quality factor Q would increase exponentially at lower temperatures [1]. The retrapping current would therefore decrease exponentially as the temperature is lowered until it reaches $I_r = 0$ at T=0.

Johnson et al. [45] measured the bottoming out of I_r at low temperatures to a constant value of

$$I_{r0} = \frac{I_c^2 Z_l}{2V_g \cdot (1 + (4C_j Z_l \Delta/\hbar)^2)}, \tag{2.31}$$

with the gap voltage $V_g \equiv 2\Delta/e$, the capacitance of the junction C_j and the impedance of the lead Z_l.

This is in contradiction to the above discussion which expects $I_r = 0$ at T=0. This abrupt stop of the decrease in I_r was explained by taking into account the damping effect of the lead at high frequencies ($\approx \omega_J$). The total impedance $Z(\omega_J)$ at high frequency consists of a parallel contribution of the junctions capacitance C, the quasi-particle resistance R^* and the impedance of the lead Z_l [1, 45]

$$1/Z(\omega_J) = i\omega_p C + 1/R^* + 1/Z_l \tag{2.32}$$

By equalising the input power supplied by the source to the dissipative terms at DC and at ω_J, Johnson et al. identified the retrapping current, under the assumption of small capacitance $\omega_J C Z_l < 1$, as

$$I_r^* \approx I_c \sqrt{2Re(Z)/R^*} \tag{2.33}$$

In the limit $R^* \rightarrow R_n$ and $Z \rightarrow \infty$, equation (2.33) reduces to $I_r^* \rightarrow \sqrt{2} I_c/Q$ which compares well to the already obtained retrapping current in equation (2.30). The more

interesting limit is reached at high frequencies when the lead impedance can not be neglected, i.e. $Z_l \ll R^*$, and equation (2.33) reduces to $I_r^* \approx I_c\sqrt{2Z_l/R^*}$. In this limit, I_r^* falls as $1/\sqrt{R^*}$ compared to $I_r \propto 1/R_n$ given by equation (2.30). As soon as the corresponding voltage $V_r \propto R^* I_r^*$ reaches the gap voltage $V_g = 2\Delta/e$, the retrapping current becomes temperature independent with a constant value of I_{r0} as given by equation (2.31). This was indeed experimentally observed by Johnson et al. and is unique to small Josephson junctions. Section 2.1.6 discusses a theoretical description of a small Josephson junction embedded in an arbitrary environment characterised by the impedance $Z(\omega)$.

2.1.6 The P(E) theory

A more general description of a small, voltage-biased Josephson junction coupled an arbitrary environment of impedance $Z(\omega)$ is given by the so-called *P(E)-theory* [46–49]. The environment itself is modeled by an infinite series of LC-oscillators which is also-called the *Caldeira-Leggett*-model [50, 51]. The function P(E) represents the probability that a Cooper pair which tunnels through a small, voltage-biased (V_b) Josephson junction transfers the energy $E = 2eV_b$ to the environment (described by the impedance $Z(\omega)$). The total supercurrent corresponds to the sum of the forward Γ_{LR} and backward Γ_{RL} tunneling rates which can be expressed as [46–49, 51]

$$I_s = 2e(\Gamma_{LR}(V_b) - \Gamma_{RL}(V_b)) = \frac{\pi e E_J^2}{\hbar}(P(2eV_b) - P(-2eV_b)) \qquad (2.34)$$

The probability $P(E)$ depends on the arbitrary environment $Z(\omega)$ and the temperature T as given by [51]

$$P(E) = \frac{1}{2\pi\hbar}\int_{-\infty}^{+\infty} \exp\left(J(t) + \frac{i}{\hbar}Et\right)dt \qquad (2.35)$$

$$J(t) = 2\int_{-\infty}^{+\infty} \frac{Re(Z_t(\omega))}{\omega R_q}\frac{e^{-i\omega t} - 1}{1 - e^{\hbar\omega/k_BT}}d\omega, \qquad (2.36)$$

whereas $Z_t(\omega) = 1/(i\omega C + 1/Z(\omega))$ is the total impedance seen by the Josephson junction, similar to equation (2.32).

The P(E)-theory has a restricted validity which depends on the bias voltage V_b and the electromagnetic environment given by the impedance $Z(\omega)$. In the high impedance limit ($Z(\omega) \gg R_q$), equation 2.34 is valid as long as $E_J \ll E_c\sqrt{R_q/Z(\omega)}$. In the low impedance limit ($Z(\omega) \ll R_q$), equation 2.34 can only be applied as long as $E_J \ll 1/P(2eV_b)$ which depends on the voltage bias [47].

To simplify the discussion further, one assumes a pure resistive environment, i.e.$Z(\omega) = R$. As long as $R \ll R_q$, the I(V)-curve of the junction shows a suppercurrent peak at $V_b = 0$ for $T = 0$. For finite temperatures, the I(V)-curve looks the same as the I(V)-curve of an overdamped Josephson junction [49, 52] which will be discussed in more detail in section 2.1.7. However, the I(V)-curve can be seen in figure 2.8 which is a plot of equation 2.42 for different temperatures.

In the limit of a high resistive environment ($R \gg R_q$), the peak in I(V)-curve is shifted to $V_b = E_c/2e$ in comparison to the low resistive limit. This indicates a Coloumb blockade at biasing voltages below $V_b = e/C$ as the charging energy of the junction E_c is now comparable to the energy supplied by the voltage source ($2eV_b$). Figure 2.7 shows the I(V)-curve for a purely resistive environment $Z(\omega) = R > R_q$ at $T = 0$ for different ratios of R/R_q. The P(E)-function becomes Gaussian such that the peak in the I(V)-curve is sharpening with an increase of the R/R_q ratio. This Coloumb blockade was first shown experimentally by Kuzmin et al. [53]. In another experiment, Watanabe et al. studied the I(V) characteristic of a small Josephson junction embedded in a tunable electromagnetic environment realised by SQUID arrays [54]. By increasing the impedance of the environment, it was possible to induce a Coulomb blockade in the single Josephson junction.

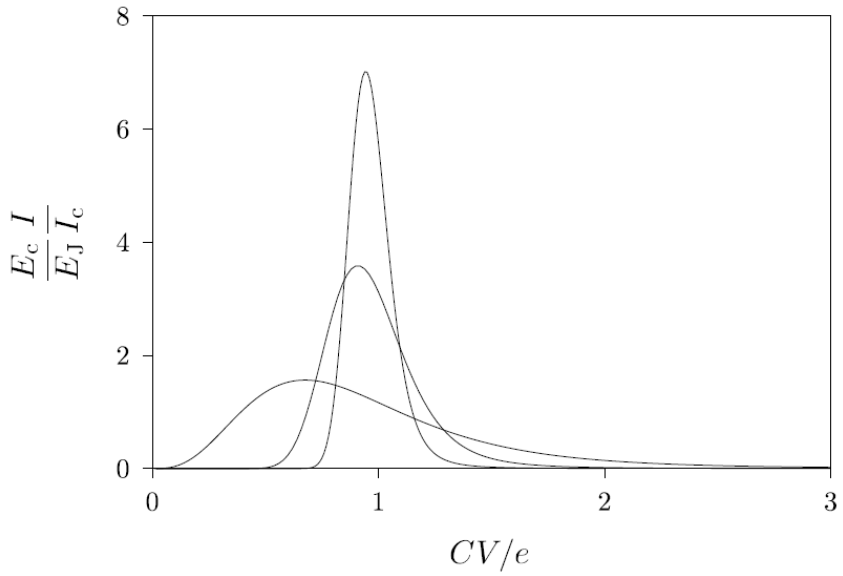

Figure 2.7: The I(V)-curve of a voltage biased Josephson junction in the Coulomb blockade regime at $T = 0$. The environment is purely ohmic ($Z(\omega) = R$) and satisfies $R/R_q > 1$. The peak is sharpening with increasing $R/R_q = 2, 20, 100$. The figure is taken from [49]

2.1.7 Thermal effects

The thermal energy for temperatures $T \neq 0$ is $k_B T$ and can affect the IV characteristic significantly. In the case of a zero biasing current, the energy required for the phase particle to exceed the cosine potential to reach the next potential minimum is given by $\Delta W_-(0) = 2E_J$. The ratio between these two energy scales is $2E_J/k_B T$ and provides a measure of the influence of any thermal effects. In the limit $T \ll T_c$ (where the energy gap is nearly constant, $\Delta(0) = 1.764 \cdot k_B T_c$) it can be approximated as [1]

$$\frac{2E_J}{k_B T} = 1.764 \, \frac{R_q T_c}{R_n T}. \tag{2.37}$$

If the normal state resistance is now larger than the quantum resistance, i.e. $R_n > R_q$, thermal fluctuations affect the behavior of the junction down to temperatures $T/T_c \approx R_q/R_n$ whereas in the opposite case, i.e. $R_n < R_q$, fluctuations only play a role near T_c where $\Delta(T) \ll \Delta(0)$.

The additional thermal energy affects the tilted washboard model in the sense that the

phase particle is now more likely to overcome the potential well to reach the next, 2π phase shifted, potential minimum. The probability for a thermally activated phase slip by 2π is $\propto \exp\left(-\Delta W_{-}/k_{\mathrm{B}}T\right)$, with ΔW_{-} given by equation (2.14). This probability now has to be multiplied by the number of attempts per time (equation (2.19)) and gives a rough idea for the likelihood of a thermally activated phase slip. A more detailed calculation of the thermal escape rate, including the quality factor Q, is given by [1, 55, 56]

$$\Gamma_{th} = a_t \frac{\omega_a}{2\pi} e^{-\Delta W_{-}(I_b)/k_{\mathrm{B}}T}, \tag{2.38}$$

$$a_t = 4/(\sqrt{1+Qk_BT/1.8\Delta W_{-}}+1)^2, \tag{2.39}$$

$$\omega_a = \omega_p \cdot \left(1-(I_b/I_c)^2\right)^{1/4}. \tag{2.40}$$

By neglecting the Q-dependent pre-factor a_t, equation (2.38) describes an exponential rising from a very low probability $\propto \frac{\omega_a}{2\pi} e^{-2E_{\mathrm{J}}/k_{\mathrm{B}}T}$ for small biasing currents to a maximum value $\propto \omega_a/2\pi$ near I_c and decreasing close to I_c, due to the lower attempt frequency.
The effective critical current therefore decreases due to thermal activations in the underdamped case.

Thermal noise can also be modeled as an additional current I_{jn} in equation (2.10) (respectively an additional current source in figure 2.1) that accounts for the Johnson-Nyquist noise. Its root mean square value is

$$I_{jn} = \sqrt{\frac{4k_{\mathrm{B}}T\Delta f}{R}}, \tag{2.41}$$

where Δf is the bandwidth over which the noise is measured, given in Hertz, and R is the resistance given by the RCSJ-model. This modeling is mostly used to simulate the effect of thermal noise in a JJ. This method was previously used to calculate the effect of thermal fluctuations in an overdamped JJ giving the following analytical expression for

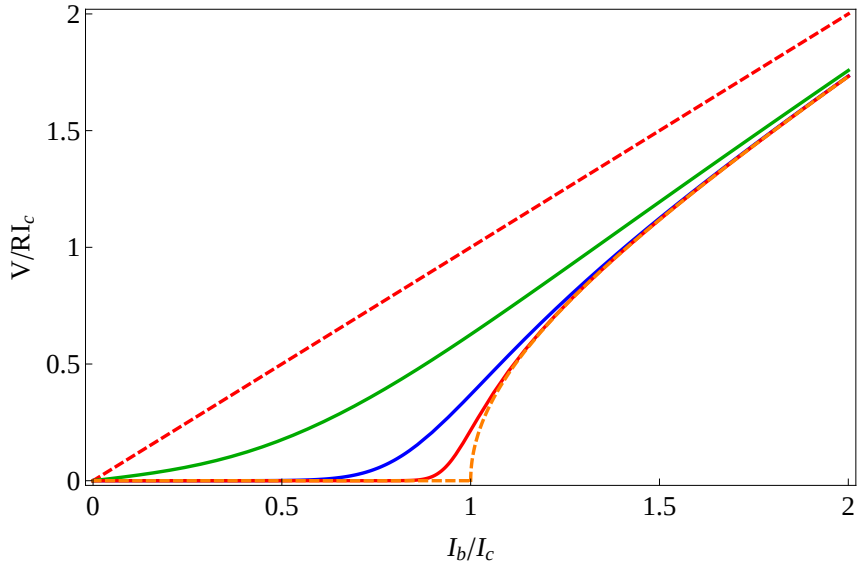

Figure 2.8: Time-averaged voltage as a function of the applied current in the overdamped case with Johnson-Nyquist noise. From top to bottom: Normal state resistance (red, dashed), $\alpha \equiv \hbar I_c/(2ek_bT) = 2$ (green), $\alpha = 10$ (blue), $\alpha = 50$ (red), $\alpha = \infty$ (orange, dashed).

the current-voltage characteristic [52, 57–60]

$$V = RI_b - \Im\left(\left(\frac{I_{1-i\hbar I_b/(2ek_bT)}\left(\hbar I_c/(2ek_bT)\right)}{I_{-i\hbar I_b/(2ek_bT)}\left(\hbar I_c/(2ek_bT)\right)}\right)\right) RI_c, \tag{2.42}$$

where $I_n(z)$ is the modified Bessel function of the first kind and $\Im(...)$ takes the imaginary part of the expression. This function is plotted for several cases in figure 2.8. The fluctuation free case (orange, dashed line) has a sharp edge at $I_b = I_c$. This edge gets rounded when thermal fluctuations are taken into account and the Josephson junction switches into the resistive state at lower bias currents. The asymptotical solution for very large bias currents is shown as a red, dashed line and just represents Ohm's law. A more general treatment of thermal fluctuations with this method leads to the so called phase *Langevin equation* [51]

$$\ddot{\phi} + Q^{-1}\dot{\phi} + \sin\phi = I/I_c + \delta I(t)/I_c. \tag{2.43}$$

$\delta I(t) = I(t) - \langle I(t) \rangle$ describes the fluctuations around the time averaged current and satisfies

$$\langle \delta I(t) \rangle = 0, \tag{2.44}$$

$$\langle \delta I(t) \delta I(0) \rangle = \int_{-\infty}^{\infty} S_I(\omega) e^{i\omega t} dt, \tag{2.45}$$

$$S_I(\omega) \equiv 2\hbar\omega \Im\left(Y(\omega)\right) \left(\coth\left(\frac{\hbar\omega}{2k_b T} \right) + 1 \right). \tag{2.46}$$

Equation (2.45) is the fluctuation-dissipation theorem that uses the impedance $Y(\omega)$ (equation (2.46)) of the sample, that is assumed to be in thermal equilibrium at a temperature T. The *noise power spectral density* $S_I(\omega)$ can be calculated in two limits

$$S_I\left(|\omega| \ll k_b T/\hbar\right) = 4\Re\left(Y(\omega)\right) k_b T, \tag{2.47}$$

$$S_I\left(\omega \gg k_b T/\hbar\right) = 4\Re\left(Y(\omega)\right) \hbar\omega. \tag{2.48}$$

$\Re(...)$ takes the real part of the expression. Equation (2.47) describes the current fluctuations of a resistance at low frequencies due to thermal noise. Whereas equation (2.48) describes quantum fluctuations that are present even at $T = 0$. Note that $S\left(-\omega \gg k_b T/\hbar\right) = 0$, because quantum fluctuations can only absorb energy in contrast to the thermal fluctuations [7].

Quantum fluctuations therefore become relevant at low temperatures, i.e. $k_{\text{B}} T \ll E_{\text{J}}$. These fluctuations are not temperature dependent as the phase particle tunnels through a potential well rather than thermally hopping over it [61, 62]. The so called *cross-over temperature* separates the thermally activated escape regime from the quantum regime, as will be explained in section 2.2 in more details.

2.2 Switching current distribution

Biasing a Josephson junction with a current $I_b \ll I_{c0}$ (I_{c0} is the fluctuation-free critical current) in absence of any fluctuations leaves the phase particle localised in one of the potential wells and the junction therefore remains in the zero-voltage state. This situation changes if one takes fluctuations into account. Fluctuations are especially relevant for underdamped Josephson junctions because once the phase particle escapes the initial potential well it will accelerate down the washboard potential until it reaches a finite velocity (depending on the damping) and will never retrap again [1]. The junction can therefore switch into the voltage state even for the case $I_b \ll I_{c0}$ and develop a voltage of the order of the gap $V_g = 2\Delta/e$ between the electrodes [1]. The voltage $V_g = 2\Delta/e$ is larger than expected by the RCSJ model for an underdamped JJ with $\bar{V}(I_c) = RI_c$, as given by equation (2.29). As the minimum energy needed to break a single Cooper pair is 2Δ, the corresponding voltage is $V_g = 2\Delta/e$. The binding energy of a Cooper pair is not taken into account in the RCSJ model which explains the discrepancy of the expected voltage at I_c.

The fluctuation-induced switching (either thermal or quantum) of the junction from the zero-voltage to the running state is a stochastic process due to the randomness of the fluctuations itself. By assuming the independence of escape events one can model the probability of the escape, $P(I_b)$, within the time- and current interval dt, dI_b by [63]

$$P(I_b) = \Gamma\left(I_b\right)\left(\frac{dI_b}{dt}\right)^{-1}\left(1 - \int_0^{I_b} P\left(\tilde{I}\right) d\tilde{I}\right). \tag{2.49}$$

$\Gamma\left(I_b\right)$ is the escape rate of the phase particle from the potential well and dI_b/dt is the ramp rate of the bias current. Experimentally the switching probability $P(I_b)$ is either measured by a constant ramp rate of the biasing current or by applying a bias current pulse of duration dt and amplitude dI_b to then extract the escape rate $\Gamma(I_b)$. The pulsed measurements of the switching probability are described in chapter 6.

Depending on the type of fluctuations one can extract the noise-free critical current I_{c0}, the junction's capacitance C_j, the effective junction resistance R_n and the temperature by comparing the measured $P(I_b)$ with the theoretical model for the given fluctuation regime. It is important to stress that fluctuations in the escape process are not necessarily an undesirable effect in this situation, as it provides a way to get a deeper insight into the characteristic parameters of the Josephson junction. The crossover temperature T_{co} which separates the thermal- and quantum fluctuations is given by

$$T_{co} = \frac{\hbar\omega_p}{2\pi k_B} \cdot \left(\sqrt{1 + (2Q)^{-2}} - (2Q)^{-1} \right), \tag{2.50}$$

where the large quality factor of an underdamped junction ($Q \gg 1$), simplifies equation (2.50) to $T_{co} \approx \hbar\omega_p / 2\pi k_B$.

For high temperatures $k_B T \gg \hbar\omega_p$, T_{co}, thermal fluctuations dominate the escape process, described by the classical thermal escape rate Γ_{th} in equation (2.38). Using the approximate function of the barrier height given in equation (2.14) and inserting it into Γ_{th} leads to the following equation

$$\left(\ln\left(\frac{a_t \omega_a}{2\pi \Gamma_t} \right) \right)^{2/3} = \left(\frac{2E_J}{k_B T} \right)^{2/3} \cdot (1 - I_b / I_{c0}) \,. \tag{2.51}$$

Equation (2.51) allows to easy compare theory with the experimental data, since the right hand side is linear in terms of the measured bias current I_b.

At $T < T_{co}$, thermal fluctuations are exponentially suppressed and the phase particle can only get into the running state below the critical current by quantum tunneling through the potential barrier. The temperature independent quantum tunneling rate Γ_q is given

by [56, 64]

$$\Gamma_q = a_q \cdot \frac{\omega_a}{2\pi} \cdot \exp\left(-\frac{7.2 \cdot \Delta W_-}{\hbar\omega_a} \cdot (1 + 0.87/Q)\right), \tag{2.52}$$

$$a_q = \sqrt{120\pi \frac{7.2 \cdot \Delta W_-}{\hbar\omega_a} \cdot (1 + 0.87/Q)}. \tag{2.53}$$

Notice that the escape rates for thermal activation (TA) Γ_{th} and for the quantum tunneling (MQT) Γ_q look very similar, it therefore makes sense to introduce a general escape rate Γ with an escape temperature T_{esc} equal to $T_{esc,t}$ and $T_{esc,q}$ for the thermal activation regime and the quantum tunneling regime respectively [62]:

$$\Gamma = (\omega_a/2\pi) \exp\left(-\frac{\Delta W_-}{k_B T_{esc}}\right), \tag{2.54}$$

$$T_{esc,t} = \frac{T}{(1 - k_B T \ln(a_t)/\Delta W_-)}, \tag{2.55}$$

$$T_{esc,q} = \frac{\hbar\omega_a}{(7.2 k_B (1 + 0.87/Q)(1 - p_q)))}, \tag{2.56}$$

$$p_q = \frac{\hbar\omega_a \ln(a_q)}{((1 + 0.87/Q)7.2 \cdot \Delta W_-)}, \tag{2.57}$$

$$\left(\ln\left(\frac{\omega_a}{2\pi\Gamma}\right)\right)^{2/3} = \left(\frac{2E_J}{k_B T_{esc}}\right)^{2/3} \cdot \frac{1}{I_{c0}} (I_{c0} - I_b). \tag{2.58}$$

Equation (2.58) will be useful later when switching current data analysis is discussed. Due to the low critical current (nA range) in small Josephson junctions it is critical to be able to apply and read-out small currents respectively voltages. This makes the measurement of small Josephson junction more challenging compared to larger junctions with critical currents in the 10^2 µA range [56].

2.3 Cumulative escape probability

The cumulative escape probability $\widetilde{P}$ is given by

$$\widetilde{P} \equiv \int_0^{I_b} P(i) \cdot di \quad = \quad 1 - \exp\left(-\Gamma(I_b) \cdot \Delta t\right) \tag{2.59}$$

$$\Longrightarrow \quad \Gamma(I_b) = -\ln\left(1 - \widetilde{P}\right)/\Delta t \tag{2.60}$$

with $P(i)$ being the switching probability distribution and $\Gamma(I_b)$ the escape rate from the superconducting to the normal state of the junction.

In order to get a deeper understanding of this cumulative switching process one has to calculate the bias current necessary to reach a certain cumulative probability $\widetilde{P}$. By inserting the general form of the escape rate from equation (2.54) into equation (2.59) one gets

$$(\omega_a/2\pi)\exp\left(-\frac{\Delta W_-}{k_B T_{esc}}\right) \quad = \quad -\ln\left(1-\widetilde{P}\right)/\Delta t, \tag{2.61}$$

$$\Delta W_-/k_B T_{esc} \quad = \quad \ln\left(-\frac{\omega_a \cdot \Delta t}{2\pi \ln\left(1-\widetilde{P}\right)}\right). \tag{2.62}$$

Equation (2.62) can be further simplified using the usual approximation for the potential well ($\Delta W_- \approx 2E_J\left(1 - I_b/I_{c0}\right)^{3/2}$), yielding:

$$\frac{I_b}{I_{c0}} \quad \approx \quad 1 - \left(\frac{k_B T_{esc}}{2E_J} \cdot \ln\left(-\frac{\omega_a \cdot \Delta t}{2\pi \ln\left(1-\widetilde{P}\right)}\right)\right)^{2/3}. \tag{2.63}$$

Neglecting the current dependence of the attempt frequency ω_a, by setting $\omega_a = \omega_p$, further simplifies equation (2.63). This is justified by the fact that ω_a, given by equation (2.19), is only significant different from the plasma frequency near I_{c0}. This simplified model shows the important dependence of the switching current as a function of the temperature, namely $I_b(\widetilde{P}) \propto T_{esc}^{2/3}$.

There are two different figures of merit that characterise the cumulative switching pro-

cess, the bias current for $\widetilde{P} = 0.5$ which decreases with temperature as $T_{esc}^{2/3}$ and the width $\Delta I_b = I_b(0.9) - I_b(0.1)$ increases as $T_{esc}^{2/3}$.

2.4 Experimental background

Experimentally, small Josephson junctions presently remain relatively unexplored in comparison to large area junctions. This is probably because they are difficult to fabricate and difficult to measure. Accordingly, a clear picture based on a systematic study of the temperature dependent escape phenomena is not yet available [65]. However the motivations for developing the physics and technology of this regime of small junctions have increased recently. The properties of small junctions are interesting because a new regime of Josephson junction operation may be explored and they offer the study of new phenomena which are not known from large junctions [1, 66]. A small junction implies a small junction capacitance, a small Josephson energy and a narrow but, to some extent, selectable range of R_n that places the junctions in a strongly underdamped, highly fluctuating and strongly hysteretic regime. Technologically, solving the problems of physical understanding and precise and reliable measurement in this regime are important because of the wide interest in developing such devices. They may be used, for example as highly sensitive current threshold detectors to read-out solid-state qubits [67,68]. They also have potential for use as nanoscale thermometers, single photon detectors, phase qubits and other devices. Experiments on small Josephson junctions are difficult to perform in part because the low critical current (on the order of 10^1 nA) is highly sensitive to unwanted and poorly controlled current noise. The behaviour of small junctions is also likely to be very sensitive to temperature and incident electromagnetic radiation down to the single photon regime. In addition, the high normal state resistance R_n (in the order of $10^1\,\mathrm{k}\Omega$) can make it necessary to include the environmental impedance $Z(\omega)$ at the Josephson frequency $\omega_J = 2eV/\hbar$ which will greatly increase damping at this frequency [1] and

complicates the physics (see section 2.1.5 for more details). Most experiments to date on small Josephson junctions, have been performed on junctions with relatively high I_c in the range several hundred nA or μA, compared to the 100 nA or so expected for our junctions. The first studies of hysteretic Josephson junctions were performed by Martinis and Kautz [58, 69] who uncovered the phenomenon of phase diffusion, a process in which the phase particle is in an intermediate regime between free movement and trapped in a well, instead it moves from well to well in a diffusive process such that the junction displays a voltage that is neither zero nor the full gap value but in-between. For small Josephson junctions in the overdamped case, Vion et al. [66] could show the existence of a phase diffusion regime at finite temperatures which causes a small voltage drop over the junction before it switches to the running state. This process was shown not to be dominated by the usual thermal activation as is the case for large area junctions. However, Kivioja et al. [65] could show theoretically and experimentally, that a regime exists where escape does not lead to a finite voltage state but rather to underdamped phase diffusion. As this result is relevant for the Josephson junction regime considered in this thesis, a more detailed discussion follows.

Kivioja et al. [65] measured the cumulative escape probabilities (see section 2.3 for further information) of two different samples, one was a dc-SQUID with a R_n =1.3 kΩ, and the other was a single Josephson junction with R_n =0.41 kΩ. The results of the dc-SQUID measurement are more relevant to our samples and we therefore focus the discussion on them. The loop inductance of the dc-SQUID was around 4 times larger than the Josephson inductance (see equation (2.9)) such that the device almost behaves as a single Josephson junction with a tunable critical current and a maximum value of I_{c0} =200 nA. The capacitance of the sample were estimated to be C_J =100 fF and the sample showed a strong hysteretic I(V) characteristic with retrapping currents well below 1 nA. A surface mounted resistor with R_s =500 Ω and capacitor with C_s =5 nF were used to keep the Josephson junction in the underdamped regime even at ω_J. Here lies the main difference to the ex-

perimental work performed by Vion et al. [66] as their junction was overdamped at this high frequency. The measured cumulative escape probabilities of Kivioja et al. on the dc-SQUID were consistent with the macroscopic quantum tunneling model (see section 2.2) at low temperatures, i.e. below the crossover temperature T_{co} =50 mK. Above T_{co}, the cumulative escape probabilities agree with the thermally activated model, specifically $I_b(\widetilde{P} = 0.5)$ and the width $\Delta I_b = I_b(0.9) - I_b(0.1)$ both follow the predicated temperature dependence. In a newly discovered feature, at a temperature T_D ≈335 mK, the width ΔI_b decreases abruptly whereas $I_b(\widetilde{P} = 0.5)$ saturates at $\approx 0.3 I_{c0}$. This phenomena was explained by a model based on that described in section 2.1.5. It considers the effect of frequency dependent damping on the retrapping current and lead to an underdamped phase diffusion, occurring at a bias current $I_m = 4I_{c0}/\pi Q(\omega_J)$. The quality factor $Q(\omega_J)$ is calculated by using equation (2.17) with $R \rightarrow R_s$ =500 Ω and $C \rightarrow C_J$ =100 fF and gives $Q(\omega_J)$ ≈4. Their measured saturated $I_b(\widetilde{P} = 0.5)$ ≈0.3I_{c0} is therefore in agreement with the calculated I_m =0.32I_{c0}. In the underdamped phase diffusion regime, the phase particle diffuses from one metastable well to another and causes a voltage drop which is smaller than $V_g = 2\Delta/e$, and this process is independent of the temperature. By applying a magnetic flux to the dc-SQUID loop, the critical current could be decreased to around 60 nA and showed no trace of thermal activation at any temperature. The interpretation of this behaviour was that the junction switches directly from the macroscopic tunneling regime for $T < T_{co}$ to the underdamped phase diffusion regime for $T > T_{co}$ as T_D is expected to be less than 30 mK. A useful diagram of their results can be seen in figure 2.9. Later, Yoon et al. [70] were able to avoid the underdamped phase diffusion regime and maintain thermal activation in small underdamped Josephson junctions by decreasing the crossover temperature T_{co}. This was achieved by fabricating a large shunt capacitance in parallel to the Josephson junction. By also measuring a similar device without the additional shunt capacitance they could show that the shunt capacitance preserved the thermal escape process at all temperatures measured.

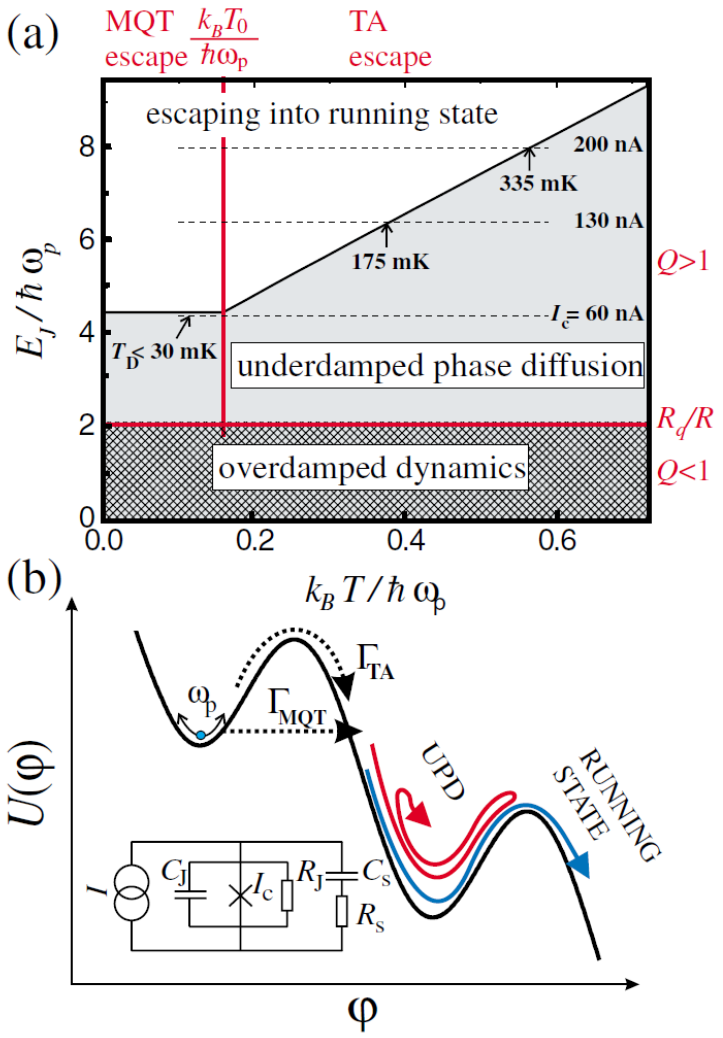

Figure 2.9: a) The different regimes of a small dc-SQUID with low critical current. The different critical currents (indicated by dashed lines at 60 nA, 130 nA and 200 nA) were achieved by applying a magnetic flux into the loop of the dc-SQUID to reduce I_{c0}. The corresponding temperatures T_D indicate the temperatures above which the dc-SQUID switches into the underdamped phase diffusion regime. The vertical red line separates the macroscopic tunneling (MQT) regime from the thermally activated escape (TA) which takes place at the crossover temperature $T_0 \equiv T_{co}$. b) The dynamics in the upper well and schematic behaviour upon escape. Inset: equivalent circuit of the junction with frequency dependent dissipation. Taken from [65].

In summary, few experiments have been done in the regime of small Josephson junctions, but for careful measurements in junctions with critical currents down to approximately $500\,\mathrm{nA}$ the now standard theoretical framework described earlier in this chapter appears to work well. In the experiments described in this thesis we now try to push this down towards $100\,\mathrm{nA}$.

Chapter 3

Sample fabrication

A 3 inch Si/SiO_2 wafer is the starting point of the fabrication process. The first step is the fabrication of the gold leads using a photolithographic process (figure 3.1) and thermal thin film evaporation. After dicing the wafer into samples of size $9 \times 9\,\mathrm{mm}^2$, the main structure is fabricated by using a modified scanning electron microscope (SEM) and two-angle shadow evaporation of aluminium [71] with an oxidation stage in between. Several etching processes are applied during the fabrication to clean the samples between different stages. My main task was to develop a recipe for the fabrication of reproducible and stable small Josephson junctions with a typical normal state resistance of $R_n \approx$ 1-3 kΩ. The overlap area has to be in the range of $0.05\,\mu\mathrm{m}^2$ to reach such values of R_n. This chapter describes the extensive and time consuming work that was designed to raise the reliability of the fabrication of small $Al/AlO_x/Al$ Josephson junctions. Room-temperature methods for sample characterisation are discussed to access the reliability and reproducibility of the fabrication.

3.1 Wafer preparation

The starting wafer from *Si-Mat* has a surface resistivity of $10 - 20\,\Omega\,\mathrm{cm}$ and is thermally oxidised to get a layer of SiO_2 $(250 - 300\,\mathrm{nm})$ on both sides [72]. The cleaning of the

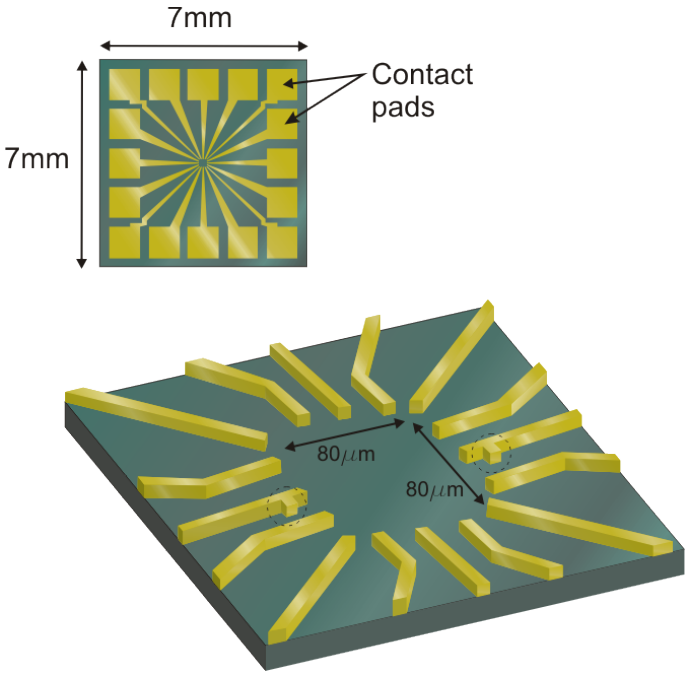

Figure 3.1: The schematics of the photolithographic fabricated gold leads on top of the substrate. The leads connect the contact pads to the small structure which is later fabricated inside the (80×80) µm^2 area by electron beam lithography. The dashed circles in the bottom figure show the alignment markers which are needed for the second, small structure fabrication step.

wafer is a crucial step in the fabrication of small Josephson junctions to remove impurities from the substrate [73].

The first cleaning step is a reactive ion etch (RIE) which removes any organic residues by inserting the wafer in an oxygen plasma for 2 minutes (*Plasmalab 80 Plus, Oxford Instruments)*. The second step is simply rinsing the wafer in warm acetone in an ultrasonic bath before dipping it into isopropanol to rinse off the acetone. After the last step, the wafer is blow-dried using a Nitrogen gun.

3.2 Photolithographic process

Directly after the cleaning procedure, the wafer is baked on a hot plate at $120\,^{\circ}\mathrm{C}$ for several minutes to remove any water which might have accumulated on the surface from the surrounding air. This also makes it easier to spin the resist smoothly onto the wafer

[74]. The first (i.e. bottom) layer of positive resist, *Microchem LOR 5B*, is then spun onto the wafer to give an expected thickness of 500 nm based on the spin curves [74]. After baking at $150\,^{\circ}\mathrm{C}$ for 5 minutes to harden the resist, the second (i.e. top) positive resist, *Microchem S1813* , is spun on top with a thickness of around 1200 nm [75] and then hard baked on a hot plate ($90\,^{\circ}\mathrm{C}$ for 5 min). See the schematics in figure 3.2. As a next step, the two layers of resists are UV-exposed through a chromium patterned glass mask with a mercury lamp (90 lux) for 150 seconds. *Microposit MF-319* is used to develop the pattern for a time of 80 seconds. This time can be tuned if the undercut in the bottom resist is not large enough. In order to get rid of any residual resist, a reactive ion etch is performed by inserting the wafer into an oxygen plasma (4 min, 100 W, 100 standard cubic centimeters per minute (SCCM), 100 mTorr). The wafer is now ready for metallic coating for which a thermal evaporator is used (more details can be found in section 3.2.1). Firstly, a 5 nm adhesion layer of *NiCr* is evaporated onto the wafer, making it possible to then evaporate Au with a thickness of around 80 nm. Metal films of the group 1B (copper, silver and gold) require additional bonding layers of adhesion to insulators (i.e. silicon dioxide) as their oxide layers are not adequate for adhesion itself [76, 77]. These two evaporations are done consecutively without breaking the vacuum. Liftoff of unwanted metals is done with *Microposit 1165* remover, the wafer is subsequently flushed with deionised water. A RIE oxygen-plasma etch is used to clean the wafer from residual resists after the lift-off process.

3.2.1 Thermal evaporation

A thermal evaporator from *Edwards* was used to deposit the desired materials under vacuum and it is equipped with a digital thickness monitor. This system has two sources which allows two different materials to be evaporated, for example $NiCr$ and Au in this case. The sample holder of the evaporator is designed to hold two chips with the maximum dimensions of $(10 \times 10 \times 1)\,\mathrm{mm}^3$ each. The holder can be manually rotated along a

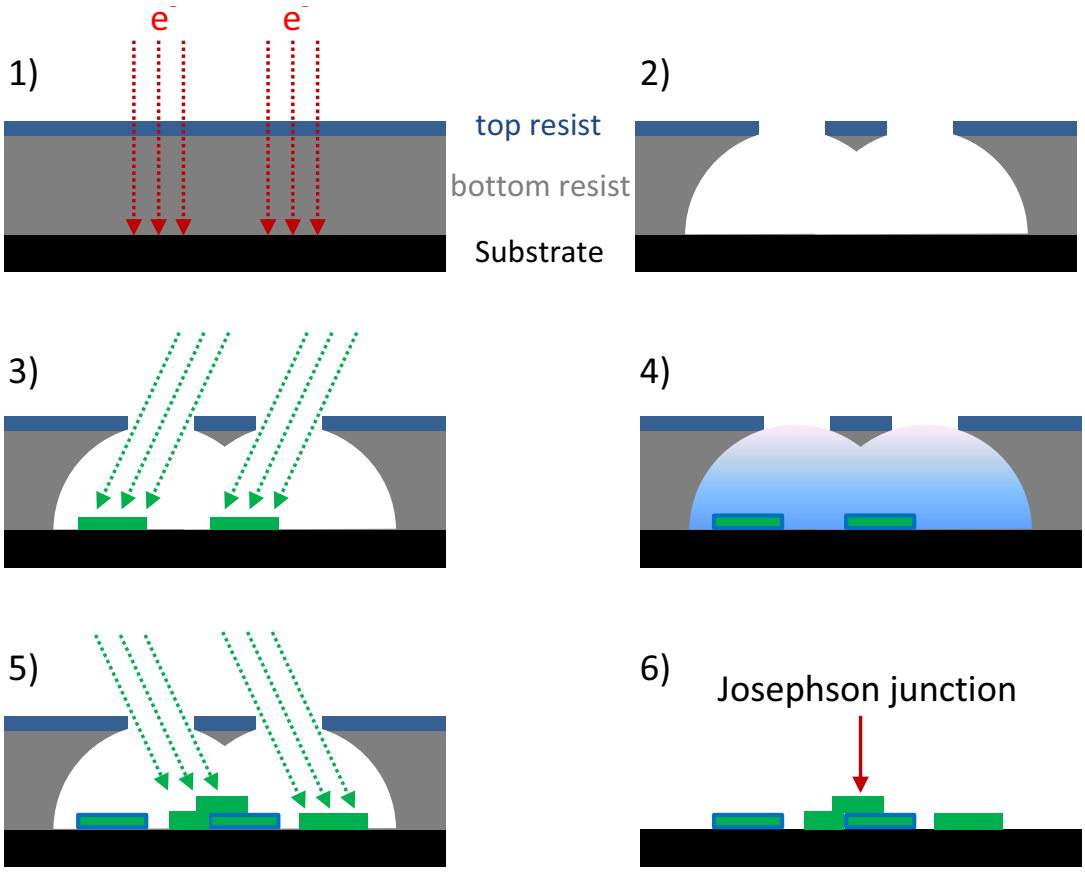

Figure 3.2: Schematics of the fabrication process of a Josephson junction by the Dolan bridge technique. 1) Electron beam exposure 2) Development with creation of an undercut 3) First aluminium evaporation 4) Oxidation stage 5) Second aluminium evaporation which creates overlap between two aluminium layers 6) Lift off which leaves the Josephson junction in the center.

fixed axis by 360 degrees as this will later be needed to perform a double-angle evaporation. There is an additional sample holder for a whole wafer (maximum size is 3 inches), but it is only possible to evaporate perpendicular to its surface. It also has a gas inlet for Ar, O_2 or a gas mixture of both which can be set for a fixed ratio and are controlled by a digital flow meters. The evaporator is also equipped with an argon ion plasma to mill oxide layers or to clean the substrate (not available for a whole wafer sample holder).

After developing the resists and cleaning the wafer with a RIE process, it can be mounted onto the evaporator's sample holder. The two different thermal boat sources made of tungsten are filled with a short Nichrome wire and with a gold pellet respectively. The sources have to be separated by a metallic wall to avoid mutual contaminations during the evaporation. The Nichrome is used to form an adhesion layer between SiO_2 (i.e. the substrate) and Au and is therefore very thin, usually 5 nm. It is important to check that the thickness monitor is working properly before closing the chamber. The chamber has to be pumped down with a rotary pump for around 5 minutes to reach a pressure of less than 50 mTorr before opening the chamber to an oil diffusion pump (which has a liquid nitrogen trap). Around 2 hours later, the pressure should have reached approximately $(2-4)\times 10^{-6}$ Torr which is sufficient to start the evaporation.

The thermal source which contains the Nichrome wire is slowly heated up with the wafer protected by a shutter. The resonance frequency of a quartz crystal oscillator slowly changes due to the additional mass it gains during the evaporation and can therefore be tracked to measure the thickness and rate of the deposition. Two parameters have to be set for each deposited material: the speed of sound and the mass density. A third, tooling parameter is set by the calibration of the monitor and depends on the geometry of the crystal resonator. As soon as a stable rate of around 0.2 nm/s is reached, the shutter can be opened and the evaporated Nichrome will be deposited onto the wafer before closing the shutter again and cooling down the thermal source. A thickness of 5 nm of Nichrome is sufficient. The pressure inside the chamber usually rises by around an order of magnitude

during this time due to offgassing. The second evaporation of Au is done in the same way and rate but with a thickness of around 80 nm. The chamber is kept under vacuum for 5-10 minutes after the last evaporation so that everything is cooled down before the chamber is vented with air.

3.2.2 Liftoff

When the deposition is finished, the positive resist is stripped off from the wafer and all deposited material on top of it will also be lifted-off, leaving only the deposited material (i.e. the patterned structure) in direct contact with the wafer. To do so, the wafer is soaked in *Microposit 1165* for approximately 15 min at room-temperature. This removes the bulk of the resists. The wafer is then inserted into a vessel of clean remover for another 60-90 min. The use of a small diameter pipette helps to mechanically blow-off any persistent resist. The wafer is then rinsed in deionised water and blow-dried with nitrogen gas.
As a last step an additional oxygen plasma cleaning is performed for 4 min to guarantee a clean surface.

3.3 Electron beam process

The steps previously described will fabricate the on-chip Au measurement leads ready for the attachment of the much smaller Josephson junctions that are fabricated in a separated process using an electron beam lithography. This section will describe the steps necessary to fabricate small Josephson junctions. A schematic overview can be seen in figure 3.2. In order to reach high resolution for patterning small structures (< 500 nm), an electron beam lithographic (EBL) system is used with a maximum acceleration voltage of 30 kV. Here, a modified *JEOL 6460* with an electrostatic beam blanker (200 V) and the *Nanomaker* software fulfills the requirement. It has three different apertures with diameters $20\,\mu$m, $30\,\mu$m, $100\,\mu$m.

3.3.1 Resist coating and dicing

There are two possible routes to follow after the 3 inch wafer is equipped with the gold leads:

1. Coating the wafer with a protective resist before cutting it into the desired chip size and then coating each chip individually with the two different electron dose sensitive resists.

2. Coating the wafer with the two different electron dose sensitive resists and then dicing it.

The first procedure protects the wafer during the cutting process but it can not be guaranteed that the thickness of the two electron sensitive resists are always the same. In addition it takes significantly more time to coat the small chips individually. The second procedure achieves a fixed resist thickness for all (9×9) mm^2 chips and controls one of the unknowns in the fabrication process but it does not allow to change the thickness of the two resists for different chips without stripping it off first. The second procedure was chosen without using any additional protective layer before dicing the wafer because it would likely cause additional mechanical stress to the very thin (80 nm) top layer resist.

3.3.2 Chip preparation

The procedure is very similar to the photolithographic steps, described in section 3.2, and it should be performed immediately after the oxygen plasma cleaning of the wafer. One starts by putting the wafer on a hot plate at $120\,^{\circ}\mathrm{C}$ for several minutes and then spinning the first layer of positive resist (13-14 % *Nanocopolymer in Ethyl lactate*, around $1\,\mu$m thick) over the entire wafer before baking it on a hot plate for 5 minutes at $110\,^{\circ}\mathrm{C}$. A second positive resist (*ZEP 520A* 1:1 or 1:3 Anisole, 80-350 nm) is spun and the wafer is baked (5 minutes at $110\,^{\circ}\mathrm{C}$). The first layer of resist is more sensitive to the electron

irradiation (direct, secondary and also backscattered electrons) which is needed to create an undercut for the later two-angle shadow evaporation and lift-off. The choice of the two resists is advantageous because it allows to develop the layers separately, which is in contrast with the more widely used PMMA/MAA and PMMA resist technologies [78] that are usually developed simultaneously with an MIBK-IPA mixture, where one relies on the different etch rates.

The wafer can now be cut into small chips of the size 9×9 mm^2 by scratching it with a diamond tip and breaking it on a sharp edge along the crystallographic direction. The chips must then be immediately inserted into isopropanol and any accumulated dust blown off from the surface using a pipette. An optical microscope inspection (preferably with a dark field) helps to guarantee a good cleaning and already damaged chips can be discarded.

3.3.3 Electron beam lithography

The structure which has to be written by the electron beam must first be designed and drawn. To do so, one can either use the *NanoMaker-Editor* software which directly creates a *.GDB file or one can use the more convenient software *AutoCAD* program and export it in a *.DXF format (R12/LT2 DXF) that can then be imported into *NanoMaker*. A dose factor has to be assigned to every geometrical object, with 100% set to correspond to a dose of $150\,\mu$C/cm^2 [79]. The optimal dose factors were determined by a dose testing structure, consisting of different sized horizontal- and vertical lines and additionally circles with different diameters. Notice that this is a crucially important step, especially for structures smaller than 300 nm that need a very large dose. A marker file *.MRK also needs to be created in order to later align the drawing to the prepared chip that has two little markers on the fabricated Au leads for this purpose (indicated by the dashed circles in figure 3.1).

Before loading the chip into the EBL system (a maximum of 4 chips of size 9×9 mm^2 can be loaded at the same time) it has to be cleaned with isopropanol, using a pipette to blow

off any dust and inspecting it with an optical microscope. The last step before inserting it into the EBL is to make a little scratch ($\approx$ 0.5 mm long) at the corner of the chip to later facilitate focusing the electron beam and to perform the stigmation. The chip can then be mounted tightly on the sample holder and inserted into the EBL system. After pumping the chamber down to around 0.1 mbar and setting the working distance to 10 mm, the focusing and stigmatism can be iteratively optimised using the scratch or a dirt particle. The aperture is set to $20\,\mu$m for a small sized write field ($100 \times 100\ \mu m^2$). Next, the beam current has to be measured. This is done by moving the beam to a Faraday cup and setting to 20 pA. The already fabricated markers on the gold leads (indicated by the dashed circles in figure 3.1) are used as reference points for the alignment of the designed structure to the chip. A parameter file has to be loaded into the software and it is used by the software to calculate the dwell time, exposure step size and line/point dose. The file contains the information about the type of substrate, the beam current and voltage, the sensitivity and type of resists used, including their thickness. Those parameters are also used to calculate the proximity correction by the software. The final step is to execute the exposure which in our case usually takes a couple of minutes. The order of patterning of the geometrical structures can be chosen beforehand.

3.3.4 Development

After the electron beam exposure, the bilayer positive resists are developed by two different chemicals. The first step is to develop the top resist layer by inserting the chip into *p-Xylene* for 15 seconds and continuously keeping the liquid in motion. The development is stopped by immersing the chip into isopropanol and rinsing it. The optimal development time can be checked by optical microscopy. The second step develops the bottom resist layer and also produces the undercut needed for the two-angle shadow evaporation and later lift off. The chip therefore goes directly from the isopropanol into a mixture of isopropanol and deionised water (with a volume ratio of 80 to 20). Here, the water is the

developer for the bottom resist and not the isopropanol. The immerse time is between 45 seconds and up to 2 minutes depending on the size of the undercut, which can again be checked using an optical microscope with a dark field after rinsing the chip in pure isopropanol and blow-drying it with the nitrogen gun.

3.3.5 Shadow evaporation and oxidation

The technique of shadow evaporation was first described by G. J. Dolan in 1977 [80, 81] and is still the standard technique to fabricate small Josephson junctions and various other structures.

The *Edwards* thermal evaporator, previously described in section 3.2.1, is used. As already mentioned, the sample holder is designed for two samples with the maximum dimensions of $(10 \times 10 \times 1)$ mm^3 each and can manually be rotated along a fixed axis by 360 degrees. To mount the chip a very small amount of vacuum grease is used to stick the chip onto the holder preventing any sliding. Additionally a metallic cover is fixed over the chip to hold it in place. At this point, it is critical to check that a full rotation can be done with the mounted chip. A thermal boat made of tungsten is used to evaporate the 5N (i.e. 99.999%) aluminium. The source is made by taking around 10 cm of aluminium wire with a 1 mm diameter and then cleaning it with isopropanol before winding it around a clean pair of tweezers to make it fit to the boat. Additionally a metallic plate with a small slit is fixed above the boat to collimate the evaporated material. After aligning the source and the collimator, a glass cylinder is placed over the source and the chip to prevent the glass bell, which later covers the chamber, from also being coated. Moving the shutter in front of the chip and checking the correct operation of the rate monitor are the last things to do before pumping the chamber down for 2-2.5 hours. Because an argon ion milling and an oxidation will be needed later, it is advisable to pump out the gas pipes by leaving them open to the chamber during the evacuation.

After a pressure of around $(2 - 4) \times 10^{-6}$ Torr is reached an argon ion milling is carried

out with a constant gas flow of 1.5 standard cubic centimeters per minute (sccm) reaching a constant chamber pressure of around 1×10^{-4} Torr. The chip is then rotated in the plasma for around 10 seconds between $\pm 45^{\circ}$ to also clean the undercut area. This milling procedure cleans the developed surface from any residual resists and has been shown to reduce ageing of the tunnel barrier [73] (i.e. it prevents the normal state tunnel resistance to go up in time). It is necessary to wait for around 20 minutes after the cleaning has finished to reach the base pressure again. After heating up the source carefully until a stable rate of (0.2-0.3) nm/s is reached, around 25 nm of aluminium is then evaporated at an angle of $+21^{\circ}$ relative to the perpendicular axis of the chip surface. Oxidation is then carried out after the thermal source has cooled down for 5 minutes. Closing the pumping line, pure oxygen is injected at 10 sccm until a pressure of 950 mTorr is reached (this takes around 1.5 minutes) inside the chamber and left for 5 minutes before starting the evacuation. The second layer of aluminium is deposited in the same way as the first layer, but at an angle of -21° and a thickness of 40 nm. The reason why the second layer is thicker than the first one is related to stability, meaning that the edge between the double layer of deposited aluminium to the single layer is kept to a minimum to avoid mechanical stress. When the second layer of aluminium is deposited, the chamber is vented with pure oxygen (10 sccm) for 5 minutes to build a uniform and clean aluminium oxide layer before exposing it to air.

3.3.6 Lift-off

Warm ($50\,^{\circ}\mathrm{C}$) acetone is used to dissolve the resists that are directly stuck to the substrate. It is necessary to keep the acetone in motion when the chip is immersed to speed up the lift off. After around 10 minutes a small diameter pipette is used to carefully blow off the unwanted aluminium. If this technique does not work properly it is possible to use the ultrasonic bath by inserting the acetone vessel into it for a short time (approximately 2 seconds) at the lowest possible power. Unfortunately, there is also a high chance that this

invasive method will destroy the junction. Before drying the chip with the nitrogen gun, the chip is dipped into isopropanol. An optical microscope can be used to check that the lift off is complete.

3.4 Room-temperature characterisation

As part of the equipment in the cleanroom, a four-point measurement DC probe station with a *Keithley 2602* source meter can perform measurement of current-voltage characteristics. To do so, two needle-probes are placed on the golden bonding pads of the chip using an optical microscope (each pad has the dimensions (1.75×1.75) mm^2. A voltage is ramped by a simple *LabView* program between $\pm 100\,\mu$V and the corresponding current measured. The maximum applied voltage was chosen to be much smaller than gap voltage of aluminium $V_g \approx 400\,\mu$V. A linear fit extracts the normal state resistance R_n. For a typical $R_n \approx 3$ kΩ the theoretical value of the critical current of aluminium at T=0 K is predicted by the Ambegaokar-Baratoff formula [43, 44] $I_c^0 = 1.764\pi k_B T_c/2eR_n \approx 100$ nA.

Unfortunately, such small Josephson junctions (overlap area is around $0.05\,\mu$m^2) are very sensitive to voltage discharges and voltage spikes. I found that the setup described above in fact can destroy the junctions, meaning that a typical $R_n \approx 3$ kΩ typically reduces by around an order of magnitude (i.e. a short circuit is created as the lead resistance is around 10% of R_n).

By repeated measurements of a large set of 135 junctions it was shown that around $35\,\%$ of the working junctions broke each time they were measured with the probe station. Note that this occurred despite the fact that the two probe needles were short circuited on a single bonding pad before starting the measurement to equalise any possible potential difference across probe needles. Several methods were tried to avoid destroying the junctions in this way:

- Common grounding of the probe station, computer, source meter and operator
- Switching off all lights and only using a battery powered hand torch
- Using a potentiometer in parallel to the resistance measurement to avoid voltage discharge between the probe needles
- Twisting the cables between probe station and source meter to avoid any voltage pick ups.

None of these methods improved the damage rate of the junctions. A better solution was achieved by moving away from the probe station and using a simple handheld Multimeter (*Fluke 179 True RMS Multimeter*) instead with an adjustable resistance range in parallel with a potentiometer. The potentiometer short circuits the two source leads before contact is made with the sample and is ramped by hand to $1\,\mathrm{M}\Omega$ for performing the measurement and then short circuited again before disconnecting the leads from the sample. This relatively "low-tech" method was found to be reliable and repeatable. Although it was determined that the probe station is causing the damage of the samples by electrical spikes, it was never possible to eradicate them from this machine or to stop the probe station from damaging the samples.

3.4.1 Normal state resistance dependency

The normal state resistance R_n should depend inversely on the overlap area of the Josephson junction assuming all other parameters are equal [1]. By slightly under developing the resists during the fabrication process (see section 3.3.3) it was possible to create different overlapping areas even on a single chip. A total set of 70 Josephson junctions were fabricated and then measured with a handhold Multimeter in parallel to a potentiometer (as described in section 3.4) to extract R_n. In a second step, SEM pictures were taken at a magnification of $75000\times$ and the overlap area calculated by using *ImageJ* which allows

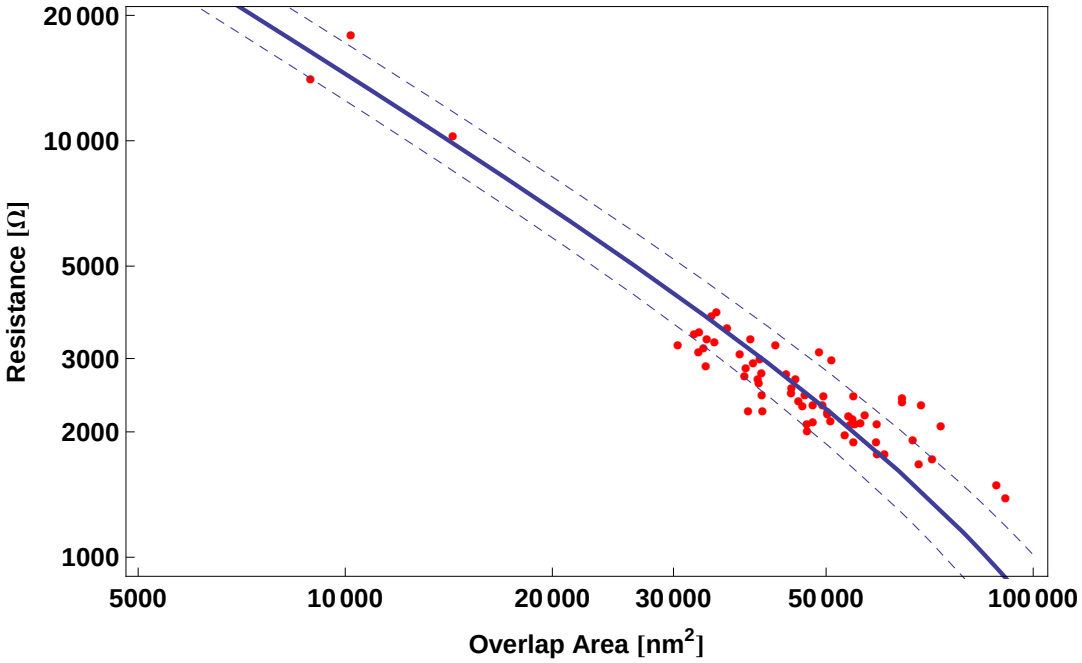

Figure 3.3: Normal state resistance as a function of the overlap area A of the junction. The solid blue line represents a fit to the $1/A$ model with the blue dashed lines indicating a standard error of $\pm 15\,\%$ in determing A.

the user to manually define the overlap area. The results can be seen in figure 3.3. The solid blue line is a fit to the inverse overlap area model. The least square method gives a fitting parameter of $153\,\Omega\mu m^2$ which is in good agreement with the literature (see for example [73,82]). The two dashed lines take into account a standard error of $\pm 15\,\%$. This relative error arises due to the difficulty to manually determine the overlap area. This important result shows that the difference observed in R_n on a single chip can be primarily explained by the difference in the overlap areas.

3.5 Reliability and Reproducibility

The reliability of R_n was checked by simultaneously fabricating two chips with 14 Josephson junctions each, as shown in figure 3.4. All junctions (red rectangles) had two leads with one connected to a common ground. A straight line was also included in the design (purple) to estimate the pure lead resistance. For junctions with an overlap area of around

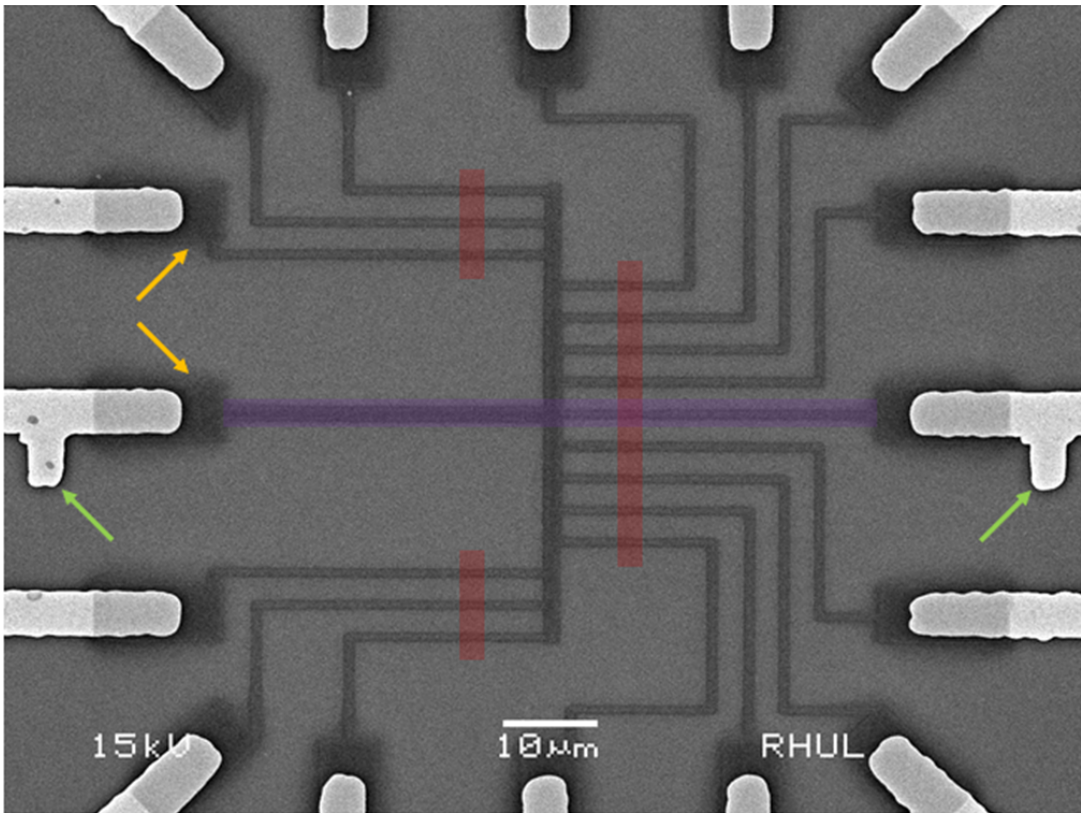

Figure 3.4: SEM image of a fabricated sample to check the reproducibility. The bright areas are the gold leads which are connected to the aluminium structure by rectangular pads (yellow arrows). The red marked areas indicate the position of the 14 Josephson junctions sharing a common ground (yellow, downwards facing arrow). The straight line (purple) is used to measure the lead resistance. Note the Au markers (green arrows) which are used to align the drawing for the e-beam patterning.

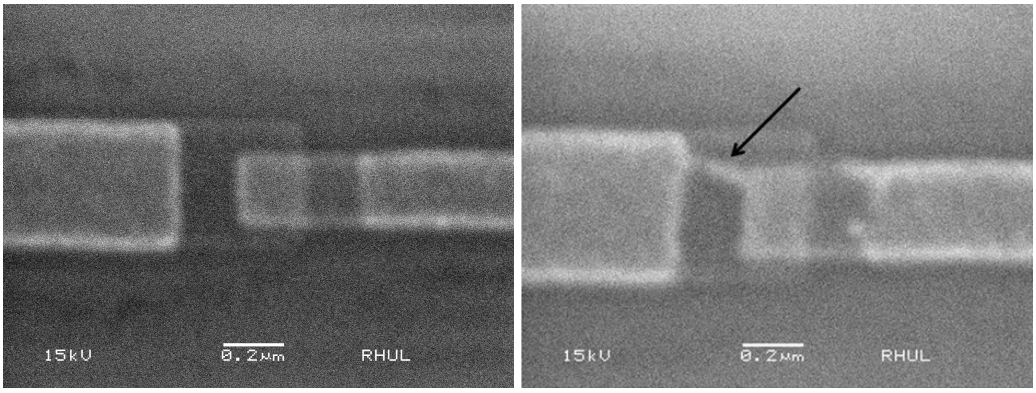

Figure 3.5: Left: SEM image of a working Josephson junction with an overlap area of around (200×200) nm^2. Although the resist has been stripped off the border of the undercut can still be seen and is around 200 nm wide. Right: Short circuited junction where the two edges seem to be connected (black arrow).

$0.05\,\mu\text{m}^2$ and a lead resistance of approximately $250\,\Omega$, an average value of $R_n = 3.5\,\text{k}\Omega$ (including the lead resistance) was found with a standard deviation of $0.5\,\text{k}\Omega$. This shows a good reliability in the fabrication of small Josephson junctions [73]. The main problem was that $10 - 20\,\%$ of the fabricated junctions exhibit a very small resistance (approximately equal to the lead resistance) indicating that they were short circuited at the oxide layer. Figure 3.5 shows the SEM image of a working junction (left) and one that is shorted (right). Judging by the SEM image the edges of the two deposited aluminium layers are directly connected (black arrow). Significant time has been spent trying to solve this problem, but without success so far. In order to try and isolate the cause of this problem it is in general advisable to simplify the problem and it is crucial to only change one parameter at the time. That means in this case to first look at the resist mask. To do so, the EBL was performed and Au then evaporated perpendicular to the chip surface (Au gives a better contrast when imaging it with the SEM due to the higher atomic number in comparison to aluminium) with a thickness of approximately 10 nm. The resist was not stripped off such that the mask can be analysed by the SEM, see figure 3.6. As one can see from the right image in figure 3.6, there is already a wide connection between the leads and there is additionally a small, curved line on the right lead. This suggests two possibilities: a)

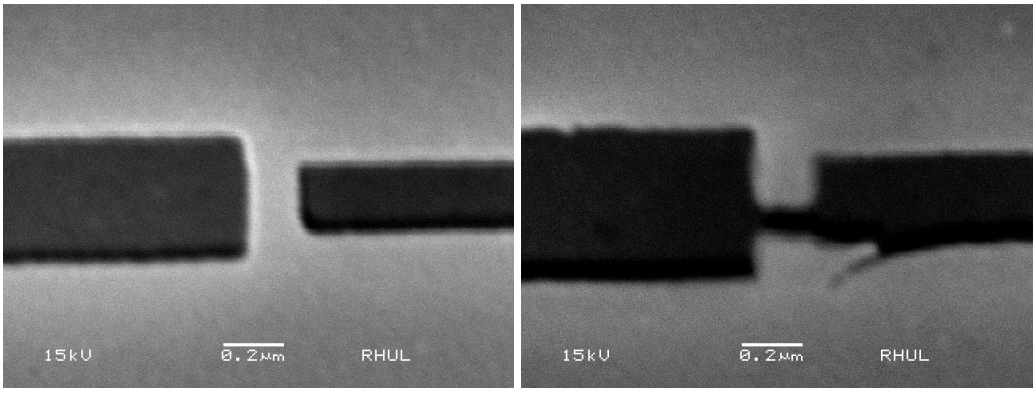

Figure 3.6: A thin (10 nm) Au layer was deposited after the development of the resists in order to check for defects in the mask. Left: SEM image of a desired resist mask for a Josephson junction. The black structure represents the desired opening of the resist layers. Right: Defects in the mask given by the opening of the mask between the two electrodes.

there is mechanical stress in the resist, and/or b) there is an electron beam control problem during the the exposure of the structure.

3.5.1 Mechanical stress in the resist layers

Mechanical stress at the boundary of two resist layers mostly builds up during the hard baking stage or during the patterning of the structure following the development when parts of the resists are removed. The list below shows various measures that have been tested to reduce mechanical stress.

a) Looking for a pattern in the location on the chip where most of the junctions are short circuited.

b) Reducing the number of junctions on a chip and keeping them further away from each other.

c) Changing the width of the bridge between the two leads by up to a factor of 2.

d) Skipping the argon ion milling cleaning to check for damage to the resist mask. Note that this step can not be skipped for the fabrication of Josephson junctions as the Al would otherwise not build a contact to the Au leads.

e) Heating the sample right before and/or right after the electron beam exposure. Several temperatures have been tried on different samples, ranging from $110\,^{\circ}\mathrm{C}$ to $140\,^{\circ}\mathrm{C}$ for a time of 2 minutes. This treatment softens the resists slightly and therefore reduces possible mechanical stress.

f) Vary thickness of the top resist between 60-350 nm.

g) Under develop the bottom resist to decrease the size of the undercut.

h) Try putting an additional thin layer of Germanium between the two resists. The structure was exposed into the top resist layer and then dry etched into the germanium by using a mix of $O_2 + SF_6$ gas before developing the bottom layer resist to get the desired undercut to continue with the evaporation. This additional layer of Germanium caused even more mechanical stress since it deformed (buckling) the flat surface of the resists. More time could be invested into this technique but it causes a significant increase in the time to fabricate a sample due to the additional steps.

For each measure, a set of 126 junctions were simultaneously fabricated and analysed by taking SEM pictures. None of these methods above was able to solve the short circuiting of some junctions. However, when the chip was not coated with the usual bottom resist and therefore only having one layer of resist on it (namely *ZEP520A*), the mask always looked perfectly fine. This is an indicator that the bottom layer resist might cause the mechanical stress between the two resists but surprisingly method e) did not show any effect to reduce the stress in this case.

3.5.2 Electron beam control and discharging

Another possible cause of the short circuit problem could be an error in the electron beam control, for example the beam does not switch off between the exposure of spatially

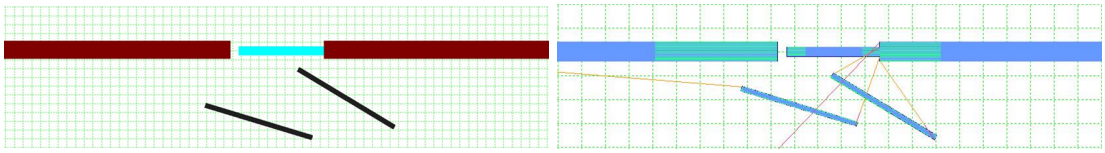

Figure 3.7: Left: Drawing of a single junction pattern. To force the beam not to cross the area of the bridge (i.e. area between dark red and turquoise shapes) two additional low dose rectangles have been added (black shapes). Dimension of green mesh is $200 \times 200\,nm^2$. Right: Beam simulation of the modified pattern in which no direct crossing happens in contrast to a simulation without the additional low-dose structure. Dimension of green mesh is $500 \times 500\,nm^2$.

separated geometrical shapes. Alternatively, there could be a discharging between the two leads during the patterning. Many attempts were made to prove that the short-circuiting of the junctions happens during the electron beam exposure, the following is a summary.

i) Increasing the dwell time, τ_d, which is the exposure time for a certain area A_{exp} and is related to the dose D by the beam current I_b through $D = I_b \cdot \tau_d / A_{exp}$. The speed of the beam $v_b = \sqrt{A_{exp}}/\tau_b$ during the patterning is therefore reduced which might reduce the risk of overshooting. This has been done by reducing the beam current I_b from 20 pA to 15 pA.

ii) By adding additional, sufficiently low dose (i.e. later development will not dissolve resist in these areas) structures close to the bridge between the leads and simulating the path of the beam made sure that the beam did not cross the bridge, see figure 3.7.

ii) Exposing each geometrical shape individually which forces the beam to switch off after writing a single element.

iii) Change of different software settings like using dynamic beam compensation, scan mode during exposure (line by line or meander), direction of writing (horizontal or vertical), area step size and so on.

iv) To reduce the possible chance of a voltage discharge inside the resist, an additional layer of 20 nm thick Germanium was deposited on top of the two resists before

exposure. This metallic layer was connected to the common ground of the EBL system by a metallic plate such that any discharge voltage would be short circuited between the resist and the Germanium layer, i.e. in a vertical direction. After the exposure the Germanium was removed by a dry etching process with $O_2 + SF_6$ gas in the RIE machine before continuing to develop the resists in the usual way.

Significant effort has been put in attempting to control the beam and to try to see any effect by changing many parameters. Nothing was successful and it is considered that the electron-beam is unlikely to be the cause of the problem. Note that some assistance has also been provided from a technician of the company *JEOL* which installed the modified EBL system and also maintained it until recently.

3.6 Conclusions

This chapter explained step-by-step the fabrication of $Al - AlO_x - Al$ Josephson junctions which are connected to gold leads to make later wire bonding possible.
It has been proven that the room-temperature DC measurement setup has to be modified to avoid voltage discharges which destroy the oxide layer of the junction. Furthermore the variation in the normal state resistance R_n can be well explained by the variation of the overlap area.
The original project proposal was the investigation of coherent quantum phase slippage (QPS) in a large array of small Josephson junctions under the influence of an electromagnetic irradiation [2–4, 83, 84]. This original project was in collaboration with the National Physical Laboratory (NPL) in Teddington under the lead of Dr Carol Webster as the NPL is interested in a possible application of such a device as a new metrological current standard. It was therefore necessary to investigate the fabrication of a large number of almost identical small Josephson junctions at RHUL.
A reproducible recipe has been developed with the use of precision measurements to en-

sure quality control of the fabricated small Josephson junctions. The issue of connected leads, possibly due to mechanical stress in the resists, has not yet been completely solved, despite the extensive study. This problem has so far made the prospect of reliable fabricating large arrays of small Josephson junction arrays impossible with this system. More time could be invested into the possible solution of putting a metallic layer in between the two resist layers which acts as a mask but would be less sensitive to mechanic stress compared to the chemical resist mask. Otherwise, the more widely used PMMA/MAA and PMMA resist technologies could be used and optimised. The choice of the resists in this thesis is based on the already successful fabrication of small Josephson junction arrays by the group of Prof D. B. Haviland, see reference [85] for more details.

Chapter 4

Experimental setup

The original plan to use the cryogenic facilities at NPL were inadequate for the project and work was transferred to a dilution refrigerator at RHUL that was already set up for superconducting circuit measurements. However, a leak to the inner vacuum can proved to be difficult to find and cure such that around 6 months later it was decided to commission and install the measurement setup from scratch of a brand new *Cryoconcept* dilution refrigerator. This chapter describes the successful commissioning of a dilution refrigerator which includes the installation of the needed setup to perform superconducting circuit research.

4.1 The cryostat

There are three important parameters which determine the operating temperature needed to measure small Josephson junctions. The following estimations are base on typical parameters for the fabricated small Josephson junctions described in chapter 3 and 5. First, the critical temperature of the superconducting material which is T_c =1.2 K for aluminum in this case. Second, the characteristic energy scales of the Josephson junction which include the plasma frequency $\omega_p = \sqrt{2eI_{c0}/\hbar C_j} \approx 125$ GHz that corresponds to a temperature $T = \hbar\omega_p/k_B \approx 1$ K. Third, the Coulomb charging energy of a single electron

$E_c = e^2/2C_j \cong 45$ mK. This shows that the upper limit of the operating temperature is given by the charging energy of a small Josephson junction.

Besides these intrinsic scales, that give a good indicator for the needed operational temperature, one also has to take into account thermal excitation effects. Thermal excitation effects dominate the escape process above the crossover temperature T_{co}. Thermal effects are also present below T_{co} but are not dominating the escape process such that the aim is to keep the sample colder than T_{co}.

4.1.1 Dilution refrigerator

A detailed explanation of the working principle of a dilution refrigerator can be found in references [86, 87] but for completeness, a short overview of the principle will be given here.

A dilution refrigerator is based on the quantum properties of two Helium isotopes, namely He-4 and He-3. By mixing those two isotopes of Helium and cooling it down to 860 mK they separate into two distinct phases with a concentrated He-3 phase and a diluted He-3 phase. The He-3 rich liquid floats on top of the He-3 diluted liquid. Even at 0 K there is a finite concentration (6.4%) of He-3 in the diluted phase which is the key point to maintaining a finite cooling power at very low temperatures as will be explained later. As the He-4 obeys the Bose statistics it will undergo a so-called *Bose-Einstein condensation* below 500 mK (when it is mixed with He-3) to form a superfluid which is characterised by a negligible entropy but still has a finite volume. The cooling effect is achieved by pumping out the He-3 from the bottom laying diluted phase such that the concentrated phase has to allow He-3 to cross into the diluted phase to maintain the finite solubility limit (6.4%). This process will cause the cooling effect: He-3 has to cross the phase boundary from the concentrated into the diluted phase when mixing the two quantum liquids and this crossing is an endothermic process. The dilution process is maintained in a closed cycle by using circulation pumps, heat exchangers, impedances and pre-cooling stages.

Usually, a so-called *1K-pot* inside the cryostat pre cools the He-3 from 4.2 K to around 1.2-1.5 K by evaporative cooling of He-4 which is thermally connected to the incoming He-3 gas. The refrigerator from *Cryoconcept* (model DR-JT-S-400-10) uses a Joule-Thomson stage which replaces the 1K-pot. The Joule-Thomson effect is used inside the cryostat to directly cool the incoming He-3 gas by forcing it to expand through a nozzle hence decreasing the temperature of the He-3 gas down to 1.2-1.5 K.
The dilution refrigerator from *Cryoconcept* has a measured cooling power of around $400\,\mu W$ at 100 mK. A base temperature of around 12 mK was reached without any wiring. Figure 4.1 shows the schematics of the full dilution refrigerator (left figure) and the bottom part from the 4K-flange to the mixing chamber stage (right figure). The dilution refrigerator provides a lot of space to install the wiring and also RF equipment if needed.

4.2 Wiring

The wiring diagram can be seen in figure 4.2 and it shows the most relevant parts which were installed as part of the setup. Three different materials were used for the wiring: Manganin (86% copper, 12% manganese and 2% nickel), copper and niobium-titanium (NbTi), all with a diameter of 0.1 mm. Copper is a very good electrical conductor and therefore also has a high thermal conductivity which is usually used to apply high currents or very low signal damping. The two twisted-pair copper lines (red line in figure 4.2) were installed to make it possible to later install a superconducting coil to apply a small magnetic field to the sample if necessary. The twisted Manganin wires have a large electrical resistivity but also a low thermal conductivity which is needed when the wiring is a direct connection between the room temperature stage and the sample at the mixing chamber to avoid large heat loads. The niobium-titanium alloy becomes superconducting below 9.2 K and is used to read-out the thermometer at the mixing chamber and the adsorption pump and minimises the conducted heat load to these items (see section 4.3). The resis-

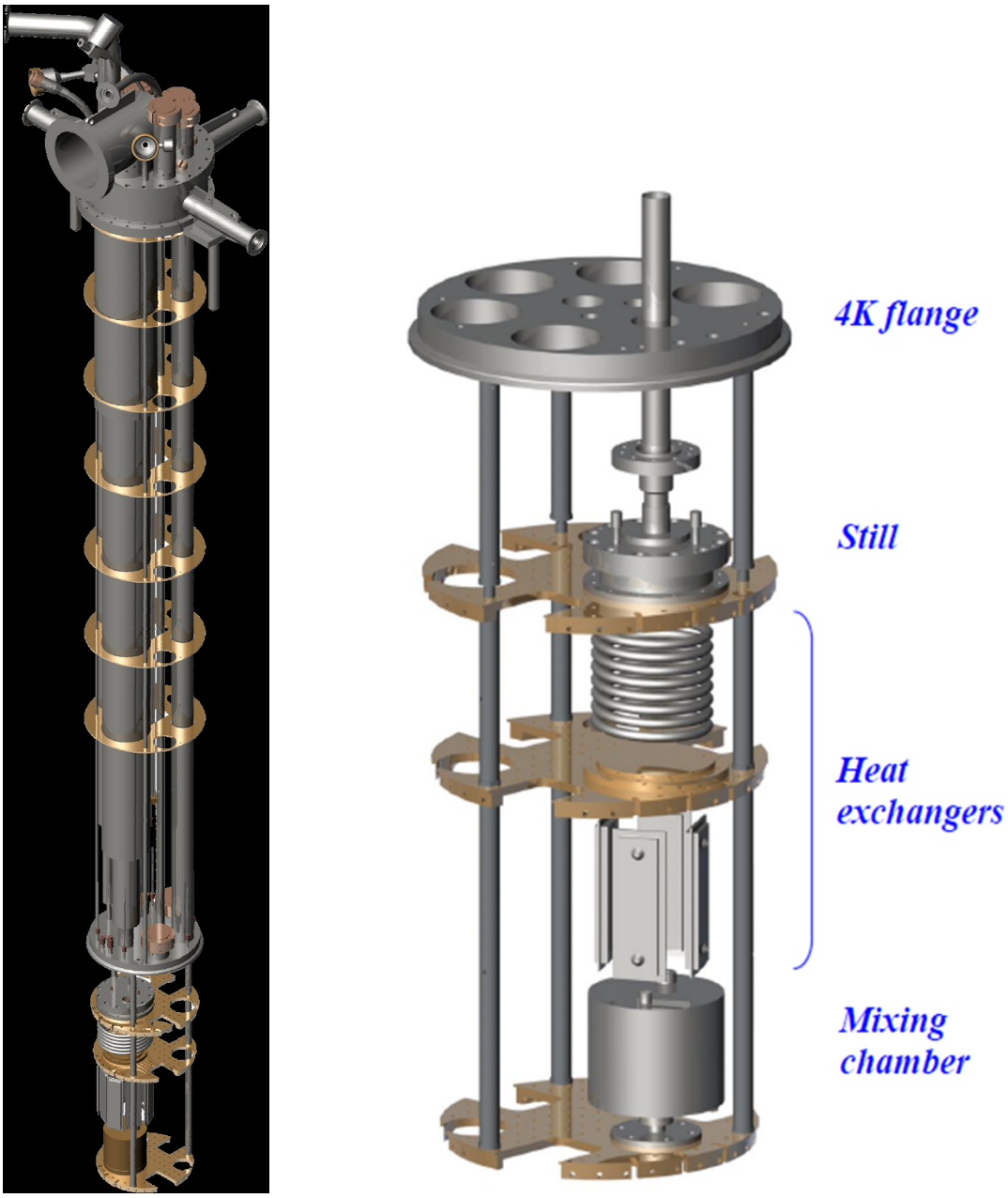

Figure 4.1: Left: Schematics of the full length *Cryoconcept* dilution refrigerator which is inserted in a Helium dewar (not shown here). The six gold plated copper plates on the upper part are radiation shields. Right: Schematics of the lower unit of the left picture showing the part which will be colder than 4 K during operation and is therefore the core part of the cryostat, taken from [88].

tive heater of the adsorption pump is connected to a separate pair of twisted NbTi wires to be able to apply a high current to the heater (see section 4.4 about the adsorption pump

below). All wires are twisted in pairs to avoid pick-up voltage induced by oscillating magnetic fields, with a *Teflon (PTFE)* sleeve protecting them from mechanical damage. All wires which are connected to the sample holder are inside a copper-nickel tube (outer diameter 1.4 mm, inner diameter 1 mm) which acts as a *Faraday cage* to shield the wires from electrical fields and each other. Furthermore, CuNi has a low magnetic permeability which makes it almost transparent for magnetic fields and therefore makes this material very suitable for low temperature physics as it will not disturb any applied magnetic field. At room temperature, a breakout box with 36 BNC connectors is fed into the top of the dilution refrigerator via two 18-pin *Fischer* connectors. All outer connectors of the BNC plugs share the common ground of the refrigerator. Connection between any instrument and the BNC plugs of the breakout box are made via SMA cables with a BNC adapter on each end. Tests showed the least amount of piezoelectric and microphonic noise when using SMA cables. The wiring itself then runs from the room temperature stage to 4 K inside an evacuated stainless steel pipe. At the 4 K stage, all CuNi tubes are thermalised by clamping the tube to a copper frame (see figure 4.3, c) and d)). The wires which do not have an additional CuNi-shielding were just wrapped and glued (GE varnish) onto a copper cylinder (see figure 4.3, e)). A second thermalisation is performed at the still stage (around 600-800 mK) at which the wires inside a CuNi tube are thermalised by wrapping them around a copper cylinder which is placed inside a copper box and connecting the wires then to a 4-pin *Fischer* connector on the other side of the box (see figure 4.3, a) and b)). This allows to continuously shield the wires. The CuNi-tubes themselves are also thermalised at the still-stage. All other wires which are not inside a CuNi-tube are just wrapped around copper bobbins at the still stage and soldered to a D-connector. The last thermalisation takes place at the mixing chamber stage at which the CuNi shielded wires are connected to a microcoax stainless steel (SS-SS) filter via 4-pin *Lemo* connectors (see section 4.6 for more information). All other wires are again thermalised by using copper bobbins.

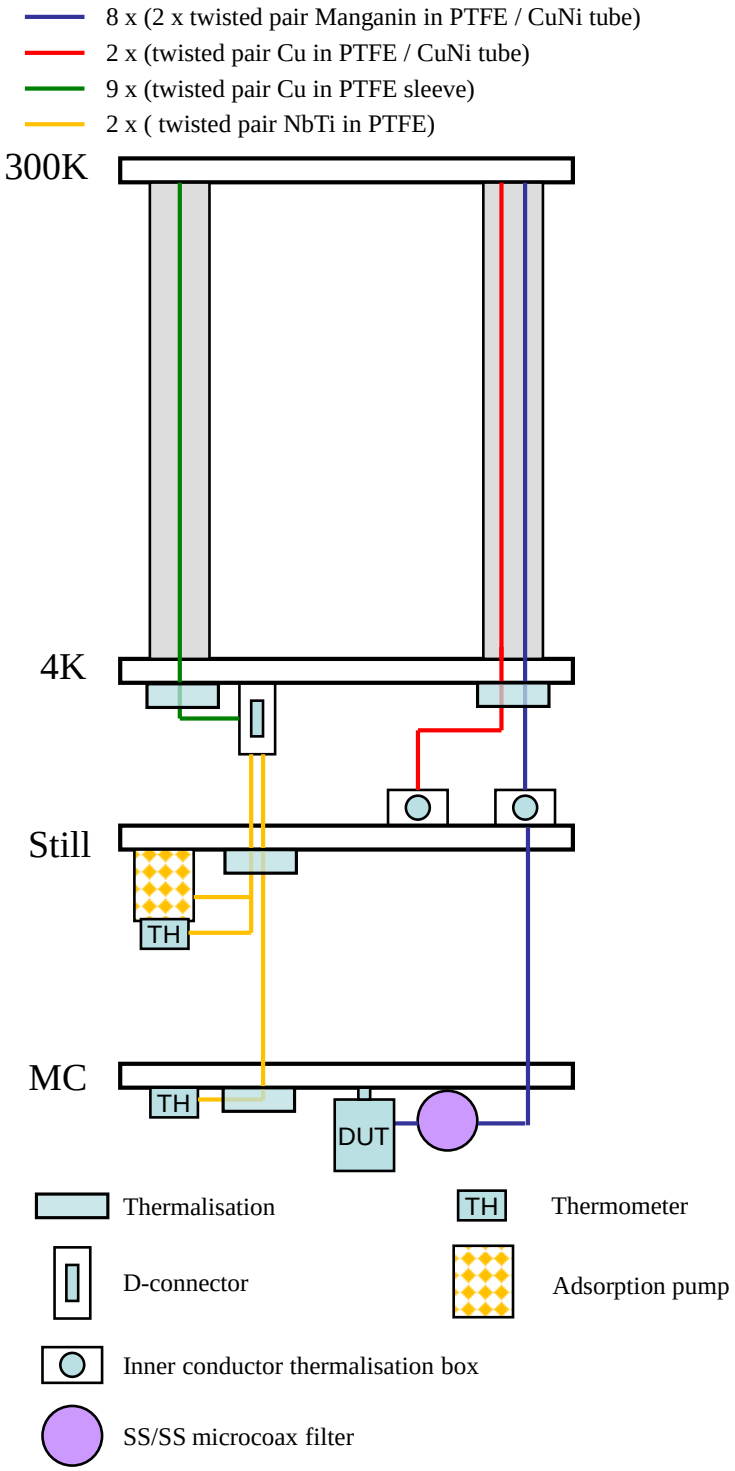

Figure 4.2: Wiring diagram and additional installed components of the dilution refrigerator like the adsorption pump, thermometers, low temperature microcoax filters and thermalisation stages. The sample holder contains the device under test (DUT).

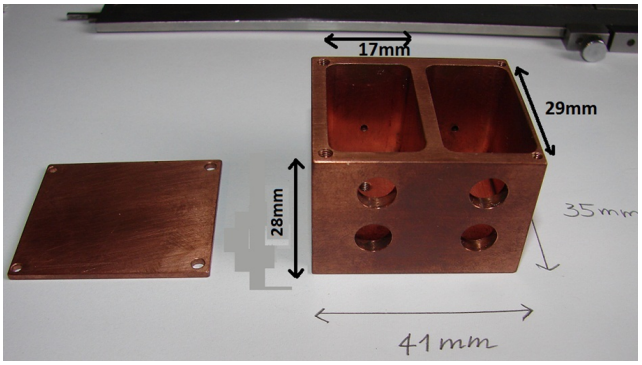

(a)

(b)

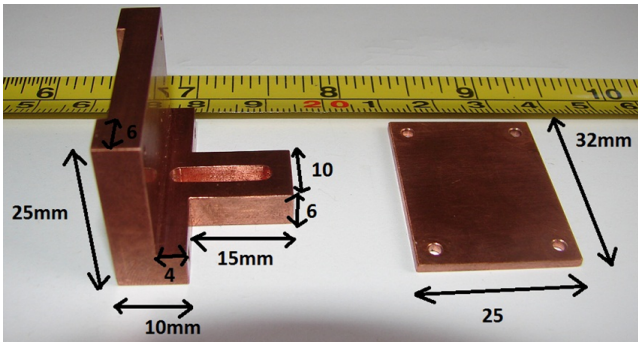

(c)

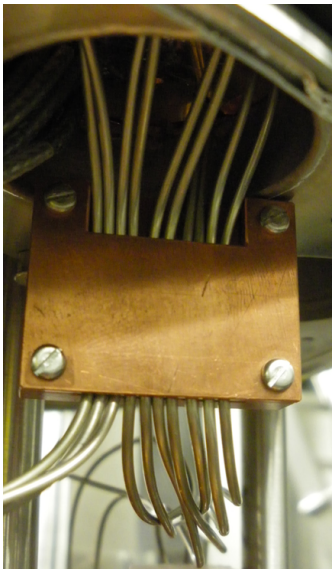

(d)

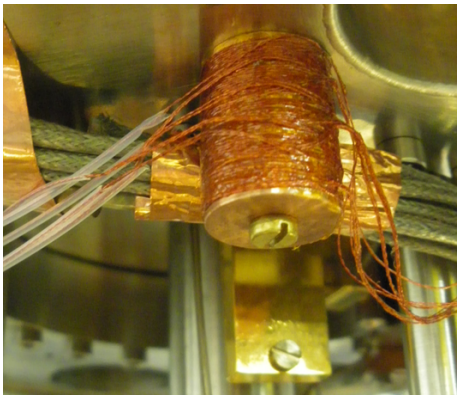

(e)

Figure 4.3: a) Thermalisation box (still stage) with cover both made of copper. The large circular holes (a) give access via 4 pin *Fischer* connectors to the inside in which each pair of wires is wrapped around a copper cylinder (b) to thermalise them. The CuNi tubes are connected to the box via small through holes. c), d) Copper thermalisation clamp which thermalises the CuNi tubes at 4 K. e) Copper bobbin which thermalises the wire by wrapping them around around the cylinder and fixes the wires by a low temperature glue (GE varnish).

4.3 Thermometers

The commissioning of the dilution refrigerator required the installation of three fixed thermometers at the following stages: mixing chamber, still and adsorption pump. In the following, the read out of the thermometers and the calibration of the mixing chamber thermometer are described as well as the installation of the adsorption pump thermometer.

The read out of all thermometers was done by an AC resistance bridge from *Stanford Research Systems* (model *SIM 921*). The frequency of the signal is 10 Hz with a reading rate of 2 updates/s which, together with an adjustable excitation voltage in the range of $3\,\mu V$ to $30\,mV$, minimises the power input. The 4-terminal configuration separates the current and voltage leads in order not to measure the lead resistances. The resistance bridge is grounded to the common ground avoiding ground loops in the measurement circuit. The AC resistance bridge is controlled by a *LabView VI*. This LabView VI allows the read out of two thermometers at the same time with a freely adjustable read out period (the standard value is 15 s). Furthermore, the excitation voltage, as well as the resistance range [$20\,m\Omega$, $20\,M\Omega$], can be selected in the software to reach the highest possible sensitivity. The read out value for each chosen time period is written into a text file that includes the name of the thermometer, the time stamp and the measured resistance values of the two selected thermometers. Those values are also plotted in real time in the LabView VI.

All the installed resistive thermometers have to be calibrated in order to assign to each measured resistance a temperature. The calibration of the installed mixing chamber thermometer (TMC) from *Cryoconcept* is the most critical part as this indicates the temperature of the sample. The TMC is a Ruthenium oxide thermometer (RuO2) and had to be calibrated over a wide temperature range (300 K to 60 mK). This type of resistance thermometer has the advantages of good reproducibility, small size, small mass and is of low cost [86]. In order to calibrate the TMC it was necessary to install two other, already

$a_0 \longrightarrow 7.924 \pm 0.003$
$a_1 \longrightarrow -0.323 \pm 0.004$
$a_2 \longrightarrow 0.065 \pm 0.001$

Table 4.1: Fitting parameters of the interpolation in the low temperature range of the TMC.

calibrated thermometers next to it. A first calibration was done from 300 K down to 200 mK by attaching an already calibrated thin-film ceramic zirconium oxynitride (Cernox) thermometer to the mixing chamber. In a second step, another RuO2(2) thermometer was used to calibrate the low temperature range from 1.2 K to 60 mK. The RuO2(2) thermometer was glued (Ge varnish) onto a cylindrical copper holder and the 10 cm copper wires of the leads wrapped around the bobbin. This is important as the leads thermalise the thermometer and therefore are critical for a good thermal contact to the mixing chamber. The copper leads were then connected to the NbTi-superconducting wires which go up to 4 K before connecting them to the thermalised copper wire up to room temperature. This 2-step calibration is shown in figure 4.4. The measured resistance of the fixed installed TMC is plotted versus the calibrated thermometers. The red circles show the temperature of the Cernox thermometer and the blue circles the one of RuO2(2). Notice the overlapping range between 1.2 K and 200 mK which is in good agreement for the two different calibrations. One has to mention that RuO2(2) itself is part of a whole batch of the same kind of RuO2-thermometers which have a general calibration with a Germanium *Lakeshore* thermometer. The highly non-linear response of the TMCs resistance at low temperatures (<1 K) can be fitted by the following empirical function [86]

$$R = \exp\left(\sum_{n=0}^{2} a_n \cdot (\ln(T))^n\right) \tag{4.1}$$

$$T = \exp\left(\frac{-a_1 - \sqrt{a_1^2 - 4a_0a_2 + 4a_2 \ln(R)}}{2a_2}\right) \tag{4.2}$$

$a_{0,1,2}$ are constants that are extracted by fitting this model to the measured curve in figure 4.5. The values given in table 4.1 are the best fit values

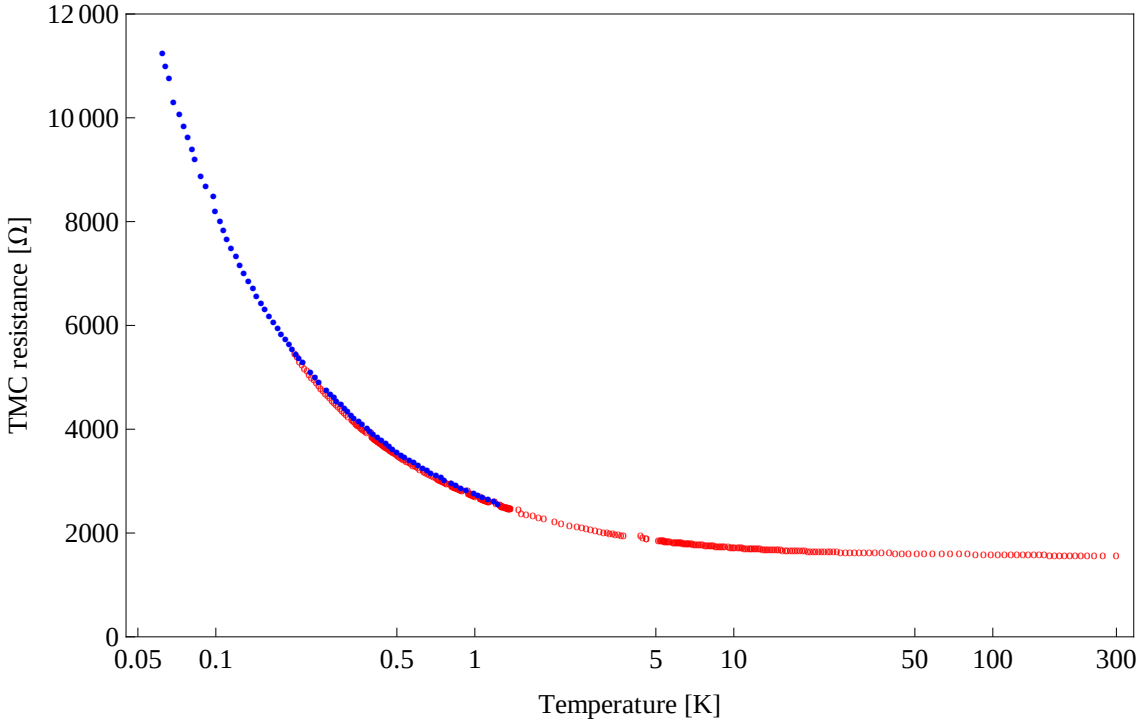

Figure 4.4: Mixing chamber thermometer calibration. The high temperature range (red points) were calibrated against a Cernox thermometer whereas the low temperature range (blue points) were calibrated against another, already calibrated RuO2 thermometer. The relative error for R_{TMC} $\leq$10 kΩ is 0.1% and for R_{TMC} $>$10 kΩ the relative error is 0.3%. The error bars are within the point size.

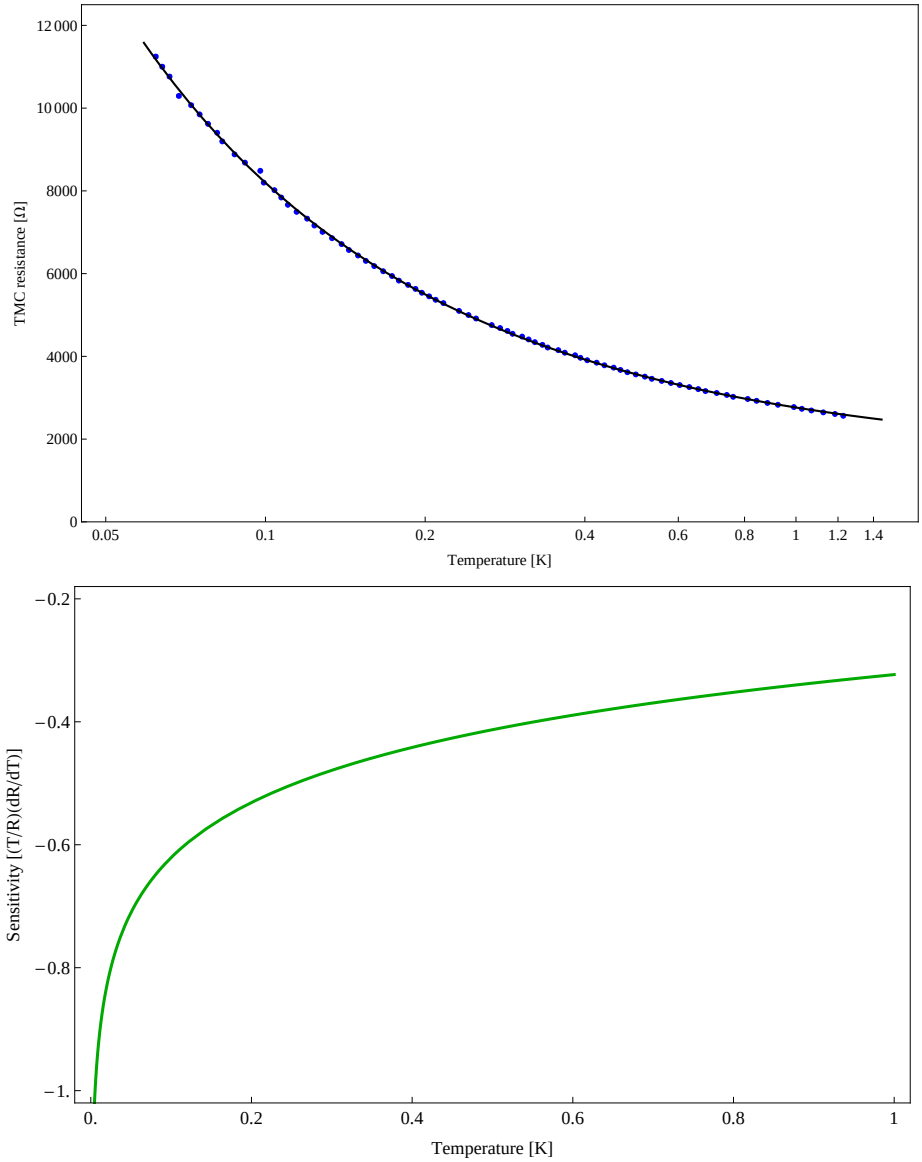

Figure 4.5: Top: Low temperature calibration curve of the TMC (blue dots) which were fitted with an empirical equation (black curve). The fitted model can be used to extrapolate the temperature range below 60 mK. The relative error for R_{TMC} $\leq$10 kΩ is 0.1% and for R_{TMC} $>$10 kΩ the relative error is 0.3%. The error bars are within the point size. Bottom: Sensitivity of the TMC (RuO2) thermometer calculated from empirical fit above. A large increase in the sensitivity below 200 mK indicates a sensible choice of thermometer at the mixing chamber stage.

Such an empirical fit allows to extrapolate temperatures below 60 mK based on the measured resistance of the TMC. Another important parameter for any type of thermometer is the sensitivity for a certain temperature which is defined by [86]

$$Sen(T) = \frac{T}{R}\frac{dR}{dT} \tag{4.3}$$

Usually each type of thermometer has a high sensitivity in a limited temperature range and it is therefore important to use the correct type of thermometry for each temperature stage. Out of the empirically fitted low temperature calibration (equation (4.1)) for the calibrated TMC the sensitivity is derived and plotted in the lower panel of figure 4.5. As can be seen, the sensitivity is very high below around 200 mK which justifies the choice of the TMC. The highest resistance value of the TMC that was measured (with the complete wiring installed) was around $33\,\mathrm{k}\Omega$ and corresponds to 15 mK. That is 3 mK more than what was measured without the wiring of the dilution refrigerator and shows the small heat load from room temperature. The resistance of the TMC steadily increased down to the base temperature and did not show any sign of thermal decoupling. The accuracy of the resistance measurement for $R_{TMC} \leq 10\,\mathrm{k}\Omega$ is 0.1% and for $R_{TMC} > 10\,\mathrm{k}\Omega$ it is 0.3% (given by the datasheet of the manufacturer). The wiring of the TMC has a neglible heat load from 4 K down to the mixing chamber stage as NbTi wires are used. The heat load is also reduced by using a relatively small excitation voltage of $10\,\mu\mathrm{V}$. It is therefore unlikely to exceed an uncertainty of 1 mK at temperature of around 20 mK.

The thermometer which is attached to the adsorption pump is a *Vishay* CLTS-2B. This thermometer shows a linear behaviour of temperature as a function of the resistance R from room temperature down to liquid helium temperature as $T_{sorb} = 4.18429\,K/\Omega \cdot R - 916.393\,K$ as given by the datasheet of the manufacturer. The sensitivity is $Sen(T) = T/(T + 916.393\,K)$ and is therefore approximatively linear in temperature and not very large (<0.25). However, it is well suited for resolving temperatures in the range of (15-40)

K. More details can be found in section 4.4.

4.4 Adsorption pump

During the cool down procedure the IVC, as well as the stainless steel pipes that contain wires from room temperature, have to be evacuated. This is done with an external powerful turbo molecular pump that takes a couple of hours to reach a pressure in the desired 10^{-4} mbar range. Next, several milliliters of He-4 exchange gas is inserted into the IVC. The core of the dilution refrigerator is then slowly inserted into the He-4 bath (4.2 K) such that any residual gas inside the IVC (except helium) will freeze at the wall of the IVC. By observing the temperature of the still and the mixing chamber stage one can observe the thermalisation process which was usually done over night.

Before starting the closed circulation of the He-3/He-4 mixture to further cool down the dilution unit it is necessary to pump out the exchange gas. This can either be done with an external pump (turbo molecular) or with a so-called adsorption pump. As the exchange gas is at 4.2 K and far away from the room temperature pump, it would take a significant amount of time ($\approx$ 12 h) to evacuate the IVC. This time can be reduced to seconds by using an adsorption pump instead. Such an adsorption pump is made of a very porous (large surface area in the order of several $\mathrm{m}^2\,\mathrm{g}^{-1}$) activated charcoal. This material binds a large number of gas molecules including Helium via the van der Waals force. The adsorption of Helium strongly depends on the temperature of the activated charcoal which is strongly absorbing below 15 K, but releases most of the Helium in the range between 15-40 K [86]. The absorption pump is a very powerful pump at low temperatures and can even absorb Helium from very tiny leaks in the setup (assuming the pump is not saturated).

Such an adsorption pump was built by gluing activated charcoal onto a thin (1.5×1.5) cm^2 copper plate. A heater was attached by wrapping *Manganin* around a copper bobbin with a total resistance of $1\,\mathrm{k}\Omega$. This is connected to a twisted pair of superconducting

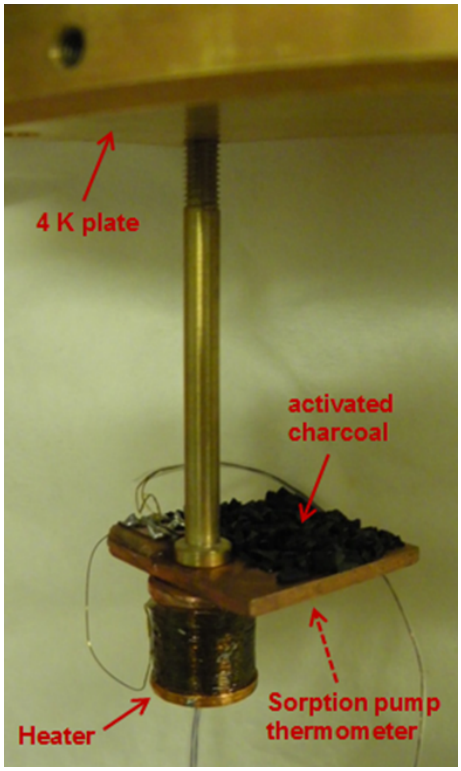

Figure 4.6: Built adsorption pump with a 1 kΩ resistive heater, a thermometer (*Vishay CLTS-2B*) and activated charcoal on top of the copper plate. The rod which connects to the 4 K plate is made of brass to provide a weak thermal contact between the 4 K plate and the copper plate.

NbTi wires via a small PCB nearby. At the 4 K stage the NbTi wires are connected to a twisted pair of thermalised copper wires which go up to room temperature. To measure the temperature of the adsorption pump a thermometer from *Vishay* (model *CLTS-2B*) was installed on the other side of the copper plate. A brass rod with a much lower thermal conductivity than copper thermally isolates the adsorption pump from the 4 K plate in order to be able to heat the pump above 15 K.

Figure 4.6 shows the installed adsorption pump. This device was tested during the pre-cooling process when the dilution refrigerator was inserted into the 4 K bath. Initial results indicate that the adsorption pump is working correctly, but it has not yet been possible to demonstrate its effectiveness in adsorbing the exchange gas, as there was a small leak at the IVC. The leak was successfully repaired, but a further test of the adsorption pump has not yet been done.

4.5 Instruments

In this section the instruments used to perform measurements of Josephson junctions will be described and their specifications given. The general schematics of the setup will be shown and described. As part of commissioning the dilution refrigerator, it was necessary to write software to control the whole pumping system including valves, vacuum pumps, compressor, pressure gauges, helium level meter, emergency stop and so on. Although the manufacturer supplied a software control system, a separate software had to be written as it was not possible to get access to the original algorithms as well as the lack of sufficient documentation of it.

4.5.1 Software control of the pumping system

The pumping system of the *Cryoconcept* dilution refrigerator is localised in an external room to reduce both acoustic noise and mechanical vibrations. The external room is equipped with an electrical defroster to keep the temperature well above 0 degrees Celsius. Condensation water on critical parts like rubber sealing rings or pneumatic valves, is prevented from freezing which could otherwise damage them. Panel a) in figure 4.7 shows the pumping system of the dilution refrigerator, that includes several pneumatic valves, as well as some manual control valves, a compressor, a rotary pump, two Roots pumps, several pressure gauges, two overpressure safety valves, an emergency stop, the dump which contains the He-3/He-4 mixture and a liquid nitrogen cold trap. All those devices are connected to a *WAGO* electronic control unit that also includes a fuse box. Panel b) in figure 4.7 shows the *WAGO* system which can be connected via a LAN cable to a computer located in the laboratory. As part of commissioning the *Cryoconcept* dilution refrigerator it was necessary to write a *LabView* program to have full control over all of these components. The block diagram of the dilution fridge control LabView VI can be seen in the bottom panel of figure 4.7. The black lines represent the vacuum pipes, the

(a)

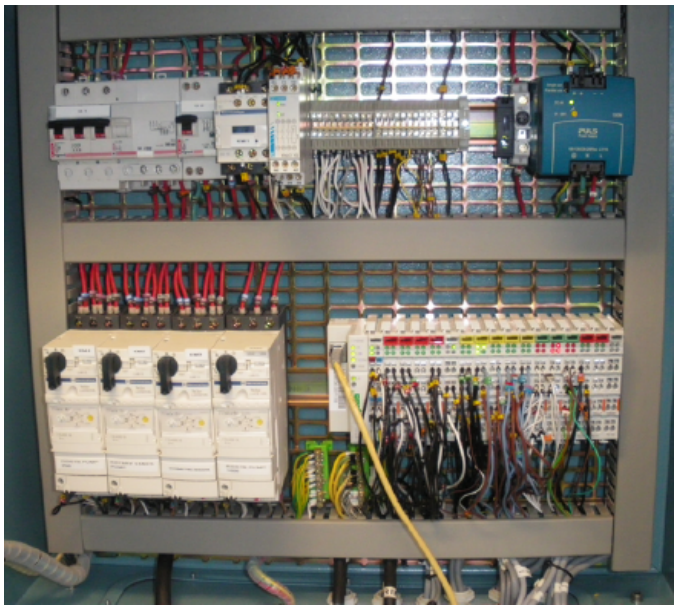

(b)

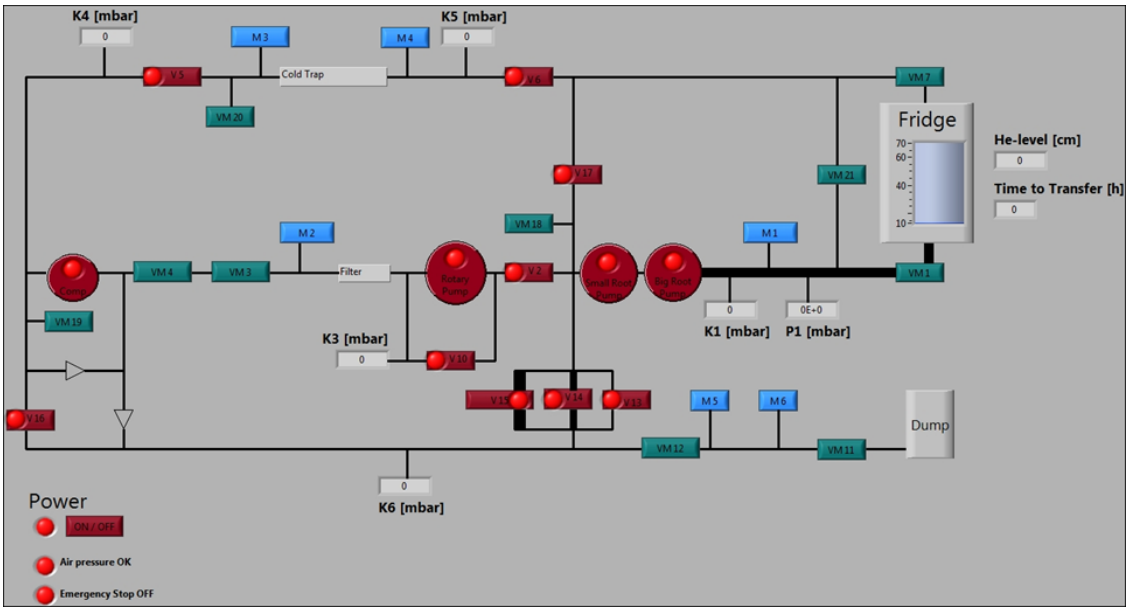

(c)

Figure 4.7: a) Pumping system of the *Cryoconcept* dilution refrigerator which is in a separate room from the experiment to reduce acoustic noise and mechanical vibrations. b) The *WAGO* system controls most of the pumps, valves, compressor and so on, but it also continuously returns the measured values of the pressure gauges and the level of the liquid He-4 inside the dewar. c) The block diagram of the written VI that allows full control of the *WAGO* system.

green buttons the manual valves (included for completeness), the red buttons are valves that can be controlled in the software. The blue rectangles represent analog pressure monitors (again shown for completeness), the digital pressure gauges are labeled by K or P and directly read out the corresponding pressures. The large red circles are either powerful vacuum pumps or a compressor. Besides the control of these devices, the *WAGO* system monitors and reports the current state of the valves and the pumps/compressor by the small circular lights next to the buttons (red for closed/off and green for opened/on). The code also permanently monitors the air pressure that activates the valves, as well as the liquid He-4 level inside the dewar. A separate VI was written to only read out the state of the pumping system without setting any parameter. This can be used in case of a power cut or if anybody pressed the emergency stop button and the system has to be restarted.

4.5.2 General setup of the measurement system

A schematic of the measurement setup can be seen in figure 4.8. It is, in essence, a simple four terminal measurement but very carefully constructed to take account of shielding and eradicating unwanted spikes. The voltage signal is applied by an arbitrary waveform generator (AWG) and it is then passed through a bias resistor R_b =1 MΩ (sometimes a voltage divider, consisting of two resistors in series, is used with $R_1 = 120 \pm 1$ ohm and $R_2 = 10110 \pm 91\ \Omega$, such that the signal is divided by a factor of 85.2 ± 1.5). The current signal is injected through the twisted and shielded Manganin pairs and thermalised at the still stage (around 600-800 mK) before it is filtered by cryogenic microcoax filters, that are thermalised at the mixing chamber stage (15-20 mK). The voltage response of the device under test (DUT) propagates through the same wires up to room temperature where it is amplified by a gain G (usually 60 dB) and also low-pass filtered before it is analysed by an oscilloscope and/or universal counter and stored on a computer by a data acquisition system (DAQ).

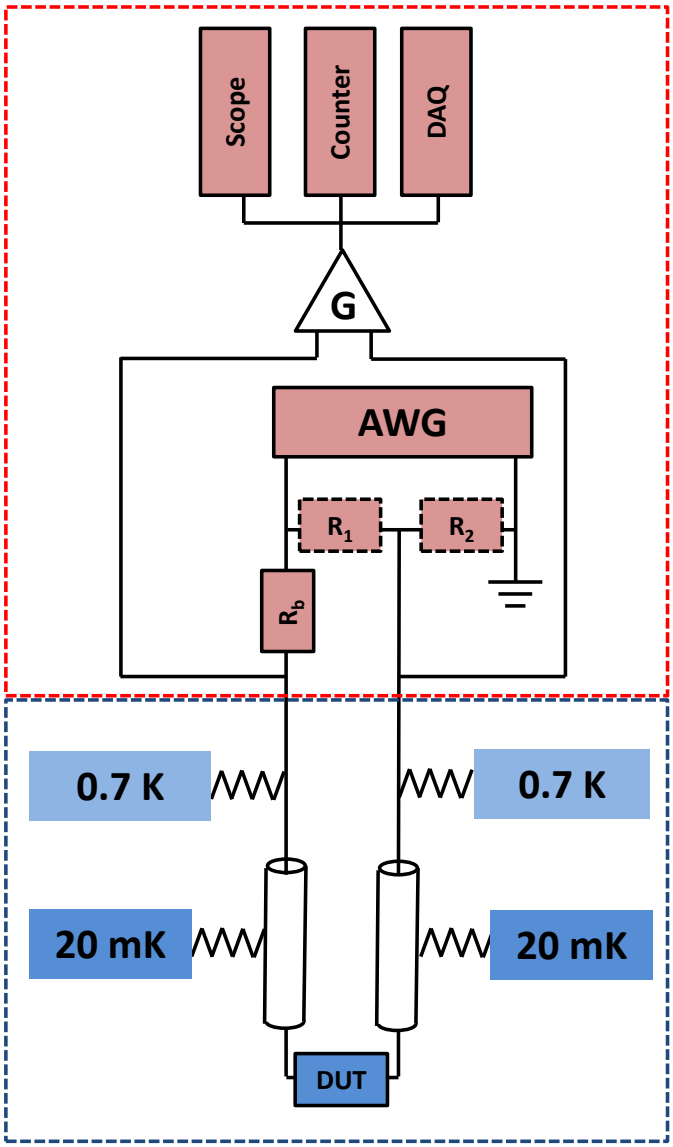

Figure 4.8: Schematics of the measurement setup of the device under test (DUT). The red dashed box shows the setup at room temperature whereas the blue dashed box indicates the installations inside the dilution refrigerator. The thermalisation stages are indicated as well as the microcoaxial filters. A voltage divider is occasionally used with $R_1 = 120 \pm 1$ ohm and $R_2 = 10110 \pm 91\ \Omega$. The bias resistor R_b =1 MΩ is installed to transform the voltage signal of the arbitrary waveform generator (AWG) into a current signal. The read out is performed by a room temperature amplifier (with gain G) which also includes a low pass filtering stage before it is sent to several instruments (data acquisition (DAQ), scope and/or universal counter).

4.5.3 Arbitrary waveform generator (AWG)

To generate an arbitrary waveform, the model *33250A* from *Agilent* was used. This instrument has 12-bit amplitude resolution, 200 MSa/s. Any waveform up to 64000 points can be defined. This can be done in a *LabView VI* and then uploaded onto the AWG via a GPIB connection. It is sometimes necessary to trigger the defined pulses by an external trigger to create a pulse train. For this purpose a separate function generator is used (*SRS DS345*).

4.5.4 Function generator

A function generator (*Stanford Research System, DS345*) was installed to trigger other instruments. This was mainly used to create a continuous rectangular waveform with a $50\,\%$ duty cycle, compatible to the TTL (transistor-transistor logic) signal with a well defined frequency. This instrument is relatively easy to use and is able to create several predefined waveforms (sine, square, ramp, triangle, noise) with a peak-to-peak amplitude from $10\,\mathrm{mV}$ to $10\,\mathrm{V}$ into a $50\,\Omega$ load. For ramp and triangle shaped output signals a frequency from $1\,\mu\mathrm{Hz}$ to $100\,\mathrm{kHz}$ can be chosen whereas for sine and square signals this range is limited to $1\,\mu\mathrm{Hz}$ to $30.2\,\mathrm{MHz}$.

4.5.5 Digital oscilloscope

A digital oscilloscope is used as a standard analysing instrument to either check the applied signals or to record the response signal of the device under test. The *Agilent DSO81004A Infiniium* has 4 input channels with a 8 GHz real-time bandwidth and a maximum sampling rate of 20 GSa/s each. The vertical sensitivity ranges from 1 mV/div to 1 V/div with a $50\,\Omega$ input impedance. This oscilloscope was also very useful for checking that the triggering signals were set correctly, as well as for setting the threshold voltage of the universal counter. This oscilloscopes offers a wide range of mathematical analy-

sis tools including recording histograms, performing fast Fourier transformations (FFT), taking the root mean square of the signal input and many more.

4.5.6 Universal counter

The main purpose of the universal counter *Agilent 53132A* was to count the number of switching events of a Josephson junction from the superconducting state to the resistive state. The counter was externally triggered to start measuring the input signal, for a certain time. It compares this signal to a set threshold to decide if a switching event occurred or not. The instrument is able to measure frequencies up to 225 MHz on two separate channels. The time resolution is 500 ps and it can perform up to 200 measurements per seconds. The input signal (peak-to-peak) for pulses longer than 10 ns has to be in the range of $50\,\mathrm{mV}$ to $10\,\mathrm{V}$ whereas the input impedance can be changed between $50\,\Omega$ and $1\,\mathrm{M}\Omega$. In case of an overlarge input signal it is possible to use a 20 dB (amplitude factor 1/10) attenuator. Furthermore it provides the following basic measurement functions: frequency, period, pulse width, duty cycle, rise/fall time, time interval, frequency ratio, totalize, phase and peak voltage.

4.5.7 Room temperature amplifier and low-pass filter

A room temperature amplifier from *Stanford Research Systems (SRS)*, *SR640* is used to amplify the voltage response of the low temperature device and also to low-pass filter it. This instrument has two independent channels, each with a programmable low-pass filter (ranging from 1 Hz to 100 kHz) preceded by a low-noise pre-amplifier ($10\,\mathrm{nV\,Hz^{-1/2}}$ at 1 kHz with 60 dB input gain, given by the manufacturers specification) with a selectable gain of 0 dB to 60 dB. The maximum input signal (either single-ended or differential) is $10\,\mathrm{V}$ peak to peak with an impedance of $1\,\mathrm{M}\Omega$. The maximum output signal is $10\,\mathrm{V}$ peak to peak and the DC offset can be adjusted manually. Another important fact is that

the BNC connector shields (input) of the amplifier are not connected to the unit's chassis ground, which allows them to be separately grounded to the common ground. Usually a gain of 60 dB is used in the DC coupling mode with an input filter in the low kHz-range. The output of the amplifier is then connected to the DAQ board (in parallel with other instruments like oscilloscope or universal counter) which then reads out the amplified signal.

4.5.8 Data acquisition

To read out the amplified and filtered voltage signals, a data acquisition (DAQ) board from *National Instruments* is used. The *DAQ BNC-2090* has 22 BNC connectors of which 16 are single-ended analog input channels (8 if used in differential mode), 3 are analog output channels and another 3 are digital input and output channels. The sampling and control of the DAQ is done by a 16 bit resolution, 250 kS/s PCI board from *National Instruments* (*NI PCI- 6221*) which has a maximum voltage range of ± 10 V. The whole data acquisition and recording is done by a *LabView VI*. It is also possible to use the analog output channels of the DAQ board to directly set a voltage signal, passed through a bias resistor before being sent down to the sample. This method is more compact and simpler in terms of writing the corresponding computer control than using the AWG but it has the disadvantage that triggering the signal becomes more difficult.

4.6 RF Filters

At millikelvin temperatures, the dynamics of Josephson junction based devices is greatly affected by their environment. For this reason, it is extremely important to filter the electromagnetic noise that arises from hotter temperature stage and propagates down the experimental wiring. Interactions with high energy photons (from the lead or incident from the vacuum) may drastically affect the V(I) characteristic of especially small Josephson

junctions. Since, in our case, all the superconducting materials are made of aluminium the frequency corresponding to the superconducting energy gap Δ is $2\pi\Delta/e\hbar \approx$50 GHz. The Johnson noise arising from the room temperature experimental setup has a white spectrum extending up to about $2\pi k_B T/\hbar \approx$6 THz. This means that even when the junction is biased at a current below its critical value, photons can cause breaking of a cooper pair resulting in a quasi-particles current and a finite voltage will develop across the junction below V_g. Hence inserting the filters at the lowest temperature stage will limit the noise frequency spectrum and shows a visible effect in the electrical characteristic of such devices. To determine the desired cut-off frequency of the filter, one uses the argument outlined at the beginning of section 4.1 (i.e. the typical plasma frequency of a small Josephson junction is around 50 GHz which corresponds to a temperature of approximately 400 mK).

Resistive microwave coax cryofilters were built and mounted in order to cut off high frequency noise ($\gg$ 5 GHz) on the input DC lines to the sample. This type of filtering was proposed and tested by A. B. Zorin [89] in 1995 for a single-electron experiment. It consists of a high-resistance inner conductor which is surrounded by a tubular dielectric material and an outer conductor jacket. The coaxial cable has a small diameter (<1 mm) and acts as a low-pass filter for frequencies below a couple of GHz.

Commercially available heating wire known as *Thermocoax*, as demonstrated by Zorin [89], has a NiCr central wire with the dielectric space made of MgO powder and it has stainless steel outer conductor jacket. In order to prevent air moisture leakage and mechanical separation from the inner and outer conductors, the wires must be sealed with epoxy as MgO tends to absorb moisture causing a short between the inner conductor and outer stainless steel. In addition, silver epoxy has to be used for soldering the NiCr central wire. This makes it very difficult to solder any connector to the inner NiCr wire. It was therefore decided to fabricate and test a similar device but with the inner and outer conductor made of stainless steel 304 (SS) which has a high resistivity similar to NiCr but

Outer conductor diameter	(0.508 ± 0.0254) mm
Dielectric diameter	0.381 mm
Inner conductor diameter	(0.114 ± 0.0127) mm
Impedance	$(50 \pm 2)\ \Omega$
Capacitance	95.1 pF/m

Table 4.2: Manufacturers specification table of the coaxial lines from the company *MICRO-COAX* (UT-020-SS-SS) made of a stainless steel center conductor which is separated by a PTFE dielectric to the stainless steel jacket.

is easier to solder. The coaxial cables were ordered from *MICRO-COAX* , model UT-020-SS-SS. The key parameters are summarised in table 4.2. The dielectric which electrically isolates the center conductor and the jacket of the coaxial cable is made of PTFE.

Other possible implementations of such a filtering would be 1) a copper powder filter [90], with the high frequency attenuation resulting from the skin-effect given by the large surface area of the copper powder or 2) an on-chip RC microwave filtering consisting of a meander line made of AuCo (using a lithographic process), surrounded by silicon nitride placed inside a brass box to protect it from irradiation [91].

Several reasons make the coaxial cables a suitable device for our needs [89]. First, the high DC resistance of stainless steel 304 guarantees dissipation over a large temperature scale, second no additional external screening is necessary due to the already existing outer metallic jacket. The attenuation spectrum can be calculated using the geometrical dimensions of the coaxial cables and the properties of the materials. By contrast, such a precise calculation is not possible for the copper powder filters.

The thermalised Manganin wires are then connected to the center connector of the microcoax filter (thermalised at the mixing chamber stage) via a 4-pin *Lemo* connector. The outgoing DC-lines are then directly connected to the sample holder via *Lemo* connectors, see figure 4.9.

(a)

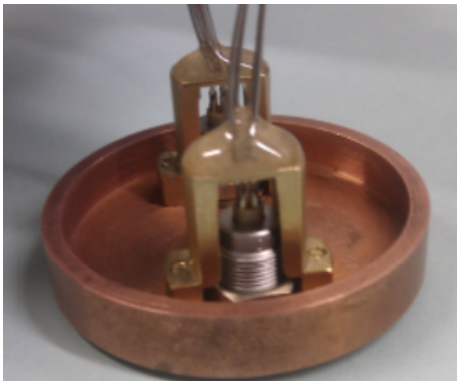

(b)

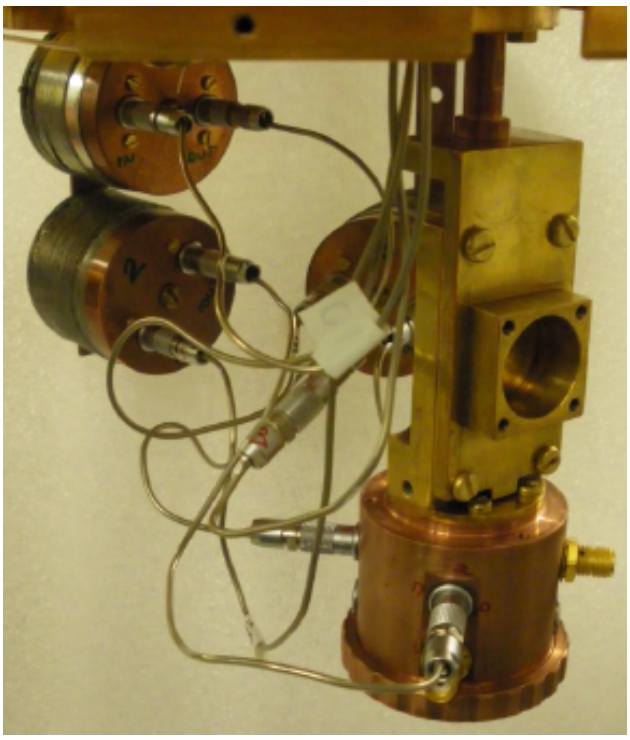

(c)

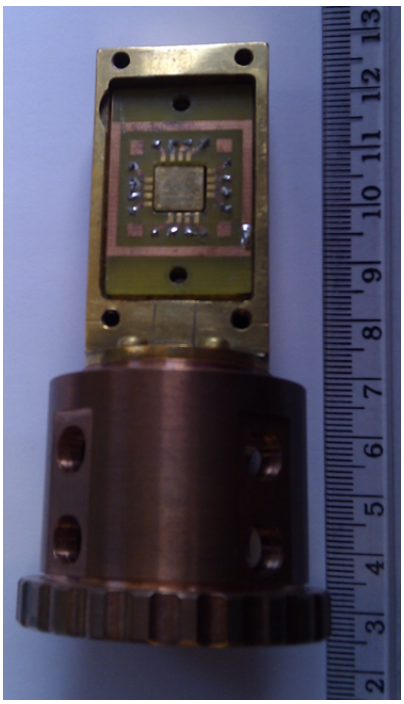

(d)

Figure 4.9: a) Two of the four filters, each with 4 coaxial cables wrapped around a copper cylinder which is attached to the mixing chamber stage. Four 4-pin connectors were used to later connect the incoming DC-lines to it. b) Cover of the filter which show the input and output connector of a single filter. As the stainless steel coaxial cables are very springy they have to be held in place by a little frame through which the cables are inserted and fixed with a low temperature glue. c) Mixing chamber stage showing the installed filters on the right back which are connected via short shielded (CuNi tubes) cables to the sample holder. d) Inside of the sample holder showing the PCB which is connected to the sample via aluminium wire bonds.

4.6.1 Recipe to thermalise the stainless steel micro coax cables

Four coaxial cables were wrapped around a copper cylinder with an outer diameter of 40 mm, a length of 30 mm and a wall thickness of 2 mm in order to thermalise them at the coldest point of the dilution refrigerator. It is critical to pre-coat (also called tinning) the surface of this cylinder with a multi core 60/40-tin/lead solder and wet it with the special liquid flux, *Superior No. 23*. Before tightly wrapping around the coaxial cables one has to prepare them.

Stainless steel is difficult to solder due to the presence of an oxide film and the low thermal conductance. It is therefore important to prepare the surface carefully and tin it beforehand. Each micro coax cable of 1.5 m length was prepared in the following way:

1. Clean with acetone
2. Roughen and clean the surface with *Scotch Brite*
3. Apply flux *Superior No. 23*
4. Tin surface with multi core 60/40-tin/lead and use a low temperature of around $200°C - 220°C$ for the solder iron
5. If necessary apply more flux and solder
6. Wet the cable with the flux *Superior No. 23* and let it dry

It is critical to not exceed the given temperature range of the solder iron due to the outer conductor integrity temperature of the coaxial cable, which according to the manufacturer is $175°C$.

In a next step, the tinned coaxial cables have to be wrapped around the solder-coated copper cylinder. Here, 4 coaxial cables were wrapped around one copper cylinder which has to be done carefully in order not to do irreversible damage to the cables by bending them too much. Due to the springy properties of the cables, metallic clamps were used

to fix them to the cylinder with a piece of PTFE in between in order to avoid squeezing and scratching the sensitive jacket of the cable. Small holes were drilled in the two ends of the copper cylinder in order to pass the cables along the inside of the copper cylinder after they were wrapped around it.

A temperature-controlled hot plate was used to heat-up the whole copper cylinder with the mounted cables on it. Slowly increasing the temperature to $200°C - 220°C$ made it finally possible to melt the pre-coated solder and it could be spread over the surface of the wrapped cables with a wooden stick and *Superior No. 23* .

In order to solder the four inner stainless steel core wires of the coaxial cable into a 4-pin panel-mounted *Lemo* connector, an ad-hoc holder is mounted to keep the coaxial cables in place. The holder, made of brass, has 4 holes for passing the cables through. The holders and the *Lemo* connectors are fixed into a 1 cm long hollow copper cylinder, open on one side, that forms the cover of the filter (figure b) in 4.9). The SS core are soldered using the *Superior No. 23* flux and 60/40 tin-lead solder. The cables are then glued to the holders using double bubble epoxy. When the epoxy is dry, the cover is fixed to the main cylinder via a screwed-in copper rod (panel a) of 4.9). This allows the pins of the *Lemo* connectors to be completely screened from unwanted electromagnetic fields. Four of these cylinders were fabricated in total and installed at the mixing chamber, as shown in figure 4.9.

4.6.2 Characterisation

To characterise and test the filters before mounting them, a vector network analyzer (VNA) *Anritsu 37397C* was used to measure the attenuation of a single coaxial cable (1.5 m) over the frequency range from 40 MHz up to 15 GHz. Three thermal cycles were done between room temperature (300 K) and liquid nitrogen (77 K) to check for mechanical strength and repeatable behavior of the coaxial cable. The microwave cables of the VNA were calibrated beforehand over the desired frequency- and power range. Figure 4.10 shows the measured attenuation at the two different temperatures with a power input

Insertion loss [db/m]	Typical (RT)	Measured / Calculated (RT)	Measured / Calculated (LN2)
0.5 GHz	12.78	12.2 / 11.8	10.3 / 9.9
1.0 GHz	18.08	16.9 / 16.8	14.4 / 14.0
5.0 GHz	40.50	37.5 / 37.6	32.2 / 31.4
10.0 GHz	57.36	'52.9' / 53.2	'47.4' / 44.5
20.0 GHz	81.28	- / 75.2	- / 62.9

Table 4.3: Insertion loss per meter at different temperatures. The typical values are given by the company *MICRO-COAX*. RT stands for room temperature and LN2 for the liquid nitrogen temperature. Notice that noise strongly affects the measurement below -60 dB such that the last values at 20 GHz are missing.

between 0 dBm and -7 dBm. Below an attenuation of around -60 dB the signal lies within the white noise level of the VNA and it is therefore not useful to give any exact values below this point (see table 4.3). In this high attenuating range, a much shorter coaxial cable or a pre-amplifier would make it possible to extend these measurements, but there was no need to do so because the filtering only becomes more and more efficient at higher frequencies anyway [89].

It is possible to calculate the attenuation A per meter as a function of the frequency as given by [89]

$$A = 20 \cdot \Re(\gamma)/\ln(10) \tag{4.4}$$

$$\gamma = \sqrt{i\omega c \cdot (r + i\omega l)} \tag{4.5}$$

$$c = 2\pi\epsilon\epsilon_0/\ln(d_2/d_1) \tag{4.6}$$

$$l = \mu\mu_0 \ln(d_2/d_1)/2\pi \tag{4.7}$$

$$r = \sqrt{\omega} \cdot \left(\sqrt{\mu\mu_0\rho_w/2}/\pi d_1 + \sqrt{\mu\mu_0\rho_j/2}/\pi d_2 \right) \tag{4.8}$$

The total attenuation A per meter consists of the capacitive (equation (4.6)), inductive (equation (4.7)) and resistive (equation (4.8)) part per meter of the coaxial cable. Only the real part $\Re(...)$ of the propagation coefficient γ (equation (4.5)) contributes to the attenuation A. With d_1 the diameter of the inner core, d_2 the outer diameter of the PTFE insulator, ϵ and μ are the DC value of the relative dielectric and the relative magnetic

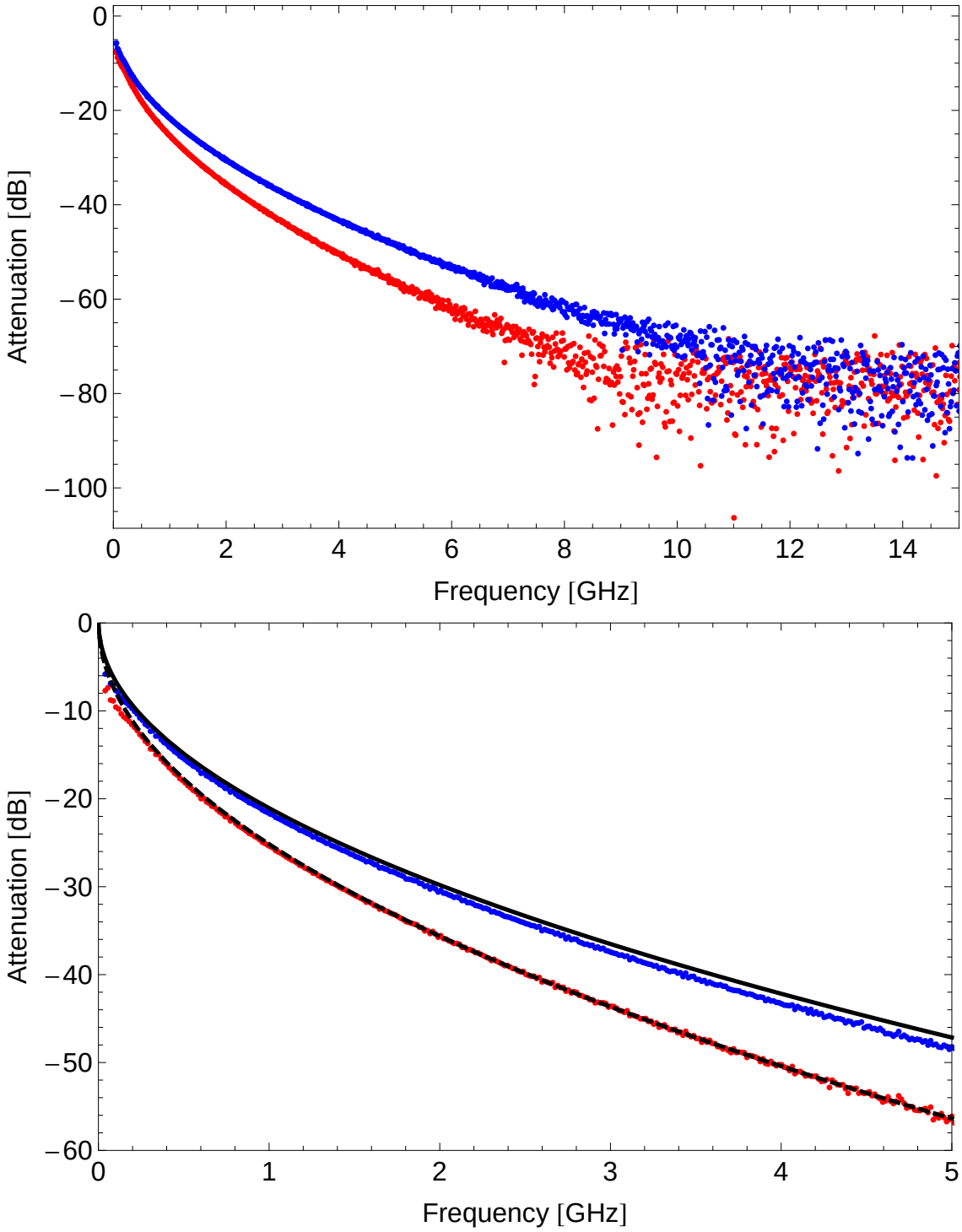

Figure 4.10: Top: Attenuation of a single micro-coax cable, *MICRO-COAX* (UT-020-SS-SS), with length 1.5 m over the frequency range from 40 MHz to 15 GHz. The red points represent a room temperature (300 K) measurement and the blue ones at liquid nitrogen temperature (77 K). Below an attenuation of around -60 dB the signal lies within the white noise level of the VNA. Bottom: Same as above but over a reduced frequency range. The theoretical prediction are given in black (solid line for 300 K and dashed for 77 K) without any adjustable parameter.

Parameter	300 K	77 K
d_1	0.114 mm	
d_2	0.381 mm	
ρ_w	$7.19 \cdot 10^{-7}\,\Omega \cdot m$	$5.03 \cdot 10^{-7}\,\Omega \cdot m$
ρ_j	$7.19 \cdot 10^{-7}\,\Omega \cdot m$	$5.03 \cdot 10^{-7}\,\Omega \cdot m$
μ_0	$1.257 \cdot 10^{-6}$ H/m	
μ	1	
ϵ_0	$8.854 \cdot 10^{-12}$ F/m	
ϵ	2.1	

Table 4.4: Table of the parameters used to calculate the theoretical attenuation as a function of frequency, figure 4.10. The temperature change is assumed to only affect the electrical resistivity of the stainless steel.

constant for the insulating material, respectively, ρ_w and ρ_j are the electrical resistivities of the core wire (w) and jacket (j), respectively. See reference [89] for further details.

The parameters at room temperature and liquid nitrogen temperature are listed in table 4.4 given by the datasheet. The only difference between the two temperatures is the electrical resistivity for the stainless steel which can be found in reference [92] for temperatures between 1 K and 1800 K. Note that, although there is no adjustable parameter for the theoretical prediction, it is still in a very good agreement with the measured values, see figure 4.10. To calculate the minimum length of the coaxial cable required to provide sufficiently strong filtering, Zorin calculated the effect of thermal noise onto the transition rate of a Josephson tunnel junction with an environmental impedance of $\Re Z_0 = 50\,\Omega \ll h/e^2$ and charging energy $E_c = 2k_BT_0$. The thermal noise is assumed to come from a warm load with temperature T_f before filtering the signal by the coaxial cable, which is itself assumed to be thermalised at T_d together with the device under test (DUT).

The results of this calculation can be summarised in a transcendental equation (4.11) which has to be solved for the parameter b (4.9), which in turn is dependent on the length

of the coaxial cable L.

$$b = 2\kappa L\sqrt{E_c/(2\hbar)} \tag{4.9}$$

$$\kappa = \lim_{\omega\to\infty}\frac{\Re\gamma(\omega)}{\sqrt{\omega}} \tag{4.10}$$

$$1 = \frac{8T_f Z_0 e^2}{2\pi b^2 T_0 \hbar}\exp(T_0/T_d - b) \tag{4.11}$$

For the following temperatures, $T_0 = T_d$ =20 mK and T_f =20 K, the transcendental equation is solved for $b \approx 2.18$ which, together with $\kappa = 20.4 \cdot 10^{-6}$, gives a minimum length of 104 cm. The length L depends logarithmically on the temperature of the noise source T_f such that for L = 1.5 m the noise from a source temperature of more than 100 K is still reliably filtered.

The effects of the low-temperature microcoaxial filters when installed can qualitatively be seen in figure 4.11. The top plot shows the current-voltage characteristics of two similar Josephson junction in the extended range of $I_b = [-300, 300]$ nA, with (blue) and without (green) the low temperature microcoaxial filters installed. Both Josephson junctions were fabricated in the same way at different times (approximately 5 months apart) and measured in a two terminal setup with a full up and down sweep of the applied current. One can clearly see the qualitative reduction of the noise in the resistive branch. The bottom plot shows an expanded view of the top plot and shows the superconducting branch for the filter I(V) curve which is absent for the unfiltered one. Furthermore, hysteresis can only be observed when the DC lines were filtered which is a strong demonstration of the reduced environmental noise on the behaviour of the junction.

4.7 Sample holder

The sample holder can be seen in front of the filters in panel c of figure 4.9). It is screwed into the mixing chamber plate by a threaded copper rod to achieve a good thermal con-

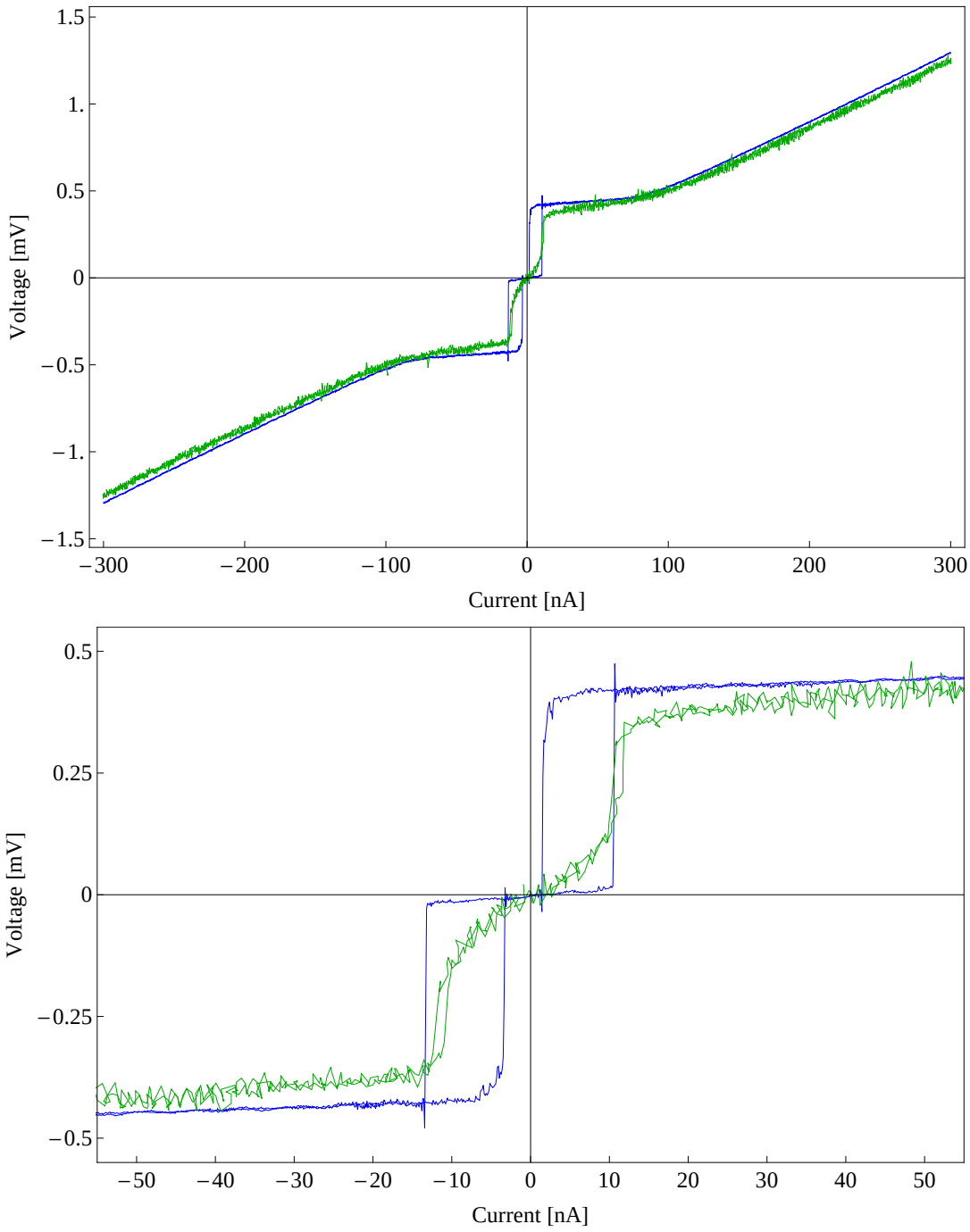

Figure 4.11: Current-voltage characteristics of two similar Josephson junctions with (blue) and without (green) the low temperature microcoaxial filters installed. Both junctions were measured in a two terminal setup. Top: I(V) characteristics in the bias current range I_b = [-300,300] nA showing the reduction of the noise in the resistive branch. Bottom: Zoom in of the top plot which shows the occurrence of the superconducting branch as well as the hysteresis after the filters were added to the DC-lines of the experimental setup. This clearly shows the qualitative improvement of the environment due to the low temperature filters.

tact. The main body of the sample holder is made of gold plated copper plates inside which a printed circuit board (PCB) contains the sample (panel d) in figure 4.9). The PCB connects the wiring of the dilution refrigerator to the sample through wire bonds ($20\,\mu$m diameter aluminium wires). An in-house ultrasound wire bonder which is located in the clean room is used for this purpose. Before wirebonding, the sample is glued onto the sample holder by GE varnish. At least 2 wire bonds were attached for each lead of the sample as there is a chance for them to break during the later cool down.

The wires of the microcoaxial filters are fed into the bottom adapter of the sample holder (see panel c) and d) in figure 4.9) by four 20 cm long niobium-titanium superconducting shielded wires. This adapter is made of copper and has the form of a hollow cylinder (with a screw-on cover) to which the 4-pin *Lemo* connectors are mounted. Short (around 10 cm), twisted copper wires then make the connection inside the sample holder to the PCB onto which they are soft soldered.

Chapter 5

Characterisation of a Josephson junction

This chapter describes the results of 2-terminal electrical measurements performed on an Al/AlOx/Al Josephson junctions with dimensions 80 nm x 5 μm = $0.4\,\mu m^2$. These junctions are considerably smaller than those explored in existing literature. The measurements consist of current-voltage characteristics (V(I)-curves) in order to extract fundamental parameters as the critical current, superconducting gap, normal state resistance and lead resistance. Based on a simple measurement of the junction resistance at room temperature, which provides an estimate of R_n ≈2.7 kΩ, the following characteristics may be expected for the junctions on which our experiments are performed (see section 2): A critical current of $I_c = 1.764\pi k_B T_c/(2eR_n)$ ≈106 nA, a capacitance close to 20 fF and a plasma frequency of around $\omega_p \approx 125$ GHz. Furthermore, the crossover temperature is expected to be T_{co} ≈95-144 mK, depending on the quality factor of the junction (expected to be Q ≈7 for at low frequencies and Q ≈1 for frequencies around ω_p). For historical reasons this junction was fabricated on a 100 nm thick SiN membrane but effect of the membrane on the measurement is not further investigated in this thesis, except perhaps where it relates to measurements related to self-heating in the junction from our measurements.

5.1 Setup for current-voltage characterisation

The measurement of a single Josephson junction was performed in a two-terminal setup in which the output of the DAQ is connected to a $1\,\mathrm{M}\Omega\pm9\,\mathrm{k}\Omega$ bias resistor at room temperature as described in chapter 4. A four-terminal measurement was originally performed but a large additional voltage noise was observed and it was not possible to determine its cause nor its suppression. The additional voltage noise did not appear on the two-terminal setup which explains its implementation. One of the leads was connected to the common ground (i.e. breakout box chassis) to avoid a floating ground. In order to use the full output range of the DAQ system for small biasing currents an additional voltage divider of a fixed factor 85.2 ± 1.5 can be inserted in front of the bias resistor as shown in figure 4.8. The maximum bias current (with a $1\,\mathrm{M}\Omega$ bias resistor) that corresponds to an output range $[-10, 10]$ V±3.23 mV of the PCI, is $[-10, 10]\,\mu\mathrm{A}\pm3.23\,\mathrm{nA}$. The bias current range, with the additional voltage divider, reduces to $[-117, 117]\,\mathrm{nA}\pm39\,\mathrm{pA}$. The applied bias current was measured using a second analog channel of the DAQ system.

The bias resistor itself creates thermal noise which affects the accuracy of the bias current. The root mean square of the *Johnson-Nyquist* current noise of the bias resistor for a bandwidth Δf =22.5 MHz (this corresponds to the -3 dB point of the cold microcoax filter from figure 4.10) is $i_n = \sqrt{4k_BT\Delta f/R_b}$ which is at room temperature ($300\,\mathrm{K}$) around $610\,\mathrm{pA}$. The bias current range and the rms-value of the Johnson-Nyquist current noise compares with the theoretical critical current $I_{c0} \approx 106$ nA.

The voltage generated by the tunnel junction above the critical current is around twice the superconducting gap $2\Delta(0)/e = 365$ μV and therefore has to be amplified. A room temperature amplifier (*Stanford Research Systems (SRS) SR640*) is used to amplify the signal with a gain of 60 dB after it is low-pass filtered at 25 kHz. The output of the amplifier is connected to the DAQ board which reads out the amplified signal. The absolute accuracy of the analog input of the DAQ system is $360\,\mu\mathrm{V}$ for the range ±1 V and the

smallest voltage change that can be detected is $12.0\,\mu V$, according to the manufacturers specification.

The DAQ system is controlled by a *LabView* VI which applies a bias current and nearly simultaneously reads out the voltage response.

5.2 Current-voltage characteristics at low temperature

In order to characterise a single Josephson junction, V(I)-curves were recorded at low temperatures. It is important to do both up and down current sweeps to examine the damping regime of the junction by looking at any hysteretic behaviour. In the presently discussed setup, the current bias sweep starts from zero and follows a saw-tooth form with amplitude $\pm I_{b,max}$. This saw-tooth form has the advantage that the starting and ending point are at zero and therefore avoids any sudden change in the bias current which might cause any form of unwanted and uncontrolled effect on the Josephson junction.

The first V(I)-curve was taken for the range I_b =[-600,600] nA with 2400 points in total (with a rate of 1 nA/ms), see figure 5.1. The data clearly shows that the junction is in the underdamped regime (i.e. $Q \ll 1$) as a hysteretic behaviour of the switching into the resistive branch is clearly visible. The V(I)-curve also shows the superconducting branch, where the voltage across the junction is nominally zero, as well as a finite voltage jump at the retrapping current that indicates the superconducting gap voltage. A linear fit (red line) for the high current part of the measurement gives a normal state resistance of $R_n = (3192 \pm 0.3)\,\Omega$ but, as a result of the 2-terminal measurement, it includes the on-chip leads and the wiring of the setup. To further extract the total resistance of the leads and wiring as well as the superconducting gap, a second V(I)-curve was taken by using an additional voltage divider in front of the bias resistor to be able to use the full output range of the voltage source in order to guarantee a good resolution. Figure 5.2 shows the measured data. The lead and wiring resistance (orange line) are extracted with

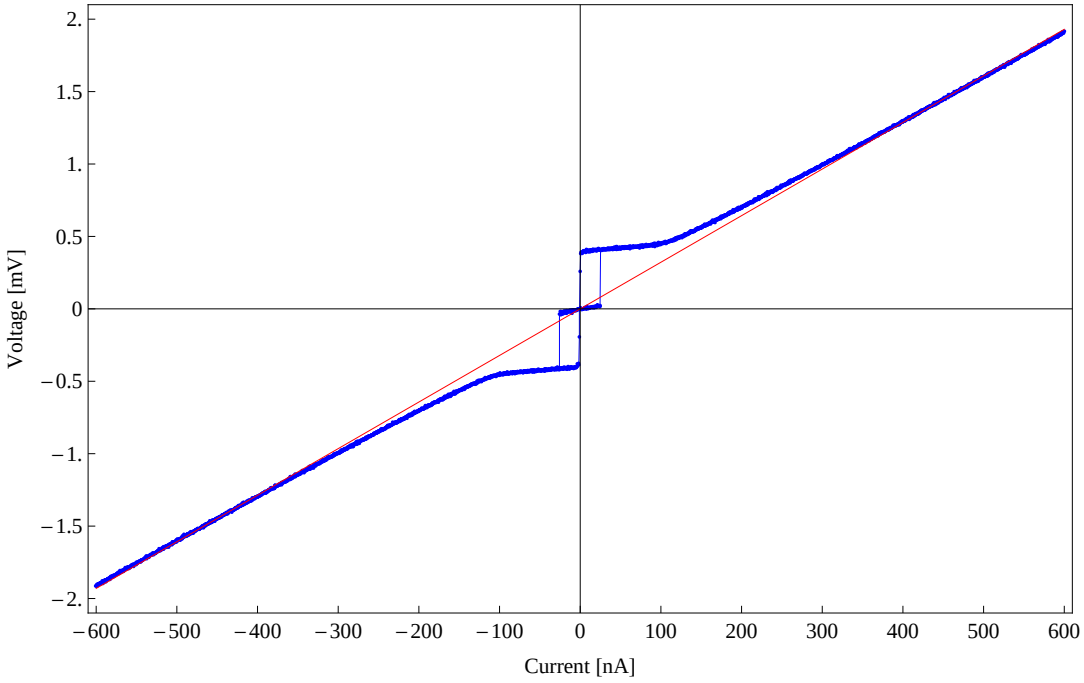

Figure 5.1: A V(I)-curve for an Al/AlOx/Al Josephson junction of dimension 80 nm x 5 µm = $0.4\,\mu m^2$ measured at 17 mK with a read-out gain of 60 dB. The red line is a linear fit of the normal state resistance $R_n = (3192 \pm 0.3)\,\Omega$. This value includes the resistance of the on-chip leads and the wiring of the setup. The plot shows up and down current sweeps in the range [-600,600] nA and clearly shows the hysteretic switching at around 30 nA which is expected for an underdamped junction (i.e. $Q \ll 1$).

a total resistance of $(630 \pm 37)\,\Omega$. This resistance compares with the expected wiring resistance of the dilution refrigerator for room temperature measurement; the resistance from the breakout box to the microcoax filter is around $2 \times 175\,\Omega$ and will not change significantly at lower temperatures due to the fact that the major part of the resistance comes from the *Manganin* wire which is an alloy. The low temperature filters have a resistance of around $2 \times 75\,\Omega$ at 77 K. This implies a total resistance close to $500\,\Omega$. The on-chip leads which are made of Au can be neglected in comparison to wiring resistance of the dilution refrigerator. There is therefore a difference of around $130\,\Omega$ between the extracted resistance of the V(I)-curve and the expected wiring resistance. Section 5.2.1 will therefore address this issue.

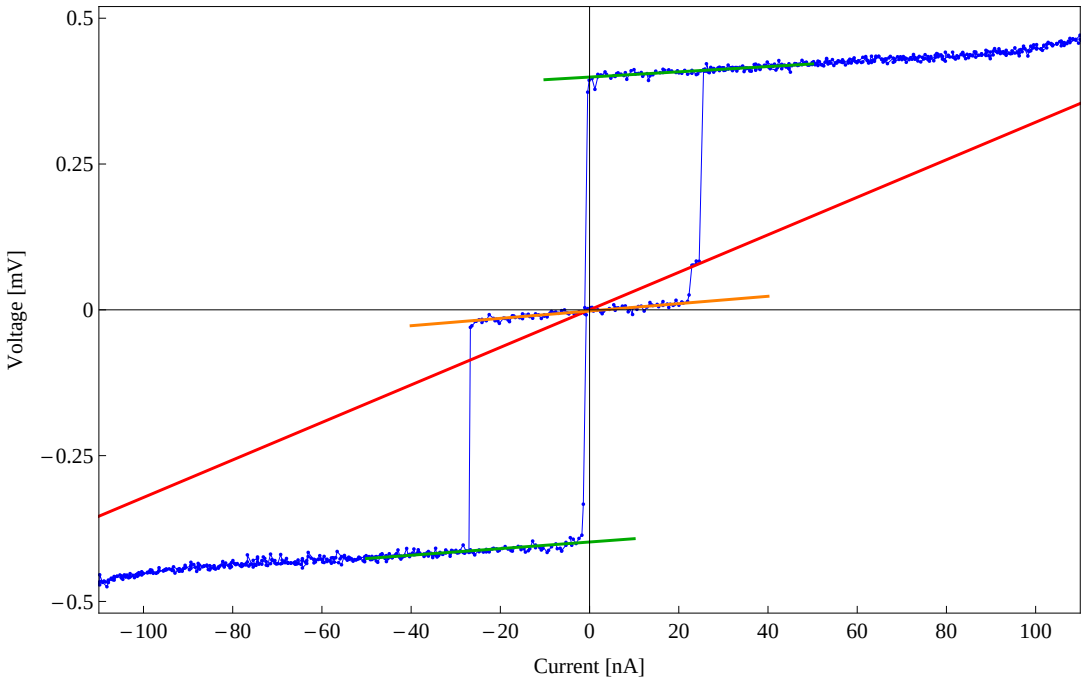

Figure 5.2: A V(I)-curve of the same underdamped Josephson junction as in figure 5.1 but in a reduced bias current range taken with a voltage divider. Red line: Linear fit with $R_n = (3192 \pm 0.3)\,\Omega$. Green lines: linear fits to extract the superconducting gap voltage V_g which is the value of the intersect with the vertical axis, $2\Delta_+/e = (399 \pm 1)\,\mu V$ and $2\Delta_-/e = (-398 \pm 1)\,\mu V$. Orange line: linear fit to determine the on-chip lead and wiring resistance which add up to $(630 \pm 37)\,\Omega$.

5.2.1 Phase diffusion

In 1989 J. M. Martinis and R. L. Kautz showed experimentally that even for underdamped Josephson junctions, classical phase diffusion can be seen as a finite resistance in the superconducting branch [58,69]. This behaviour can not be explained in the underdamped RCSJ-model because any movement of the phase particle out of the potential well would move it into the voltage state due to the low damping. The reason for phase diffusion is a frequency-dependent dissipation; the phase particle experiences a small damping in the running state but as soon as it is trapped in a metastable potential well, the particle experiences a large damping [65]. In the phase diffusion regime the particle therefore escapes and retraps continuously and thus shows a random walk down the potential wells causing a finite voltage drop. Two conditions must be satisfied to be able to observe phase diffusion in an underdamped junction, firstly a sufficient damping at high frequencies (i.e. near the Josephson frequency ω_J). This condition makes sure the junction can dissipate power by the production of current at the Josephson frequency. The second condition requires the potential well ΔW_- to not be too large with respect to the thermal energy $k_B T$ such that classical, thermal activation will occur even at very low temperatures (i.e. $T \ll T_c$) [1].

The resistance R_d caused by phase diffusion can be written as [1]

$$R_d = \frac{Z_j}{(I[0, E_J/k_B T])^2 - 1}, \tag{5.1}$$

where $I[n, z]$ is the modified Bessel function of the first kind and Z_j is the complex impedance at the plasma frequency. The resistance R_d is called *sub-gap resistance* as it can be measured in the superconducting branch of the V(I)-curve. Figure 5.3 shows the dependence of R_d/Z_j on the thermal fluctuation strength given by $E_J/k_B T$. The sub-gap resistance contributes less than 1% of Z_j to the total resistance for $E_J/k_B T \approx 3.9$. This corresponds to a critical current of $3.9\,\mathrm{nA}$ at $20\,\mathrm{mK}$ such that any higher critical cur-

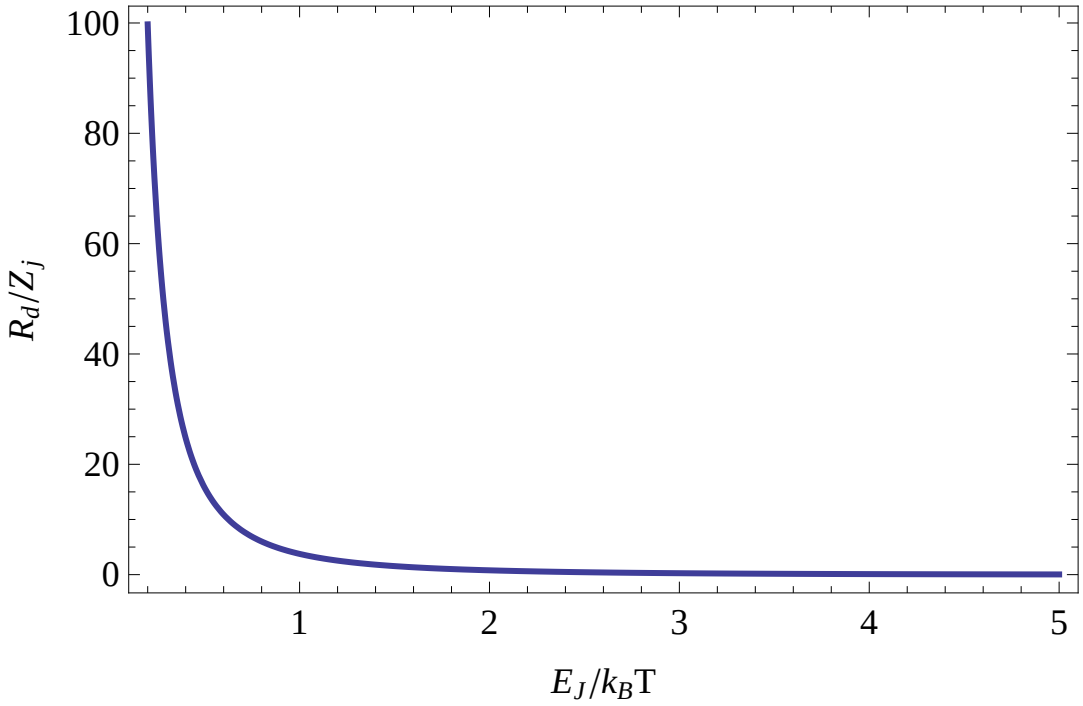

Figure 5.3: Resistance R_d caused by phase diffusion relative to the high frequency impedance Z_j on the thermal fluctuations strength E_j/k_BT.

rent would have an even smaller effect than 1% of Z_j. By assuming a high frequency impedance of around 50-100 ohm [1], the additional resistance R_d is less than $1\,\Omega$. As the critical current in figure 5.1 is much larger than $3.9\,$nA, phase diffusion is unlikely to cause the additional unknown resistance of $130\,\Omega$ in the superconducting branch of figure 5.2. Even if the sample temperature is 10 times larger (i.e. $200\,$mK) than expected, the additional resistance R_d is much smaller than $130\,\Omega$.

However, looking at a single V(I)-curve is not enough to make a reliable conclusion about the phase diffusion resistance R_d as this strongly depends on the temperature and therefore also on thermal fluctuations. In order to obtain a descriptive statistics about this random process, a set of 1000 V(I)-curves were recorded with a bias current range [-40,40] nA performed in 200 steps at a rate of 250 kSa/s. The mixing chamber temperature is 20 mK. The subgap is extracted and the resulting histograms are shown in figure 5.4 for three different cases of waiting times: 0 ms, 1 ms and 2 ms (note that the minimal available increase of the waiting time is 1 ms). There is a possibility that the bias sawtooth like cur-

rent sweep is done too fast such that the bath temperature of the junction is increasing due to the lack of time to dissipate the energy after it switched to the voltage state. The characteristic time scale of the junction for this process is $R_n C_j \ll 1$ ns (as a general rule of thumb the junction capacitance of $Al/Al_2O_3/Al$ is around 45 fF/µm^2, [70], which means in our case C_j =(18$\pm$5) fF). The leads have a capacitance to ground mainly given by the microcoax filter with a capacitance of around $1.5 \cdot 10^{-10}$ F and a wiring resistance of $250\,\Omega$ per wire which corresponds to a characteristic quasi-particle decay time of approximately 40 ns. These timescales are compared to the sampling frequency of 250 kSa/s (4μs/Sa) which is far larger and hence the junction should be relaxing to its ground state after a switching event well before the next measurement takes place. The mean of the supgab resistance $\overline{R_s}$ and standard deviation σ are given in table 5.1. The standard deviation is large relative to the mean value which itself is much larger than the expected wiring resistance of $500\,\Omega$. This indicates that the difference between the expected wiring resistance and the measured resistance in the superconducting branch (given by $\overline{R_s}$) is not intrinsic (i.e. phase diffusion) to the Josephson junction as the difference is within the standard deviation of $\overline{R_s}$. It is unclear why the resistances in the superconducting branch has such a high standard deviation but other extrinsic issues such as common mode rejection ratio effects have been considered and discarded.

Another important parameter which can be extracted from the measurement of the V(I)-curve is the critical current which will be analysed in section 5.2.2.

Waiting time	Mean value $\overline{R_s}$	Standard deviation σ
0 ms	$746\,\Omega$	$182\,\Omega$
1 ms	$730\,\Omega$	$222\,\Omega$
2 ms	$695\,\Omega$	$81\,\Omega$

Table 5.1: Mean value and standard deviation of the subgap resistance of 1000 V(I)-curves extracted from the histograms in figure 5.4.

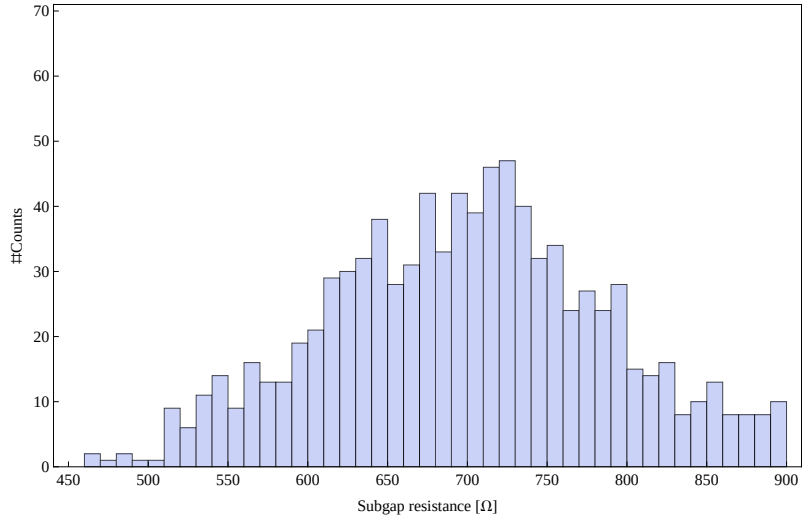

(a)

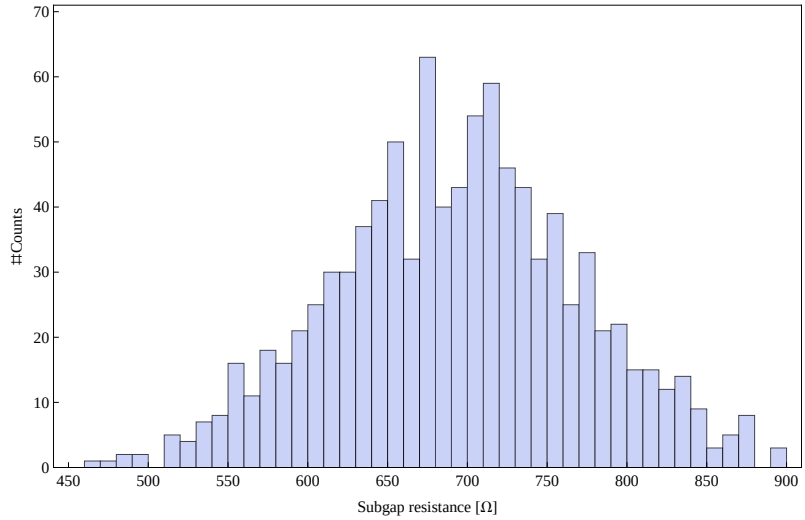

(b)

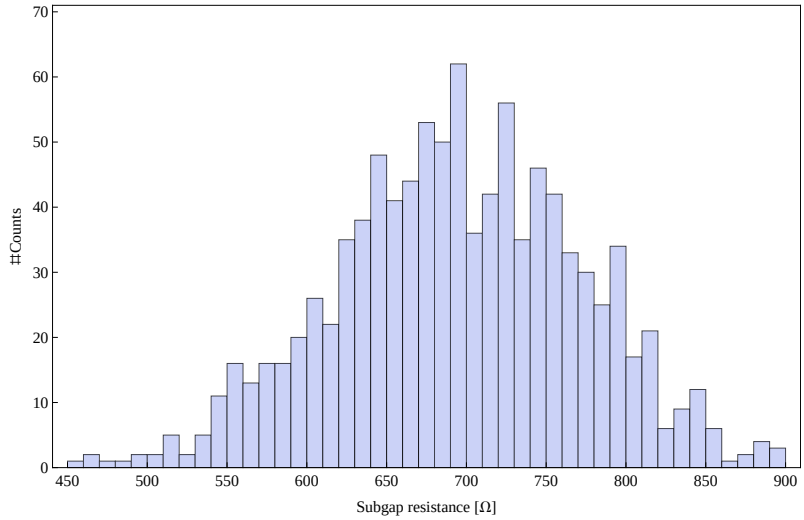

(c)

Figure 5.4: Histograms of the extracted subgap resistance of 1000 V(I)-curves. Each V(I)-curve consists of 200 measurement points within a bias current range of [-40,40] nA. In order to see if heating causes the subgap to be higher than expected, different waiting time after the 200 steps were used. a) no waiting time. b) 1 ms. c) 2 ms. The average value and its standard deviation can be found in table 5.1

5.2.2 Critical current measurement

The microscopic theory of superconductivity which was developed in 1957 by J. Bardeen, L. N. Cooper and J. R. Schrieffer (BCS theory) [6] was later (1963) applied to Josephson tunnel junctions by V. Ambegaokar and A. Baratoff [43, 44] who worked out the temperature dependence of the critical current [1]

$$R_n I_c(T) = \frac{\pi\Delta(T)}{2e} \tanh\left(\frac{\Delta(T)}{2k_B T}\right). \tag{5.2}$$

At $T = 0$, this formula reduces to $R_n I_{c0} = \pi\Delta(0)/2e = 1.764\pi k_B T_c/2eR_n$. It is important to note that I_{c0} is the critical current without any fluctuations involved, neither thermal nor macroscopic quantum tunneling. From figure 5.2 one can see that the measured critical current is around 30 nA which is more than three times smaller than expected. One possibility for this discrepancy could be the effect of quantum fluctuations in such small Josephson junctions which would cause the junction to switch into the normal-state before $I_b = I_{c0}$. This was indeed also observed by Kivioja et al. [65] and will be discussed in more detail at the end of this section. It is also possible that the electron temperature is higher than the bath temperature (17 mK) as described in section 2.1.7. In this case, thermal fluctuations would be responsible for the reduced critical current of the Josephson junction which means that the electron temperature would have to be close to the critical temperature of around $1.2\,\mathrm{K}$ as $R_n < R_q$. This scenario is unlikely even as the electron-phonon coupling is reduced in the current device by the SiN membrane between the substrate and the Josephson junction. The temperature dependency of the critical current is required for a deeper insight into the effect of the thermal fluctuations onto the critical current and this is further discussed in section 5.3. Another possibility would be a current offset circulating in the setup and therefore producing a reduced critical current. This offset current would have to be an oscillating current as the critical critical current in figure 5.2 is reduced both in the positive and in the negative bias range. In this case it

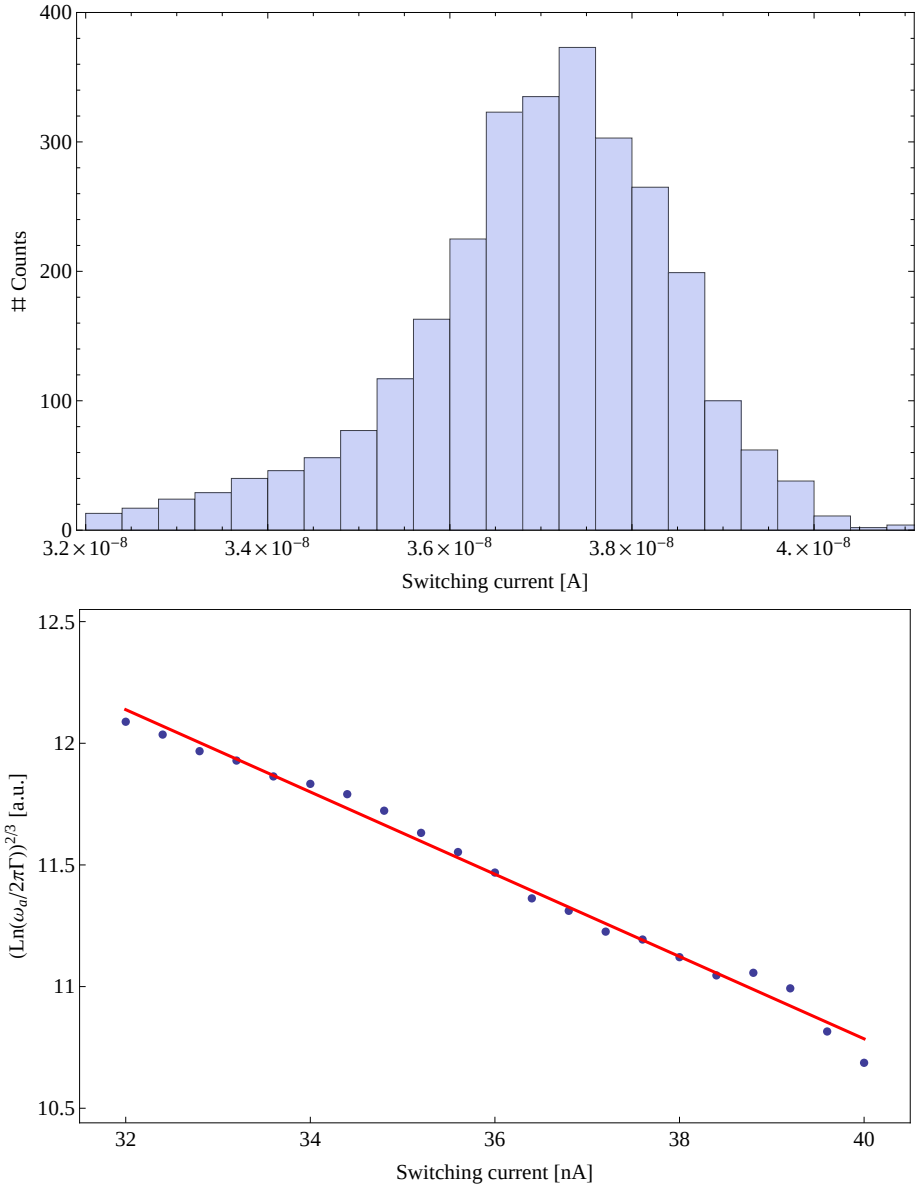

Figure 5.5: a) Histogram of the switching current distribution of 3000 recorded V(I)-curves. b) Analysis of the Histogram to extract I_{c0}, T_{esc} and C_j by comparing it to the macroscopic quantum tunneling model (MQT) by a linear regression best fit (red). The slight oscillation in the data is of unknown origin.

is useful to get descriptive statistics about the critical current distribution as the switching process from the zero voltage state into the running state is a stochastic process. The switching current was therefore extracted from 3000 V(I)-curves by finding the peak values of the curve derivatives dV/dI, the resulting histogram can be seen in the top panel of figure 5.5. In section 2.2, the switching current distribution was discussed and can now be

used to extract characteristic parameters of the measured Josephson junction. Equation (2.58) is in the form $y = b + a \cdot I_b$ and y can be calculated from the experimental data by calculating Γ using equation (2.49) and estimating the attempt frequency $\omega_a(I_b, I_0, C_J)$ using some initial values for E_J and I_{c0} (either by extracting I_{c0} from an V(I) characteristic or by a normal state resistance measurement at room temperature and then using the Ambegokar-Baratoff formula (2.3) to calculate I_{c0}). A linear fit to the data with the fluctuation model can be used to iteratively predict more precisely the values for C_J and I_{c0} by first calculating the critical current and the escape temperature from the linear fitting parameters, $I_{c0} = -b/a$ and $T_{esc} = -\hbar/(ek_B a\sqrt{b})$. These can then be compared with the theoretical prediction of T_{esc} that is used to extract C_J. By repeating those two steps several times it is possible to calculate the I_{c0} and C_J iteratively.

The above iterative procedure was applied to the measured histogram (top panel of figure 5.5), together with bias current rate of dI_b/dt=1200 nA/s. The resulting analysis can be seen in the bottom panel of figure 5.5 together with a linear fit (red line). The following fitting parameters are extracted:

$$I_{c0} = (104 \pm 3)\, nA \tag{5.3}$$

$$T_{esc} = (67 \pm 8)\, mK \tag{5.4}$$

$$C_j = (79 \pm 20)\, fF \tag{5.5}$$

The data points do show a linear dependence but they also show a slight oscillatory deviation from the fitted line, the cause of which is not understood. The extracted fluctuation free critical current I_{c0} is remarkably close to the theoretical value of a Josephson junction with R_n=2.7 kΩ, namely 106 nA. As I_{c0} is almost three times larger than the measured value in the V(I) characteristic, it would mean that the measured junction was strongly affected by quantum fluctuations.

The escape temperature of the linear fit is 67 ± 8 mK which is above the bath temper-

ature of 17 mK and could be caused by a weak electron-phonon-coupling [93] between the junction and the substrate. It is difficult to quantify this effect as the input power from the source affects the electron temperature, whereas the electrons are coupled via the SiN membrane to the substrate over several interfaces. A full calculation would also have to include the dissipation of the electrons via photons [94]. By describing an overall electron-phonon-coupling (neglecting dissipation via photons) one can roughly calculate the electron temperature via $T_{el} = (P/\Sigma V + T_{bath}^5)^{1/5}$ which was derived by Wellstood et al. [93] for thin AuCo films at millikelvin temperatures. In this formula, P is the input power, V is the volume in which dissipation takes place and $\Sigma = (2.4 \pm 0.6)$ W/mm^3/K^5 is a material dependent parameter given for AuCo. The volume of dissipation V in our case is the overlap volume of the Josephson junction plus the volume of the leads which are on top of the SiN membrane, i.e. $V \approx 25\,\mu\text{m}^3$, the input power is given by the voltage bias as $P = 0.75 V_g I_c \approx 19$ pW where the factor 0.75 corresponds to the approximate fraction of the total measurement time in which the junction was in the resistive state. By applying our parameters with $T_{bath} = 17$ mK and assuming Σ is identical for aluminium, an electron temperature of $T_e \approx 197$ mK would be the result. Such a high electron temperature is unlikely to be measured but as already mentioned, this is only a rough calculation which does not account for the used materials in detail nor does it include dissipation via photons. But it shows that heat load is clearly something that needs to be worried about and controlled in such small devices. Ultimately, the temperature dependency of the V(I) characteristic is required for a deeper insight into the possible scenario of a decoupling between the electron temperature and the bath, this is done in section 5.3.

The fitted capacitance of the junction is significantly larger than expected (estimated C_j from the designed dimensions of the junction is around $18\,fF$). Although the standard error of the fitted C_j is relatively large, a linear curve with the same fitting parameters as above but with C_j=18 fF did not fit the data at all. It might therefore be that the capacitance of the junction was underestimated. This can be caused by a smaller than expected

dimensions of the junction or the dielectric constant differs from reference [70]. It is also possible that an additional capacitance to ground was neglected which would increase the effective capacitance. A possible candidate for an additional capacitance are the RF filters which have a capacitance of 95.1 pF/m but this would exceed the total capacitance by far. A common way to explain why the capacitance of the RF filters cannot be included in the effective junction capacitance is given by the P(E)-theory (see section 2.1.6). P(E) describes the probability that the environment (with a general impedance $Z(\omega)$) can absorb energy as soon as the Cooper pair tunneled through the junction. This probability restricts the frequency ω of the electromagnetic radiation to interact with the tunnel junction. The frequency also specifies the length scale of the interaction which "increases with decreasing frequency so that the lower the [applied] voltage and the temperature the further away is the horizon which the junction sees" ([47], chapter on *Time of tunneling*). The typical wavelength of electromagnetic radiation in free space with a frequency of $\omega_p \approx 100$ GHz corresponds to less than 1 mm. This means that the additional capacitance to ground has to be on the chip rather than in the RF filters which are much further away. Another possible candidate for an additional capacitance is the SiN membrane with a thickness of around 100 nm. It is hard to quantify an additional capacitance of the SiN membrane.

It is useful to compare these results with the available data in the literature. For large Josephson junctions, the macroscopic quantum tunneling regime and the thermal activated regime are well understood and are in agreement with the theory, as for example shown by Wallraff et al. [56]. In this paper, they extracted the junction's capacitance by a cumulative switching probability measurement and compared the value with an independent spectroscopic measurement of the energy level structure of the same sample which was in good agreement. In the macroscopic quantum tunneling limit, the extracted 50% switching probability bias current was around $322\,\mu$A which is only slighly less than $I_{c0} = 325\,\mu$A of their $Nb/AlO_x/Nb$ junctions.

For small area junctions, Kivioja et al. [65] estimated the junction's capacitance by the

size of the overlap area and it was not tested separately. Their critical current was expected to be $I_{c0} \approx 239\,\text{nA}$ but a 50% switching probability was measured (at $T = 38\,\text{mK}$, i.e. MQT-regime) at around $150\,\text{nA}$ which is significanly lower. This means that the effect of quantum fluctuations is relatively large in small underdamped junctions. Maybe this explains our discrepancy between the extracted critical current from the V(I) characteristic and the theoretical I_{c0}, given by the Ambegaokar-Baratoff formula (2.3). It is well known that quantum fluctuations have a larger effect in small Josephson junctions than in large ones. This can be seen by looking at the escape rate in the MQT-regime as given in equation (2.52) in which $\Gamma_q \propto \exp\left(-\sqrt{I_{c0}C_j}\right)$ (the prefactor was neglected as Γ_q is dominated by the exponential function). Quantum effects therefore affect the junction more if $\sqrt{I_{c0}C_j}$ is small which is typical for small area junctions.

Conclusion

To conclude this section, the measured 2-terminal V(I)-curves at low temperature (17 mK) allowed us to determine that the Josephson junction is in the underdamped regime. Performing a detailed analysis on the subgap resistance showed a discrepancy between the measured and the expected value. The measured subgap resistance in the superconducting branch of 1000 V(I)-curves showed a high standard deviation the reason for which is unclear. But neither phase diffusion nor an additional heating due to the current bias was able to explain the discrepancy.

The measured critical current of the V(I)-curve is around a factor 3 lower than the predicted by the Ambegaokar-Baratoff relation. An observation that might be explained by quantum fluctuations. This was investigated by measuring a switching current histogram of the junction and comparing it to the theoretical model which includes quantum fluctuations. The fitting parameter to this model was compatible with an I_{c0} value obtained from the Ambegaokar-Baratoff relation. A comparison with literature showed that small junctions are expected to fit with theory in the MQT-regime but are indeed more affected

by quantum fluctuations in comparison with large area Josephson junctions such that it is possible to measure a significantly lower critical current in the V(I) characteristic.

The extracted escape temperature (67$\pm$8 mK) is larger than the bath temperature (17 mK). It was not possible to exclude a decoupling between the electrons and phonons which could even be emphasized by the SiN membrane. Ultimately, the temperature dependency of the V(I) characteristic is required for a deeper insight into the possible scenario of a decoupling between the electron temperature and the bath. The switching current histogram also allowed to extract the junction's capacitance which is difficult to predict just by the dimensions of the junction (as the dielectric constant might vary from the literatures value). The capacitance is relatively large compared to the expected value but it was shown that additional capacitances to ground of the setup might increase the effective capacitance of the junction.

To further understand the analysis of the Josephson junction, it is necessary to extract the superconducting gap as well as the retrapping current in a next step. Investigating the temperature dependency of the V(I)-curve allows the comparison to the Ambegaokar-Baratoff relation and furthermore shows the effect of thermal fluctuations on the critical current and the possibility of electron-phonon decoupling as we shall see in the next section 5.3.

5.3 Temperature dependence of the V(I)-curve

Several quantities in the V(I)-curve are temperature dependent, including the superconducting energy-gap Δ, the critical current I_{c0}, the retrapping current I_r (in the case of underdamped Josephson junctions) and also the subgap resistance (in the quasi particle model). In this section the temperature dependence of the current-voltage curves are recorded and analysed.

At a starting temperature of 25 mK, we switched the He-3 pumping system off. Within a

few seconds, a rapid increase of the temperature can be observed up to 300 mK followed by a slower increase afterwards, see figure 5.6. Every 15 seconds, the mixing chamber thermometer was read out while a V(I)-curve was taken every 2 minutes, or steps in temperature of approximately $2\,\mathrm{mK}$. Within the acquisition time of each V(I)-curve, the mixing chamber temperature change was less than $50\,\mu\mathrm{K}$. The bias current was swept in the range I_b=[-300,300] nA with a total of 2400 points for the up and down sweep. Figure 5.7 shows the V(I)-curves for ten different representative mixing chamber temperatures. At low temperatures, the V(I)-characteristics are hysteretic but this effect disappears at higher temperatures. The V(I)-curves in the temperature range [20,300] mK were investigated with a more careful control of the temperature (heating up the mixing chamber while circulating the mixture) but no significant change in the shape of the V(I)-characteristics could be observed. This observation indicates a thermal disconnection between the electron temperature and the bath temperature as the crossover temperature is expected to be within T_{co} ≈95-144 mK.

5.3.1 Superconducting energy-gap $\Delta(T)$

The superconducting energy-gap $\Delta(T)$ depends strongly on the temperature. The theoretical dependency can be computed numerically from the BCS model [1]

$$\ln\left(\frac{1.13\hbar\omega_c}{k_B T_c}\right) = \int_0^{\hbar\omega_c} \frac{\tanh\left(\sqrt{\epsilon^2+\Delta^2}/(2k_BT)\right)}{\sqrt{\epsilon^2+\Delta^2}} d\epsilon. \tag{5.6}$$

The cut-off frequency ω_c is chosen to be the Debye-frequency at room temperature (T_{rt}) and given by $\omega_c = T_{rt}k_B/\hbar$. The numerical solution for aluminium is shown as the red curve in figure 5.8. In the limit $T \to 0$ K the theoretical value of the superconducting gap becomes constant [1] $\Delta(0) = 1.764 k_B T_c$ and near T_c it approximates to $\Delta(T \approx T_c) \approx 1.74\sqrt{1-T/T_c}$.

The numerical solution of equation (5.6) can be approximated by a simpler analytical

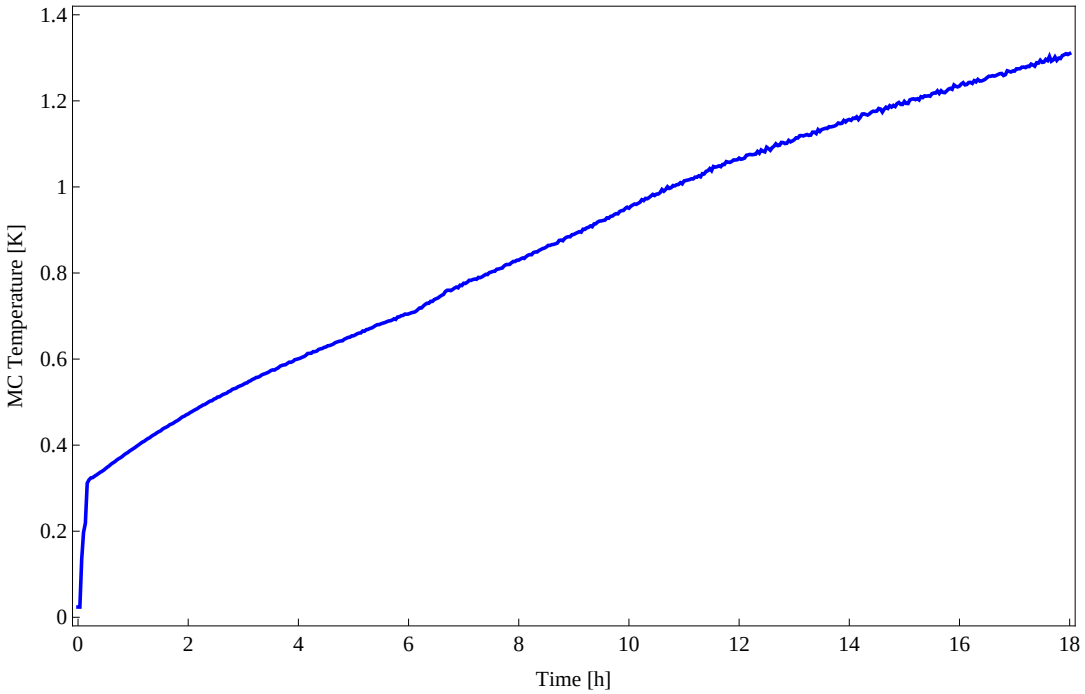

Figure 5.6: Temperature as a function of time recorded every 15 seconds after switching off the circulation pumps. The mixing chamber temperature subsequently rose quickly to about 300 mK and thereafter the temperature rate of change was about 1 mK min^{-1}.

model [95] which makes it possible to directly fit the experimental data and to extract the critical temperature T_c.

$$\Delta(T) \quad = \quad 1.764 k_B T_c \tanh\left(\frac{\pi}{1.764} \cdot \sqrt{\frac{T_c}{T} - 1}\right). \tag{5.7}$$

This analytical expression is a good approximation of the temperature dependent superconducting gap (by numerically solving equation (5.6)) as can be seen in figure 5.8 by the blue dashed curve.

The superconducting voltage gap V_g in figure 5.2 was extracted by fitting a linear regression (green lines) in the bias current range $[\pm 100, \pm 60]$ nA and then extrapolated to find the intersect with the voltage axis. This value corresponds to $2\Delta_{\pm}/e$. At the base temperature of 17 mK, the reduced positive superconducting energy-gap is $2\Delta_{+}/e = (399 \pm 1)$ µV and $2\Delta_{-}/e = (-398 \pm 1)$ µV in the negative voltage range. The theoretical value for a Al/AlOx/Al junctions at T=0 K, given by $2\Delta(0)/e = 3.528 \cdot k_B \cdot T_c/e = 365$ µV

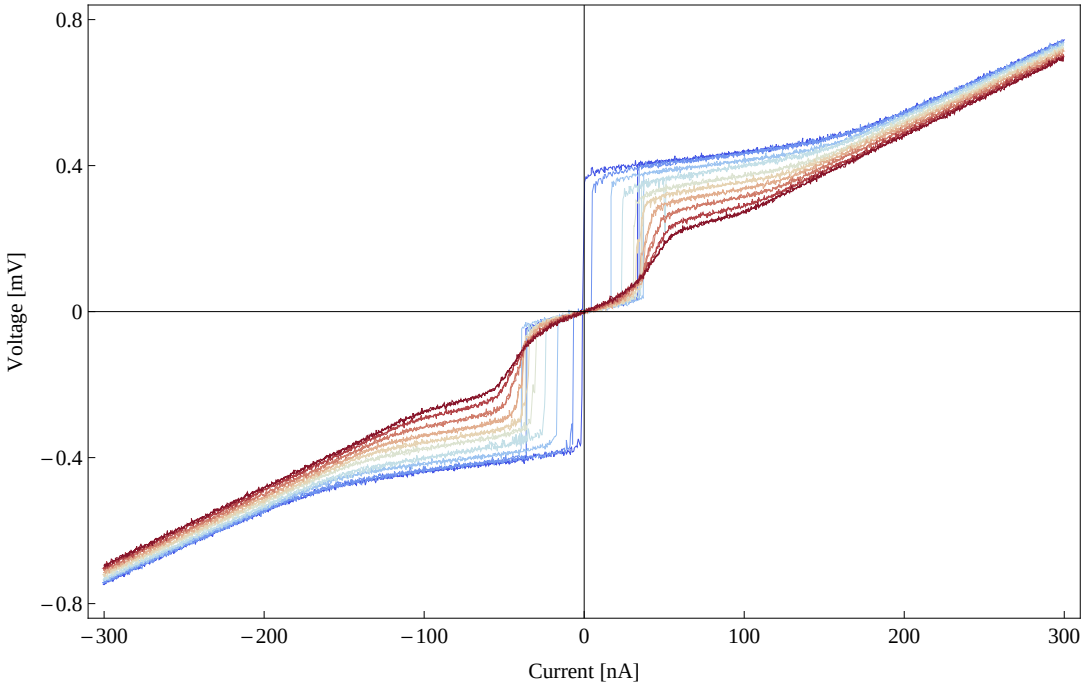

Figure 5.7: Current-voltage characteristics at different temperatures. The measured points are connected for better visibility. The colors of the lines are blue for low temperatures and red for higher ones: 25, 700, 900, 1000, 1100, 1150, 1200, 1250, 1300, 1334 mK. Notice that curves at low temperatures show a hysteretic behaviour while those at higher temperatures do not. The voltage gain of the amplifier was set to 60 dB.

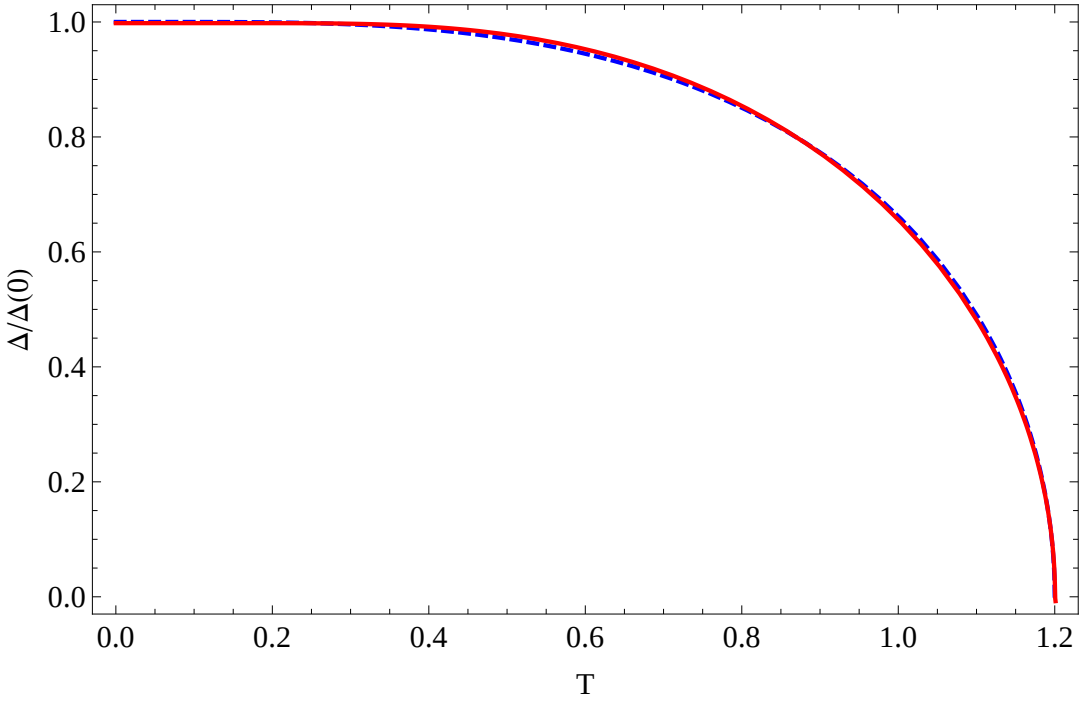

Figure 5.8: Mixing chamber temperature dependence of the normalised superconducting gap of aluminium. The red curve shows the numerical integration of equation (5.6) which is well fitted by the analytical model [95] shown by the blue, dashed curve given by equation (5.7).

is smaller than the value extracted from the measured data. The discrepancy can be explained by the dependence of T_c on the thickness of the aluminium film as discussed in reference [96]. The authors observed a relative increase of the critical temperature which is inversely proportional to the film thickness in the range of 4 nm up to 200 nm. The aluminium film thickness on this sample is around 20-25 nm which would raise T_c to around 1.30 ± 0.03 K. The measured superconducting energy-gap at the base temperature indicates a critical temperature of 1.31 ± 0.01 K and therefore lies within the expected value for the fabricated thin aluminium film. The theoretical superconducting gap at $T = 0$ is therefore $2\Delta(0)/e = 395\,\mu$V and in good agreement with the extracted value. Note that the theoretical value of I_{c0} given at the beginning of this chapter increases therefore to $I_{c0} = 115$ nA and also the cross-over temperature increases to T_{co} =99-150 mK.

The temperature dependence of the superconducting gap can now be analysed in the same way as a function of temperature and then fitted by the theoretical model of $\Delta(T)$ as given

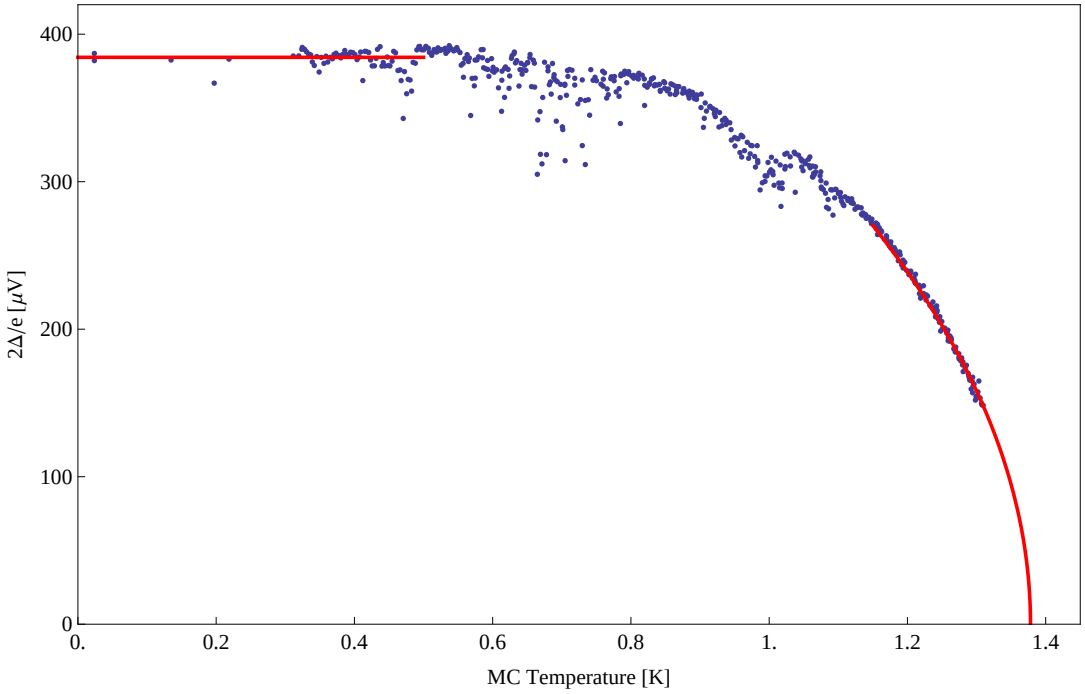

Figure 5.9: Superconducting gap Δ as a function of the mixing chamber temperature. The two red curves are fits to the theoretical limits $T = 0$ and $T \approx T_c$. The following parameters were extracted by the fits: $2\Delta(0)/e = 384 \pm 5$ µV and $T_c = 1.38 \pm 0.01$ K.

by equation (5.7).

Figure 5.9 shows the averaged superconducting gap $\Delta = (|\Delta_+| + |\Delta_-|)/2$ as a function of the mixing chamber temperature. The maximum deviation from the averaged value of Δ was $2\,\%$. Before discussing the given scatter of the extracted values of the superconducting gap, it is useful to first extract $\Delta(0)$ and T_c. The two red curves in figure 5.9 show fits of the data to equation (5.6) in the limit $T \to 0$ K resp. T_c. This results in an estimate of $2\Delta(0)/e = 384 \pm 5$ µV (for the values within the temperature range of 0 K to 0.4 K). The superconducting gap is slightly lower than the extracted value of a single V(I)-curve at 17 mK (398 ± 2 µV). The discrepancy can be accounted for the higher temperatures from 17 mK to 400 mK (the superconducting energy gap for aluminium at 400 mK is around $1\,\%$ smaller than the value at 0 K). Furthermore, the fast temperature change up to 400 mK (see figure 5.6) might cause a difference between the sample temperature and the value indicated by the mixing chamber thermometer.

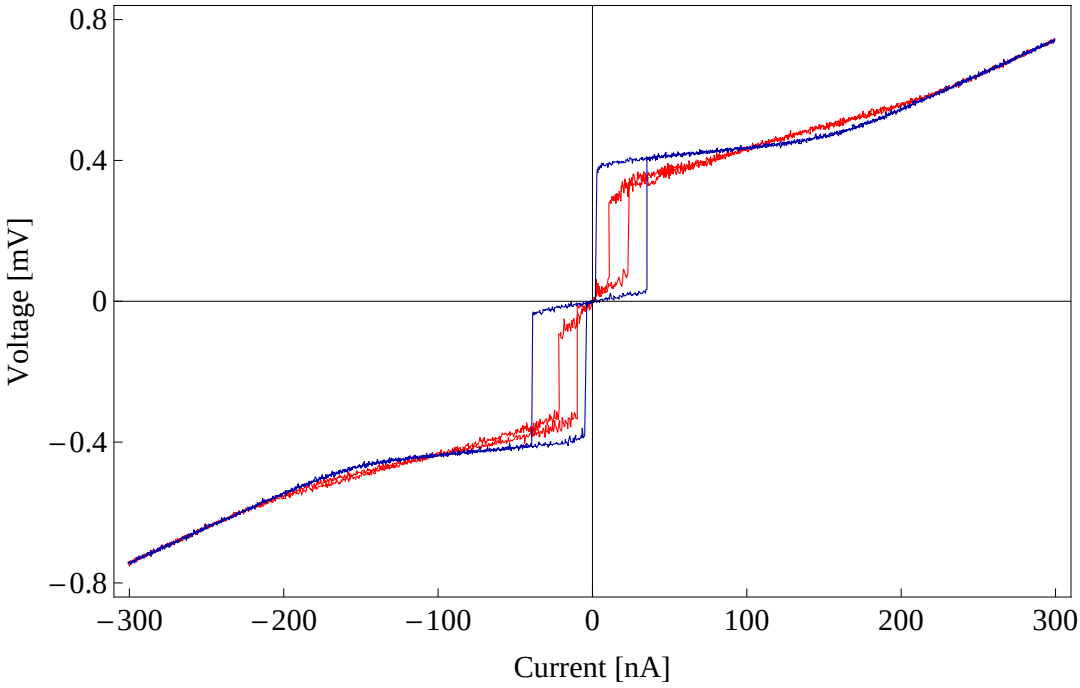

Figure 5.10: An example of a V(I)-curve which was strongly affected by noise (red) at T=705 mK in comparison to a typical curve (blue) measured at T=537 mK.

In the opposite limit, i.e. $T \rightarrow T_c$, the critical temperature can be extracted to $T_c = 1.38 \pm 0.01$ K which is slightly higher than the extracted value of the single V(I)-curve at 17 mK (1.31 ± 0.01 K). As T_c was extracted from a single V(I)-curve at 17 mK whereas the temperature dependent data, within the range of 1.15-1.3 K, consist of 75 points, the higher value of $T_c = 1.38 \pm 0.01$ K is more reliable. However, the temperature is measured at the mixing chamber stage and has its highest sensitivity in the sub 500 mK range and might be less precise at higher values. Particularly within the temperature range of 600 mK to 800 mK, the extracted values have a significant scatter. By looking at the V(I)-curves in this range (shown for two distinct curves in figure 5.10) it becomes obvious that the subgap resistance is also surprisingly high.

The slope of the linear fit which was used to extract Δ should linearly depend on the subgap resistance as both are expected to be affected in the same way by the additional quasi-particles creation at higher temperatures. In order to investigate this further, panel (a) in figure 5.11 shows this dependency. The white area in panel (a) shows the points

conforming to the expected linear relationship between the slope of the voltage state (i.e. the green lines in figure 5.2) and the subgap resistance (i.e. the orange line in figure 5.2). Those data points falling into the area shaded grey show an abnormally high subgap resistance.

A similar behaviour can be found at around 1 K. An insight into this temperature range can be obtained by looking at the coefficient of determination (R^2) of the linear fit which was used to extract Δ. For each measured resistance y_i, the linearly fitted value $\hat{y}_i$ and the average value ($\overline{y} \equiv \sum_{i=1}^{N} y_i/N$) are used to calculate R^2

$$R^2 = 1 - \frac{\sum_{i=1}^{n} (y_i - \hat{y}_i)^2}{\sum_{i=1}^{n} (y_i - \overline{y})^2}. \tag{5.8}$$

This was calculated for the positive and negative superconducting gap such that $R^2(\Delta) = (R^2(\Delta_-) + R^2(\Delta_+))/2$ and the result can be seen in panel (b) of figure 5.11. An overall decrease of R^2 is expected as the temperature increases which indicates an increase in thermal noise and such that the data points are more scattered. But near 1 K the R^2 value changes abnormally and clearly indicates an additional random noise source independent of the thermal noise. By filtering out points in the grey area (visually defined) in panel (a) and (b) of figure 5.11, a less randomly distributed dependency of $\Delta(T)$ can be found as shown in panel (c). The green curve is a fit (equation (5.7)) to the filtered data points with a critical temperature of $T_c = 1.37 \pm 0.1$ K which is within the error of the extracted T_c of the unfiltered data (figure 5.9). Although the extracted critical current is slightly larger than the theoretically expected value of 1.30 ± 0.03 K, it shows that the thin layer of the Al film increases T_c. Panel (c) of figure 5.11 furthermore shows that the temperature dependency of the superconducting gap follows the expected theoretical prediction also for small underdamped Josephson junctions. It is not clear what exactly is causing the scattering of data points in panel (a) and (b) of figure 5.11 but thermal noise is unlikely to be

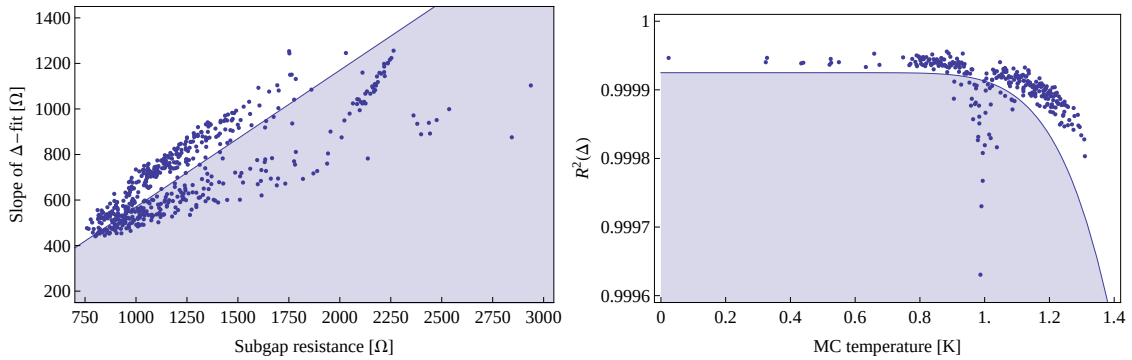

(a)

(b)

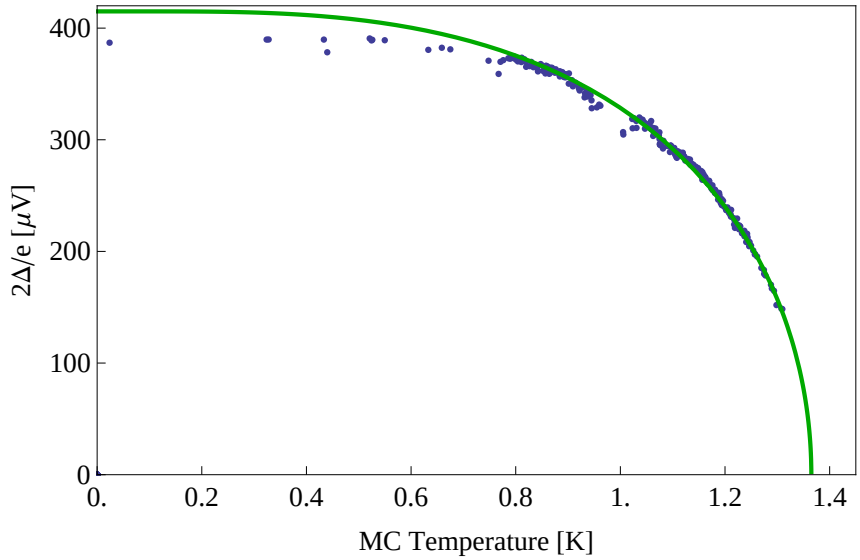

(c)

Figure 5.11: a) Slope of the linear regression to extract the superconducting gap as a function of the subgap resistance. The dots within the grey area show an abnormally high subgap resistance. b) The coefficient of determination (R^2) for the extrapolation of $\Delta(T)$ shows the spread near 1 K (grey area), indicating a random deviation of the measured resistances from the expected linear behaviour. c) Filtering out the corresponding data points (grey areas in panel (a) and (b)) from figure 5.9 shows a clearer dependency of the superconducting energy-gap as a function of the temperature. The green curve is fitted to the analytical model given by equation (5.7) with $Tc = 1.37 \pm 0.01$ K.

causing it as even V(I) curves at higher temperature show a smaller scattering. This is also supported by the fact that the mixing chamber temperature as a function of time (given in figure 5.6) does not show any unusual scattering around the relevant temperatures (around 1 K and within 600-800 mK). Given that the temperature dependence was only measured once, it is not possible to relate the scattering of data points to certain temperature ranges. Chapter 6 presents a new technique to investigate the spectrum of such unknown noise sources.

5.3.2 Investigation of the Ambegaokar-Baratoff relation

The Ambegaokar-Baratoff relation, as given in equation (5.2), can be used to calculate the fluctuation free critical current I_{c0} to then compare it to the extracted critical currents of the measured V(I) curves.

The values of the measured superconducting gap (as given in figure 5.9) is inserted into the right hand side of the Ambegaokar-Baratoff equation (5.2) and divided by the measured temperature independent value of R_n. The blue circles in figure 5.12 show the $I_{c0} = \frac{\pi\Delta(T)}{2eR_n}\tanh\left(\frac{\Delta(T)}{2k_BT}\right)$. The fluctuation free critical current calculated via the Ambegaokar-Baratoff relation reaches a maximum of around $120\,\mathrm{nA}$ in the low temperature range which is in agreement of the theoretical value of $115\,\mathrm{nA}$ (assuming a $T_c = 1.3\,\mathrm{K}$). The scattering of the data points were already discussed in section 5.3.1. The red circles in figure 5.12 show the directly extracted critical currents from the measured V(I)-curves. It is not surprising that these values are far smaller than the fluctuation free critical currents (blue circles) as quantum fluctuation are likely to cause a lower measured critical current as discussed in 5.2.2. Surprisingly, the measured critical currents seem to be independent of the mixing chamber temperature over the full range and only approaches the fluctuation free critical current at around $T = 1.2\,\mathrm{K}$. Unfortunately it was not possible to extract the critical currents from the V(I)-curves at higher temperatures due to the absence of a clear switching from the superconducting state into the voltage state.

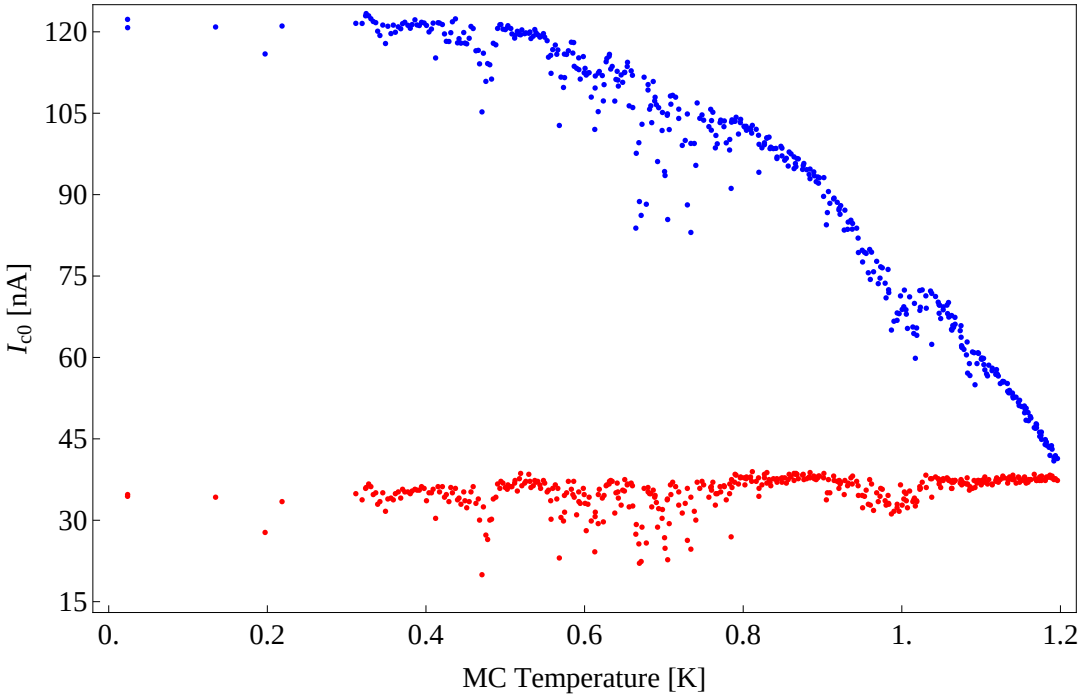

Figure 5.12: Investigation of the Ambegaokar-Baratoff relation of the measured data. Blue circles: The product $\frac{\pi\Delta(T)}{2eR_n}\tanh\left(\frac{\Delta(T)}{2k_BT}\right)$ calculated from the measured superconducting gap. Red circles: The directly extracted critical currents from each V(I)-curve which are almost constant over the whole temperature range.

Although thermal effects are expected to be the dominant type of fluctuations above the cross-over temperature T_{co} ≈95-144 mK, their effect on the temperature dependent critical current were absent. It is possible that this effect is caused by an underdamped phase diffusion as observed by Kivioja et al. [65] and discussed in section 2.4. In their paper they observed a reduction of the critical current by a factor 3, similar to our observation. Under the assumption of $C_j = 20\,\text{fF}$ and $I_{c0} = 115\,\text{nA}$ a resistance of $R(\omega_p) \approx 1.5\,\text{k}\Omega$ would be needed to reach the same reduction of the critical current. This is a rather high resistance at frequencies around ω_p as usually values around 300-500 Ω are realistic. The observation of the reduced critical current could therefore be explained by large quantum fluctuations at low temperatures and by underdamped phase diffusion at higher temperatures such that an overall reduction and temperature independence would result.

Another, not intrinsic effect, would be an AC noise source that affects the read-out of the

voltage response of the junction. This additional low-frequency noise could be responsible for the measured reduced critical current as the applied current is increased by the noise signal. Due to the fact that the critical current is in the $100\,\mathrm{nA}$ range for such small Josephson junctions, the effect of noise could be significant and even be responsible for the temperature independence of the measured critical current. Chapter 6 will show the implementation of a new technique to detect the spectrum of such a possible noise source.

5.3.3 Retrapping current

An effect which is unique to underdamped Josephson junctions is the retrapping from the running state into the zero voltage state during the sweep to zero bias current as described in section 2.1.5. If damping is completely absent the phase-particle only retraps when the bias current is back at zero. In the high damping regime the junction would already retrap at the critical current. Therefore the retrapping current I_{r0} must depend on the damping [1]. In contrast to the critical current that depends logarithmically on the damping as can be seen from equation (2.58), the retrapping current depends linearly on it [45]. On the other hand, I_{r0} also depends on the temperature and the simplest model to take this parameter into account is to assume an effective temperature dependent dissipation or damping characterised as a resistance $R^*(T)$ such that [45, 97]

$$I_{r0}(T) = \frac{4I_{c0}}{\pi\omega_p C_j R^*(T)}, \tag{5.9}$$

$$R^*(T) = R_n \exp\left(\Delta/k_B T\right). \tag{5.10}$$

Other models use a more complicated form of R^* and may even take a frequency dependence into account [45] as the damping at a few GHz is completely different from that at low frequencies. Figure 5.13 shows the averaged retrapping points (i.e. $I_{ro} = (I_{r+} - I_{r-})/2$) from the measured V(I)-curves on a logarithmic scale. The red curve is a fit to the data using equation (5.9). The following are used: $C_j = 20\,\mathrm{fF}$, $I_{c0} = 115\,\mathrm{nA}$

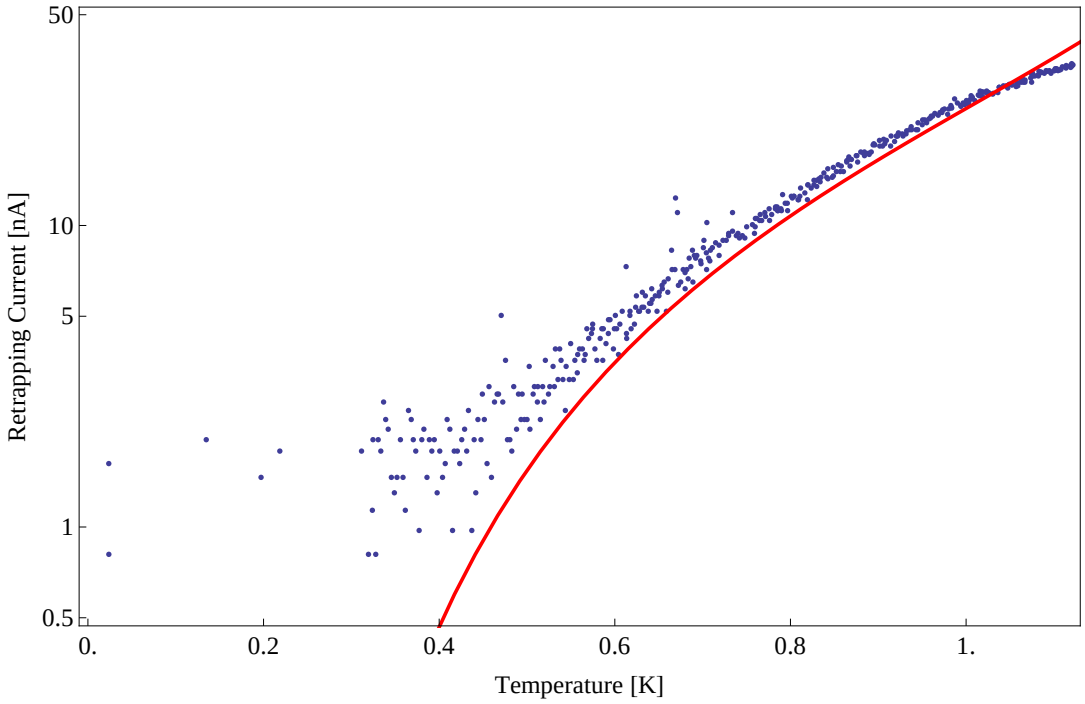

Figure 5.13: Averaged retrapping current as a function of the mixing chamber temperature. Red curve: Theoretical fit given by equation (5.9). The fitting parameter is $R_n = 405 \pm 15\,\Omega$ by using the following values $T_c = 1.3\,\mathrm{K}$, $I_{c0} = 115\,\mathrm{nA}$, $C_j = 20\,\mathrm{fF}$.

and $T_c = 1.3\,\mathrm{K}$. The analytical expression for $\Delta(T)$ is given by equation (5.7). The only fitting parameter of equation (5.10) is $R_n = 405 \pm 15\,\Omega$ which is far lower than the measured value of around $2.5\,\mathrm{k}\Omega$ but is in good agreement with the expected impedance at the plasma frequency [1, 65].

At low temperatures the measured retrapping currents are scattered which can be explained by the resolution of 1 nA. Furthermore, the low temperature values of I_r seem to bottom out at a constant value given by equation (2.31). Inserting the parameters from figure 5.13 into equation (2.31) would give $I_{r0} = 71\,\mathrm{pA}$ which is lower than the resolution of the setup such that it is not possible to make a conclusion about I_{r0} for the given data. The fit in figure 5.13 seems to predict the right behaviour under the assumption of realistic parameters.

As seen in section 5.3.2, a high frequency resistance of around $1.5\,\mathrm{k}\Omega$ would be needed to explain the reduction of the critical current by a factor 3 due to underdamped phase

diffusion. This value is around 4 times lower than the extracted value from the data in figure 5.13 and it would indicate that the effect of underdamped phase diffusion is smaller than expected.

5.4 Summary

In this chapter an advanced analysis of current-voltage characteristics of a small Josephson junction was presented. The measurement setup and the data acquisition were described. The temperature dependence of the superconducting gap $\Delta(T)$ was extracted from V(I)-curves discussed. Comparing $\Delta(T)$ to the theoretical model showed that the critical temperature is around $T_c = 1.3\,\mathrm{K}$ and therefore larger than the bulk value of aluminium. A literature review showed that this increase can be explained by the small thickness of the aluminium film which builds the Josephson junction. A large number of V(I)-curves in the temperature range 600-800 mK and also around 1 K showed a significant amount of additional noise and also showed an unusual high subgap resistance. It was not possible to make a conclusion of the cause as only one set of temperature dependent V(I)-curves were taken. But as a high standard deviation of subgab resistance was also found in section 5.2 at low temperatures it is unlikely to be caused by thermal fluctuations.

In section 5.2.2, the escape temperature was extracted from the cumulative escape probability measurement and gave a value of $T_{esc} = (67 \pm 8)$ mK. The V(I) characteristics which were measured in section 5.3 at different mixing chamber temperatures showed no qualitative difference within the range [20,300] mK which indicates the possibility of a thermal decoupling between the electron temperature of the device and the bath temperature.

The fluctuation free critical current I_{c0} was calculated by applying the Ambegaokar-Baratoff relation to the extracted superconducting gap $\Delta(T)$. Out of this analysis it be-

came clear that the fluctuation free critical current at $T = 0$ is $I_{c0} \approx 115\,\text{nA}$ and supports the theory of large quantum fluctuations below T_{co}. The extracted value of I_{c0} is also in agreement with the theoretical value of $T_c = 1.3\,\text{K}$.

The extracted critical current of each V(I)-curve showed a temperature independent constant value within the full measured temperature range and only approaches the fluctuation free critical current at around $T = 1.2\,\text{K}$. Although thermal effects are expected to be the dominant type of fluctuations above the cross-over temperature T_{co} ≈95-144 mK, their effect on the temperature dependent critical current was absent. A possible reason for this absence would be the effect of an underdamped phase diffusion as observed by Kivioja et al. [65]. In this scenario, the impedance at ω_p has to be around $1.5\,\text{k}\Omega$. Such a value would be 3 times larger than given by Kivioja et al., furthermore, the analysis of the retrapping current in section 5.3.3 used a best fit with $R(\omega) = 405\,\Omega$ which is a realistic value [1]. By going the reverse way and assuming $R(\omega) = 405\,\Omega$, $I_{c0} = 115\,\text{nA}$ and $Q \approx 4$ to be the correct values, one would need a junction's capacitance of $C_j \approx 270\,\text{fF}$ in order to observe the measured reduction of the critical current. Such a large capacitance is not realistic given by the dimensions of the small Josephson junction. It can therefore be concluded that underdamped phase diffusion is unlikely to be the dominant effect of the I_{c0} reduction.

The measured retrapping current as a function of the mixing chamber temperature was in good agreement with theory with a best fit parameter $R(\omega) = 405\,\Omega$. A bottoming out of the retrapping current at low temperatures to a constant value of $I_{r0} = 71\,\text{pA}$ was expected but the resolution of the used setup was not high enough to confirm this value.

The V(I)-curves did not show any contribution related to Coulomb blockade due to the fact that the tunnel resistance is around a factor two smaller than the quantum resistance $R_Q \approx 6.5\,\text{k}\Omega$, see chapter 1. Furthermore, the total resistance at high frequencies ($\approx \omega_p$) is even lower as the environmental impedance has to be taken into account.

The large standard deviation deviation of the subgap resistance, measured in section 5.2,

might be caused by an additional noise source. Such a noise source could also be responsible for the reduction of the critical current above the cross-over temperature. For example an additional low frequency random current noise affecting the applied bias current could be causing the above mentioned effects. The next chapter will therefore analyse the autocorrelation of the switching events for a Josephson junction. This newly developed technique allows one to get a deeper insight into additional noise sources and its frequency components.

Chapter 6

Pulsed measurement on a Josephson junction and noise analysis

In chapter 5 the switching current distribution was obtained from the recorded V(I)-curves to then extract the bias current at which the Josephson junction switched into the voltage state. This is a time consuming method as a single V(I)-curve can take up to 2 seconds which sums up to 30 minutes if 1000 of them have to be measured. A different method is to apply a series of N current pulses with a constant amplitude I_b, which is close to the expected switching current, and a certain duration Δt. During the time Δt the junction has a certain probability of switching because of thermal or quantum fluctuations. By repetitively applying identical pulses and counting the number of switching events the probability $P(I_b)$ can be determined for a single value of the bias current I_b. Repeating the same measurement for a range of bias currents, the cumulative escape probability can rather quickly be extracted (see section 2.3). Typically, it looks like an S-shaped curve. This pulsed method has a number of advantages over the previous method of collecting I(V) curves, it not only more directly and more quickly determines the probability of escape, but it opens the way to a number of ways of extracting new information about the physics and the environment of the junction, partly because we have access to higher

bandwidth information, as we shall see in this chapter. The technical implementation of the pulsed method is first introduced and discussed and results extracted and analysed. We then develop a new method that uses the calculation of the autocorrelation function of the switching measurements to extract environmental information. In our case we demonstrate that this new technique is particularly useful for uncovering the presence of small unwanted subcritical currents that have so far been hidden and unmeasurable.

6.1 Measurement setup

The wiring and setup inside the dilution refrigerator is the same as described in chapter 5. The main difference is the substitution of room temperature electronics to create and trigger arbitrary pulses and count the number of times the Josephson junction switches into the voltage state. The following section explains the modification needed to perform pulsed measurements.

6.1.1 Current pulse creation

Figure 6.1 shows a diagram of the setup used to measure the cumulative switching probability of the Josephson junction. To create the pulses a function- and arbitrary waveform generator from *Agilent* is used (Model *33250A*). A *LabView* VI was written to define and load such a waveform via a GPIB connection. The generation of the uploaded waveform is triggered by another function generator from *Stanford Research Systems* , Model *DS345* which outputs a continuous rectangular waveform with a $50\,\%$ duty cycle which is compatible to the TTL (transistor-transistor logic) signal with a typical frequency of 400 Hz (i.e. the pulse repetition rate). The voltage waveform is then applied to the $1\,\mathrm{M}\Omega$ bias resistor at room temperature before it is sent to the sample as a current pulse. The bias resistor is chosen to be much larger than the normal state resistance of the tunnel junction (around $2.5\,\mathrm{k}\Omega$) to neglect an additional resistance contribution. The current pulse

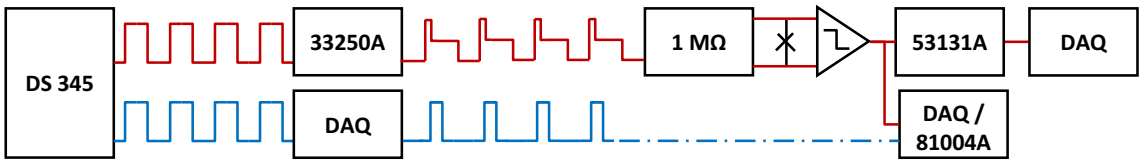

Figure 6.1: Diagram of the setup used to measure the cumulative switching probability of a Josephson junction. Top row: The DS345 triggers the AWG 33250A to create the user defined voltage waveforms which are then transformed by a room temperature bias resistor (1 MΩ) to a current pulse. The voltage response of the junction to this current pulse is then filtered and amplified by a room temperature amplifier before a universal counter 53131A compares it to a set voltage threshold and counts the successful switching events. Bottom row: A second, rectangular waveform is created (blue) in parallel which triggers the DAQ to generate a time delayed pulse. This delayed pulse is used to directly access individual switching/no-switching events to create a binary array. An oscilloscope (*Agilent DSO81004A* with 4 channels, 8 GHz real-time bandwidth with a maximum of 20 GSa/s) can alternatively be connected to simultaneously observe the junction response to the applied current pulse.

is applied to the Josephson junction at the base temperature and its response voltage is low-pass filtered and amplified at room temperature (*Stanford Research Systems (SRS), SR640*) before a universal counter (*Agilent 53131A*) counts the number of successful switches above a set threshold for a set arming time. This setup allows the determination of the number of switching events in a train of, for example, 1000 current bias pulses.

In a later experiment, the output voltage pulses were measured by a DAQ and saved as a binary array of individual switching/no-switching events. In this case, a second, delayed trigger is needed. This trigger is necessary as the junction's response is time delayed to the applied bias current and the DAQ compares the response at this delayed time trigger to a set threshold to then decide if a switching occurred or not (see the second row (blue) in figure 6.1). This delayed trigger (also rectangular, continuous, $50\,\%$ duty cycle and same frequency) is created by using the same TTL signal which triggers the arbitrary waveform generator. Alternatively an oscilloscope is connected to simultaneously observe the junction response to the applied current pulse.

6.1.2 Current pulse calibration

The form of the current pulse shape which is applied to the Josephson junction is shown in the top panel of figure 6.2. The waveform consists of a short rise from zero to the maximum voltage, A, which is then held for a time Δt_p (typically around $200\,\mu s$) before it is reduced to the sustain plateau with voltage B for a duration of Δt_s (typically around $450\,\mu s$). The pulse is then decreased to zero. The repetition rate sets the time period δt_r between two consecutive pulses and it is chosen such that any additional quasi-particle heating can relax before and after the applied current pulse. The sustain plateau makes sure that even when the junction switches at the end of the bias pulse (i.e. later than Δt_p) a measurable voltage will still build up [98]. The amplitude of the sustain is chosen such that no additional switching occurs during this time interval. The bottom panel of figure 6.2 shows the response voltage trace (green and dark blue area) of the junction. These traces enclose a black area which is clear of voltage traces indicating that the sustain plateau keeps the response voltage at a high level but without causing any additional switching events during this time. This allows us to discriminate between switching and non-switching events with high fidelity. The trace was recorded for several thousand pulses and the amplitude of the sustain plateau is set by iteratively ensuring no voltage traces enter the zone required for discrimination.

6.1.3 Low probability switching histogram

Our counting experiments rely on applying a constant bias current close to the critical current for a known time period. However, the applied current pulse has to travel down to the sample and might be distorted by the heavily filtered lines as well as ringing/resonant effects of the high frequency components in the wire. This means that the junction might not be biased with a constant current during the time Δt_p. This can significantly disturb the switching distribution as the junction would mainly switch at one of the peaks of the

distorted pulse. In order to test that the pulse one intends to apply is actually applied, a check can be performed. The switching probability distribution between t and $t + dt$, namely $P(t) = \Gamma \cdot dt \cdot \exp(-\Gamma t)$, in the limit of low biasing currents, has a very low probability $P \ll 1$ [98]. In this limit the switching probability during the time dt is almost constant $P \approx \Gamma t$ as $\Gamma t \ll 1$. By applying a continuous series of pulses with a small amplitude (such that $P \approx const.$) and recording the histogram of switching events, a flat histogram would therefore be expected. The light blue histogram in the bottom panel of figure 6.2 shows the recorded switching distribution during the pulse duration Δt_p. Initially a flat top pulse is chosen as indicated by the blue shape in the top panel of figure 6.3. More than 20000 switching events (with a repetition rate ν_{rep}=400 Hz) are recorded to obtain meaningful statistics of the switching distribution during the duration of the bias current pulse. The extracted normalised histogram of switching events as function of time can be seen in the bottom panel of figure 6.3 as a red curve. These results can now be used to modify the pulse during the interval Δt_p with the aim of achieving a constant switching probability at all times (see red curve in the top panel of figure 6.3). Measuring the histogram for the modified pulse (red line in bottom panel of figure 6.3) shows a much flatter distribution compared to the uncalibrated pulse. A quantitative measure for this improvement is the standard deviation which is $\sigma_{uncal} = 0.20$ for the initial pulse shape and $\sigma_{cal} = 0.11$ for the calibrated pulse. It is possible to iteratively improve the pulse shape but as the recording of the histogram at such low switching probabilities can take up to several hours further improvement was discontinued.

6.1.4 Heating effects given by the repetition rate

The time separation between consecutive pulses is set by the repetition rate of the TTL signal that triggers the arbitrary waveform generator. The bias current switching pulse is set to a duration of Δt_p=200 µs for the following set of measurements. The complete bias current pulse length is the sum of the bias current plateau and the rising and falling

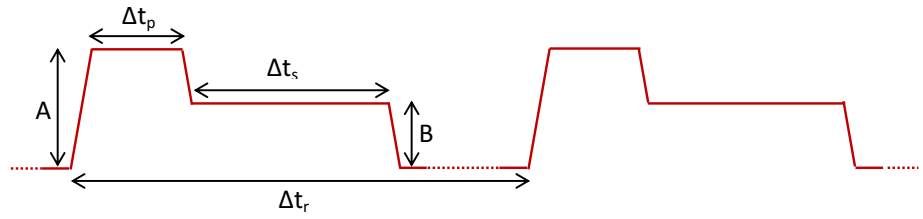

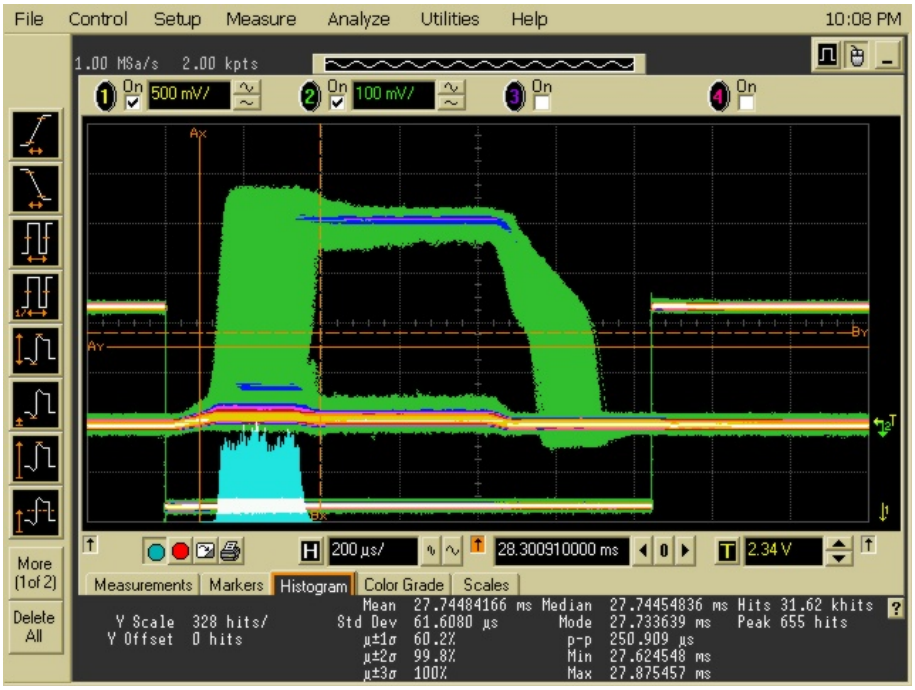

Figure 6.2: Top: Idealised waveform of the bias current pulse. The pulse consists of a short rise from zero to the voltage A which is then held for a time Δt_p before it is reduced to the sustain plateau with amplitude B for a duration of Δt_s. The repetition rate sets the time Δt_r between two consecutive current pulses. Bottom: Time traces of the voltage response (green and dark blue) which was used to set the amplitude of the sustain plateau B and also to set the threshold for the universal counter. No additional switching events occur during the sustain plateau. At the same time the oscilloscopes histogram function records the probability of junction escape as a function of bias current pulse time (light blue).

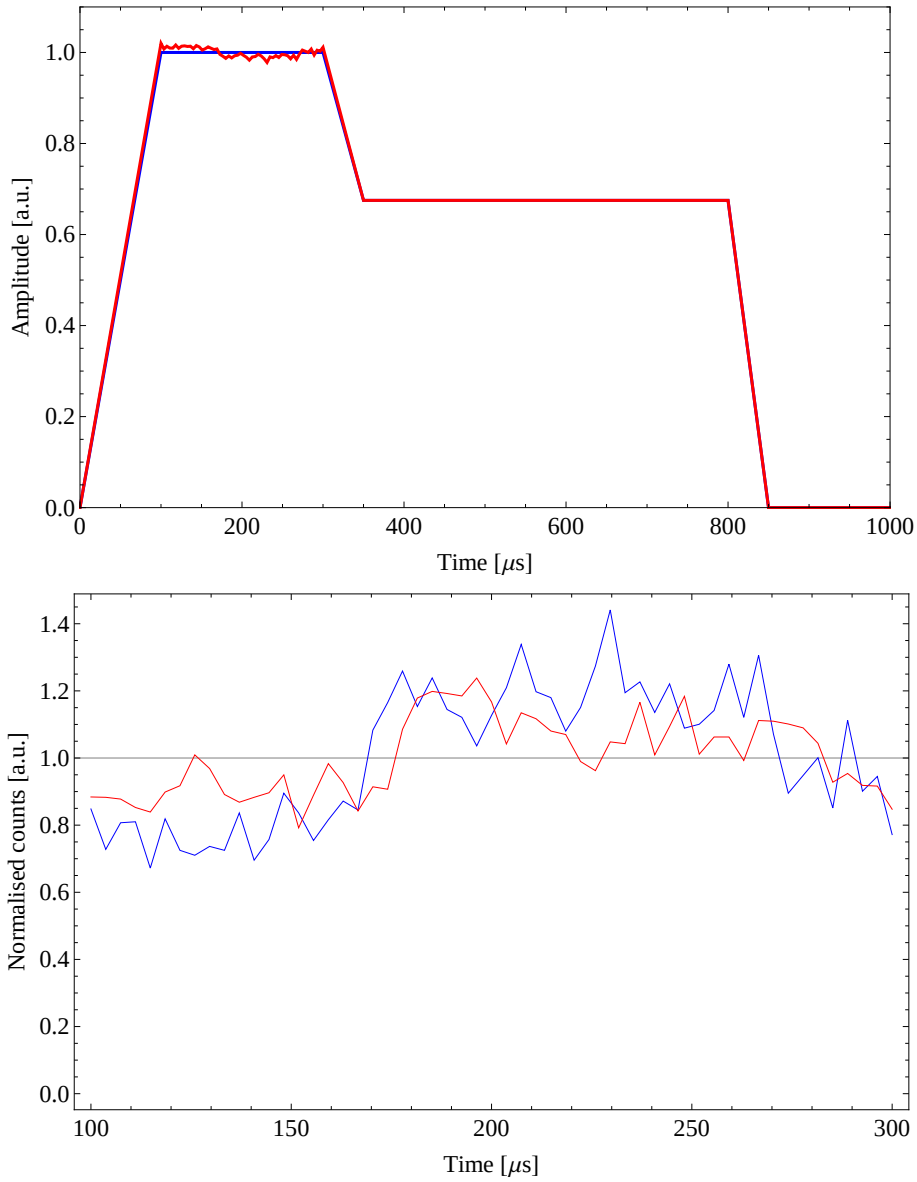

Figure 6.3: Top: Uncalibrated (blue) and calibrated bias current pulse forms (red) after one iteration. The modification is based on flattening the switching current distribution (bottom figure) over the bias current pulse duration. Bottom: Measured histograms of the switching events as a function of time of the bias current pulse. The modified pulse clearly shows a smaller standard deviation.

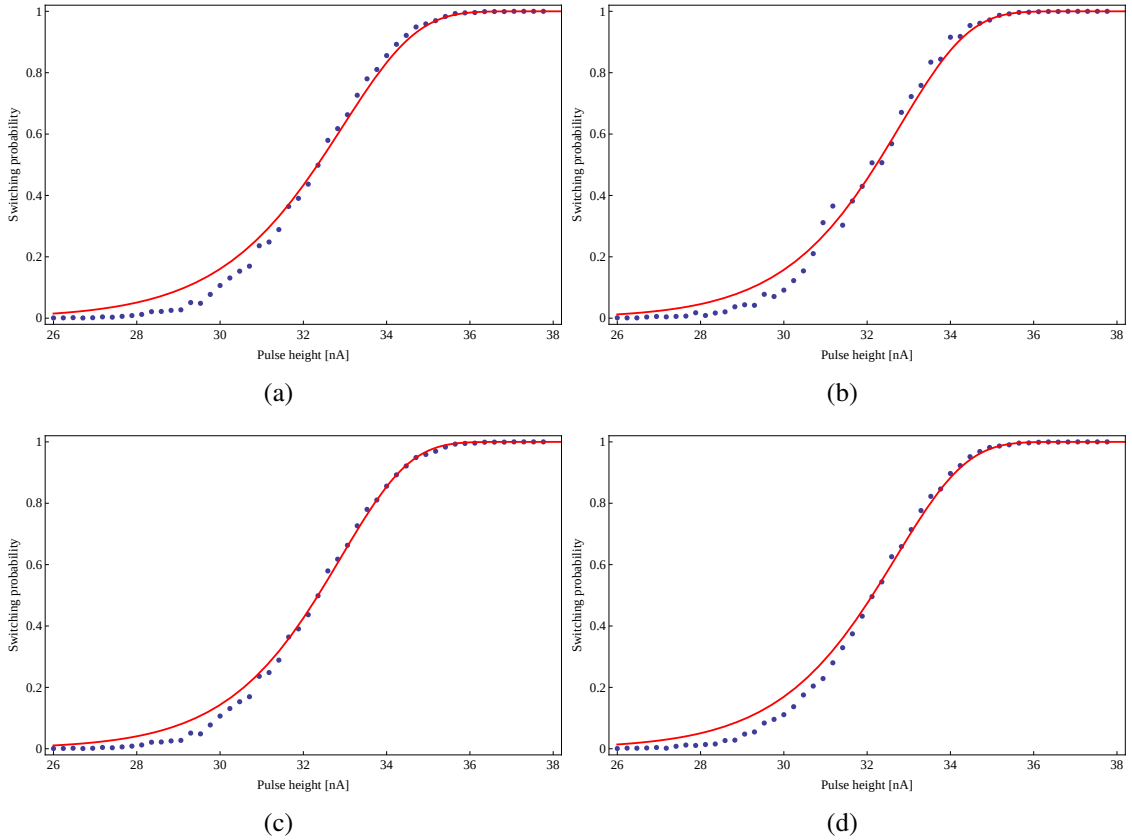

Figure 6.4: Cumulative escape probabilities at different repetition rates ν_{rep} of the pulse series. The red lines are fitting curves to the macroscopic quantum tunneling limit (i.e. $T \ll T_{co}$) with the two fixed parameters R_n=2500 Ω and Δt_p=200 µs. Each point represents the escape probability of 1000 current pulses. The resulting fitting parameters are summarised in table 6.1. a) ν_{rep}=200 Hz. b) ν_{rep}=300 Hz. c) ν_{rep}=400 Hz. d) ν_{rep}=500 Hz.

time (each 100 µs) and the duration of the sustain plateau Δt_s=450 µs which creates a total pulse length of 1 ms. The repetition rate has therefore to be at least smaller than 1000 Hz. Usually a repetition rate of 400 Hz is chosen, leaving 1.5 ms for relaxation of the quasi-particle after a switching event. However, it is possible that this time is too short and that heating in the Josephson junction may occur due to the lack of time for the junction to relax after it switches to the voltage state between two pulses. A simple check can be performed by measuring the cumulative switching probability for different repetition rates. This was done for ν_{rep}=(200, 300, 400, 500) Hz and the resulting cumulative probabilities curves (S-curves) can be seen in figure 6.4. For this set of measurements

ν_{rep}	200 Hz	300 Hz	400 Hz	500 Hz	V(I)
I_{c0} [nA]	(77.3 ± 1.8)	(73.9 ± 2.6)	(73.4 ± 1.8)	(74.5 ± 2.0)	(104 ± 3)
T_{esc} [mK]	(95 ± 11)	(92 ± 12)	(95 ± 11)	(96 ± 12)	(67 ± 8)
C_j [fF]	(28 ± 9)	(32 ± 9)	(33 ± 9)	(31 ± 11)	(79 ± 20)

Table 6.1: Fitting parameters for the red curves in figure 6.4. The escape temperatures are within each others standard error such that no heating can be seen within this error. The far right column lists the values which are extracted from the V(I)-curves of chapter 5.2.2.

the room temperature amplifier is set to a gain of 60 dB with a 25 kHz low-pass filter in front of the amplification. The counter counts successful switching events above a threshold of 150 mV which compares with the theoretical superconducting gap voltage $V_g \approx 1000 \cdot 2\Delta/e$=365 mV. The mixing chamber is stable at 20.6 mK. Each S-curve was measured with a current bias range of 26-38 nA in 50 steps. For each current step 1000 current pulses were applied.

In order to quantify the possible heating effect due to the repetition rate of the bias current pulses, the measured cumulative probability $\tilde{P}$ is inserted into equation (2.63) to extract the fluctuation free critical current I_{c0} and the escape temperature T_{esc} from which the junction capacitance C_j may be determined. All of these values, together with the fixed fitting parameters R_n=2500 Ω and Δt_p =200 µs, are then inserted into the macroscopic quantum tunneling model and plotted as red curves in figure 6.4 which fits well with the measured points (blue dots). A summary of the fitting parameters can be seen in table 6.1. Based on the fitting parameters in Table 6.1 no change in the value of T_{esc} could be observed as a result of changes in the repetition rate, within the error. This indicates that the measurement does not have a significant heating effect on the junction. Note that the junction temperature that matters is that just before a switching event. This result can be compared to the measurement on large Josephson junctions in which so-called *quasi-particle traps* were tested [99]. In the cited paper, the quasiparticle current decayed over a time of around 30 ms which was measured for $Al/Al_2O_3/Al$ Josephson junctions with a critical current of around 40 µA. The quasiparticle current which is created due to the

switching of the junction into the normal state is expected to be proportional to the critical current [99]. As the critical current in the present junction is around 1000 times smaller, a decay of the quasiparticle current in the range of few tens of μs is expected, assuming the decay time of the quasiparticle stays the same. Even the highest applied repetition rate of 500 Hz has a low time of 1 ms which is still long enough to give time to the quasiparticle current to decay.

Although the pulsed measurement reduces the amount of time for which the junction is in the resistive state, the escape temperature is higher than the extracted value from the V(I)-curves. It is not clear what the cause of such an increase in T_{esc} might be. But it confirms the observation that the electron temperature is higher than the bath temperature.

Interestingly the junction capacitance is closer to the expected value of $C_j \approx 20\,\text{fF}$ given by the dimension of the overlap area. Surprisingly, the fluctuation free critical current is smaller than the expected value of $115\,\text{nA}$ and also significantly smaller than the value extracted from the V(I)-curves. It is possible that an additional small dc current was introduced by using a different setup which was needed for the pulsed measurement. Because the cryogenic environment had not changed between the V(I) measurements and the present pulsed measurements, the change in apparent I_{c0} can only be due to one of two effects: 1) the method of measurement and analysis for pulses is not comparable to V(I) measurements for some unknown reason, 2) changes in the room temperature equipment have affected the environment of the junction, for example an additional circulating offset current.

We would consider 2) more likely and it is possible that additional small sub critical currents are circulating in the junction

6.1.5 Temperature dependence of the cumulative switching histogram

Recall that it was, surprisingly, not possible to observe any temperature dependence of the critical current by measuring V(I)-characteristics, as shown by the red dots in figure 5.12.

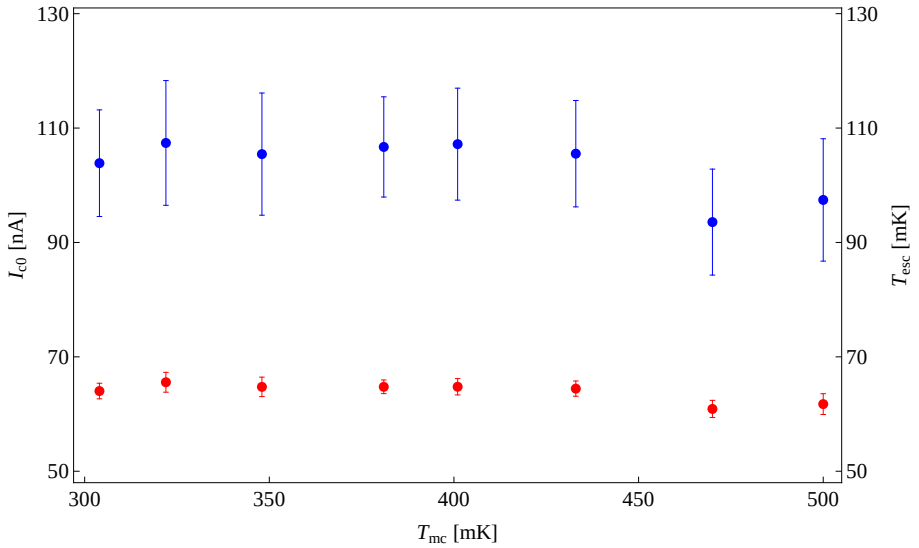

Figure 6.5: The extracted escape temperatures T_{esc} (red dots) and critical currents I_{c0} (blue dots) versus the mixing chamber temperature T_{mc}. Both parameters display temperature independence within the measured temperature range and error bars.

The same independence is therefore expected to be seen when measuring the cumulative switching histogram. This was checked within the temperature range T_{mc}=[300,500] mK in 7 steps comparing the resulting S-curves with the thermal escape model. For this set of measurements the mixing chamber heater was used to increase the temperature. For each temperature, 5 switching curves were measured and averaged. At room temperature a low-pass filter of 15 kHz and a gain of 60 dB was used to read out the voltage response. The bias current range was I_b=[28-60] nA in 50 steps with a counter threshold of 120 mV for 1000 current pulses that build a single point of the S-curve. The reason for using the thermal escape model to fit the measured cumulative probability curves is that the temperature of the sample is higher than the theoretical cross-over temperature T_{co} =99-150 mK. Only the thermal escape model is temperature dependent. The extracted critical currents I_{c0} and escape temperatures T_{esc} from the dataset is plotted in figure 6.5. Both parameters display an independence of the mixing chamber temperature T_{mc} within their errors and it confirms the results obtained by the measurement of V(I)-curves in section 5.2.2 and 5.3.2: A fluctuation free critical current of around $100\,$nA and an escape temperature of

approximately $65\,\mathrm{mK}$.

As the repetition rate is set to ν_{rep} =400 Hz the extracted fitting parameters can be compared to those of table 6.1 for 400 Hz. This clearly shows that the thermal escape model estimates a higher fluctuation free critical current I_{c0} in comparison to the macroscopic quantum tunneling model which was used in figure 6.4. The thermal escape model was also applied to the data in figure 6.4 but similar fitting parameters resulted. This means that the fitting procedure is correct. Furthermore, given the similarity to the results in section 5.2.2, it is unlikely that underdamped phase diffusion is causing the temperature independence, i.e. we might not be observing an intrinsic effect of the Josephson junction. The possibility of an external effect given by the setup is supported by the results above, for example a low frequency current noise which would increase the effective bias current yielding wrong fitting values.

6.2 Autocorrelation for noise detection

As discussed in section 6.1.5, it is possible that an underlying noise term is affecting the switching process and causing the absence of a temperature dependence on the cumulative escape histogram. In order to detect a so far unseen correlation between a time dependent noise signal and the switching process of the Josephson junction it is necessary to record each single switching event. This new technique allows to transform the information into a binary array which lists the switching/no-switching events of the junction for each applied bias current pulse. This binary array contains significantly more information than the cumulative switching probability which only sums up the successful switchings of the junction. The autocorrelation function of this binary array describes how switching events are correlated if they are time separated and it is therefore a powerful tool to extract any repeating patterns which underly the switching process.

6.2.1 Definition of the autocorrelation

There are a variety of definitions of the autocorrelation function in signal processing which mainly differ in the normalisation of the coefficients. Here, we define the autocorrelation for a set of elements $[x_0, x_1, ..., x_{N-1}]$ with $x_j = 0$ for $j < 0$ or $j \geq N$

$$R_j = \frac{1}{(N - |j|) \cdot \sigma^2} \sum_{k=0}^{N-1} (x_k - \overline{x}) \cdot (x_{j+k} - \overline{x}) \tag{6.1}$$

$$\overline{x} = \frac{1}{N} \sum_{k=0}^{N-1} x_k \tag{6.2}$$

$$\sigma^2 = \frac{1}{N-1} \sum_{k=0}^{N-1} (x_k - \overline{x})^2 \tag{6.3}$$

for $j = -(N-1), -(N-2), ..., -1, 0, 1, ..., (N-2), (N-1)$.

The mean value of the array is given by $\overline{x}$. If the variance σ^2 is different from zero, the autocorrelation is well-defined and takes a value within the range $[-1, 1]$, with 1 indicating perfect correlation, -1 indicating perfect anti-correlation and 0 indicating the values are not correlated at all.

6.2.2 Measurement setup

In order to read out the voltage response of the junction after each bias current pulse it is necessary to generate a time delayed trigger relative to pulse triggering signal as shown by the second row in figure 6.1 (blue). This is implemented by using a separate channel of the DAQ which uses the rectangular TTL signal of the DS345 as an input to then create a time delayed output TTL signal which is then fed into the DAQ to read out the voltage response of the junction at this delayed trigger. The delay time is set such that the junction response is measured right at the beginning of the sustain plateau of the current bias pulse, see figure 6.2. This allows the detection of any switching/no-switching event of the junction and transforms it into a binary array by comparing it to a set threshold (150

mV). As before, a *LabView* VI allows to have a full control over the measurement and set all the relevant parameters including the voltage threshold to convert the voltage response of the Josephson junction into a binary array.

6.2.3 Autocorrelation of the switching events

The recorded array $[x_0, x_1, ..., x_{N-1}]$ consists of zeros and ones which are sampled at ν_{rep}. The amplitude of the current pulse is set such that $\overline{x} \approx 0.5$ meaning that around half of the pulses cause a switch of the junction into the normal state. The top panel of figure 6.6 shows the autocorrelation function of the acquired data array as a function of the lag time $j \cong \Delta t$ for ν_{rep}=200 Hz (blue dots), such that the points are separated by 5 ms over a range of 1 s.

The main result of this analysis is the observation of a positive autocorrelation at 50 Hz and multiples of it (shown as gray grid lines the top panel of figure 6.6) which means that the power line frequency is having a significant effect on the switching probability (up to 12% correlation). Another interfering signal can be seen with a frequency of around 8 Hz. The red curve in the same figure tries to fit the 8 Hz noise component and applies the model for an under-damped harmonic oscillator $R(t) = \exp(-2t + c_1) \cdot \sin(2\pi 8t + c_2) + c_3$ with $c_{1,2,3}$ some fitting constants. The same pattern is also observable for the 50 Hz autocorrelation and its amplitude also decreases for larger lag times. It is important to realise that this new technique allows to identify any underlying correlation between switching events which are time separated. Such a pattern can not be detected by just recording V(I)-curves or S-curves which is the standard method for basic diagnostics in these sort of experiments. To extract the frequency components a fast Fourier transformation (FFT)

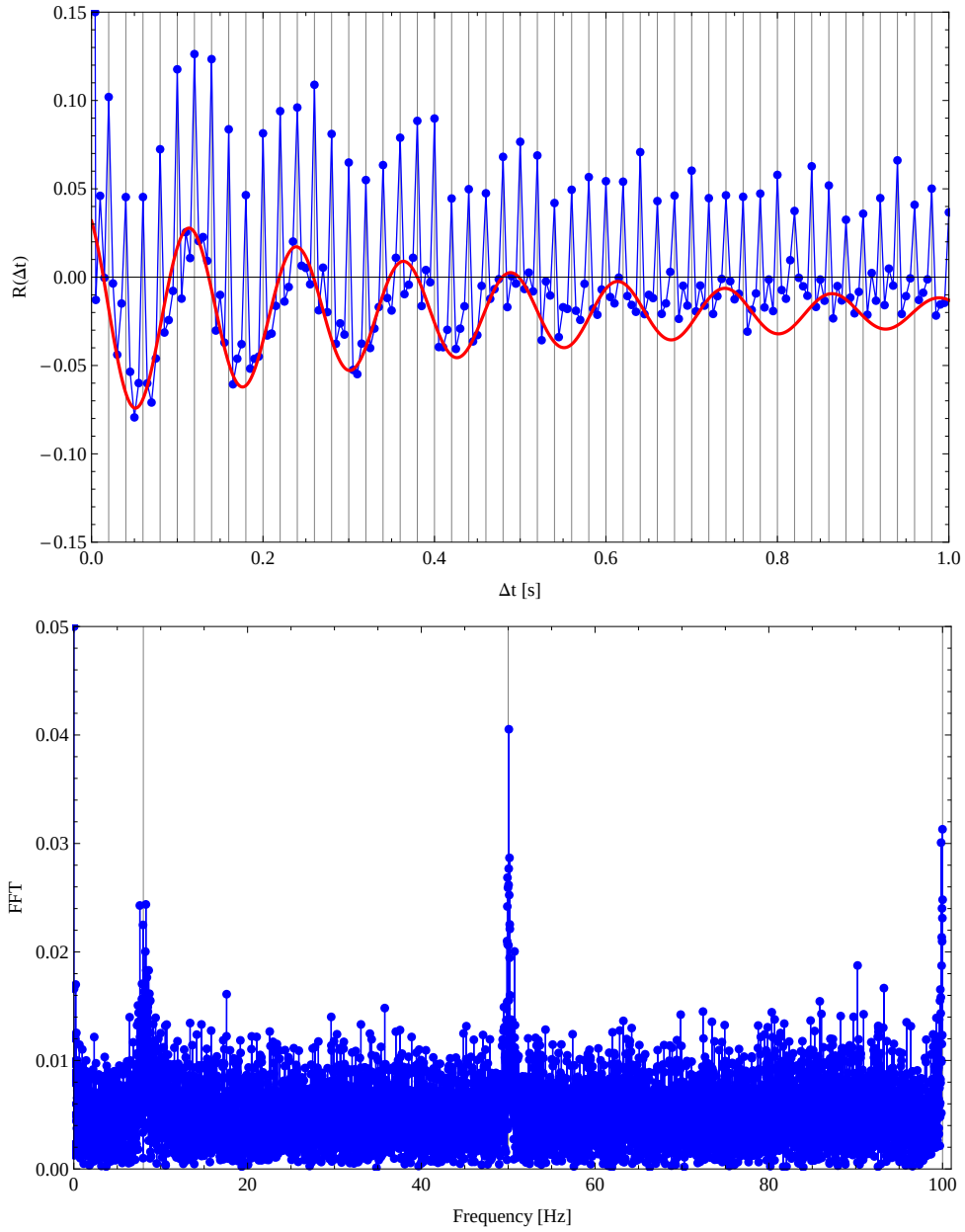

Figure 6.6: Top: Autocorrelation as a function of the time lag (blue dots) clearly showing the 50 Hz signals (gray grid lines). The red curve is fitted to the solution of an under-damped harmonic oscillator with a fundamental frequency of 8 Hz. Bottom: Fast Fourier transformation of the binary switching array showing the frequency spectrum of it. The maximum peaks occur at the characteristic 50 Hz components and also at 8 Hz.

of the binary array was performed

$$|B_0| = |\widetilde{x}_0| / N \tag{6.4}$$

$$|B_k| = \sqrt{2} |\widetilde{x}_k| / N, \qquad k = 1, 2, ..., \lfloor N/2 - 1 \rfloor \tag{6.5}$$

$$\widetilde{x}_k = \sum_{m=0}^{N-1} x_m \cdot \exp(-2\pi\imath km/N), \qquad k = 0, 1, ..., N-1 \tag{6.6}$$

The spectrum of the binary array (bottom panel of figure 6.6) clearly shows a peak at 50 Hz and 100 Hz but also one at 8 Hz, as already expected from the top figure. Notice that a repetition rate ν_{rep}=200 Hz is set but the FFT only goes up to $\nu_{rep}/2$ by the sampling theorem and therefore higher frequency components can only be extracted by using a higher repetition rate. This was done (not shown) for repetition rates up to 400 Hz which showed the expected peaks at multiples of 50 Hz without showing other frequency components. There is an even more interesting measure to look at when changing the repetition rate and that is the first lag autocorrelation R_1 (i.e. equation 6.1 with j=1) as this is closest to the perfect correlation R_0. Figure 6.7 shows R_1 for five different repetition rates and has its maximum at a waiting time of $\tau_w = \pm$ 20 ms between the two consecutive current pulses, which of course corresponds to $\pm$50 Hz. The first lag autocorrelation does not show any sign of a heating effect for higher repetition rates which might be expected if the junction stays in the resistive branch for a too short waiting time between consecutive pulses. From these experiments we conclude that there are subcritical currents derived mainly from mains supply pickup circulating in the junction and also for some unknown reason at 8 Hz (maybe mechanical vibration of the measurement wires). These currents were not evident in any of the previous measures of the junction. It is possible that they affect the values of T_{esc}, I_{c0} and C_j derived in previous experiments. We have therefore developed a new method of detecting experimental measurement problems in the investigation of ultra-small Josephson junctions.

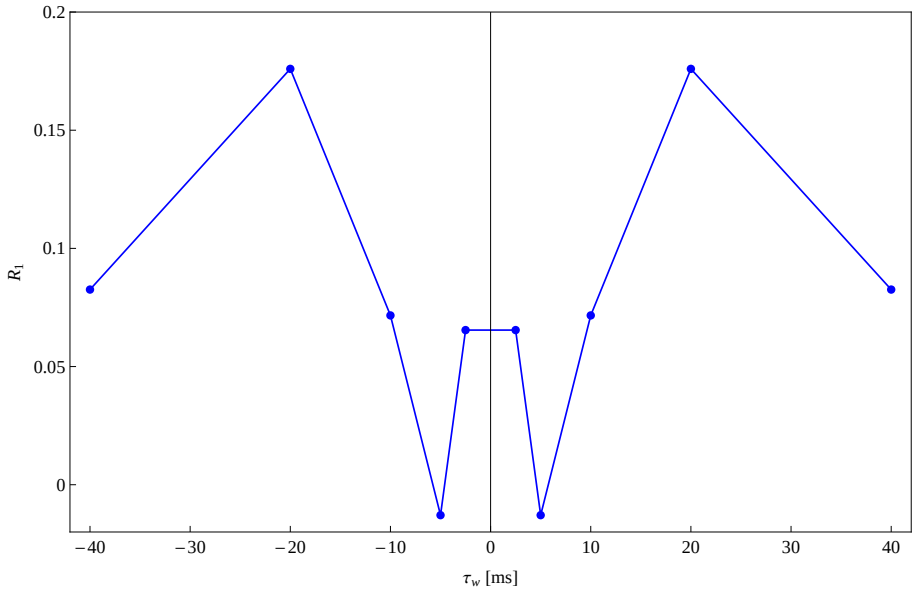

Figure 6.7: First lag autocorrelation as a function of the waiting time between consecutive current pulses. The maximum is reached at ± 20 ms which corresponds to ± 50 Hz. The blue line is shown as a guide to the eye. This calculation can also be used to identify if a heating up of the junction due to the lack of relaxation time between pulses is an issue as an exponential decay of R_1 would be expected.

6.2.4 New real time diagnostic technique

Based on these results a new *LabView* VI was created which calculates the FFT and the autocorrelation in real time for a set time span. It was found that this method is very powerful as one can try to reduce noise sources like changing the grounding of the instruments, reducing electromagnetic emission of nearby instruments or twisting cables and immediately see the effect in those two measures. An improvement was achieved on a different Josephson junction (which is also part of the same chip with $R_n = 3350\,\Omega$ and $C_j \approx 15\,\text{fF}$) and can be measured separately. Note that only in this subsection 6.2.4 the mentioned separate Josephson junction is discussed. Figure 6.8 shows the cumulative escape probability histogram before (blue dots) and after (red dots) resoldering a grounding wire attached to one of the BNC connectors of the leads. This junction was measured at the base temperature of around 20 mK with the same setup as described in section 6.1.

As one can see, the $P = 50\,\%$ point increased by around 6 nA (or $+41\,\%$) and the width

of the S-curve decreased from around 6 nA to less than 2 nA. The blue solid line is a fit to the macroscopic quantum tunneling model with a junction capactiance $C_j = 10\,\text{fF}$ and a fluctuation free critical current $I_{c0} = 77\,\text{nA}$ whereas the blue dashed line represents the thermally activated model with the same values for C_j and I_{c0} but additionally an escape temperature $T_{esc} = 168\,\text{mK}$ was used. The same procedure was applied to the red curves with the following best fit parameters: $C_j = 70\,\text{fF}$, $I_{c0} = 42\,\text{nA}$ and $T_{esc} = 50\,\text{mK}$. The fitted curves in figure 6.8 do not interpolate the measured cumulative escape probabilities well. Nevertheless, the fitting curves show that the effective temperature decreased by almost a factor of 3 as the peaks of the autocorrelation were reduced by resoldering the grounding wire of this specific junction. The extracted junction capacitance on the other hand significantly increased when noise was reduced although the dimension of the junction would suggest a capacitance of around $15\,\text{fF}$. But a higher than expected value for C_j was already observed and discussed by the measured Josephson junction in section 5.2.2. The extracted fluctuation free critical current decreased from $77\,\text{nA}$ to $42\,\text{nA}$ as noise was reduced. This compares to Ambegaokar-Baratoff value at $T = 0$ of $I_{c0} \approx 92\,\text{nA}$ (with $T_c = 1.3\,\text{K}$ and $R_n = 3350\,\Omega$). The decrease in I_{c0} is rather surprising but it shows that current noise affects the S-curve significantly and not just by an additional offset bias current. Nevertheless, the measured switching current at $P = 0.5$ increased by more than 40% and the width of the S-curve simultanously decreased significantly. It was proven that additional currents are circulating in the device that can not be uncovered by the usual techniques but only by the new technique. It is possible to reduce these currents, and this is effectively done by a realtime technqiue. However it was not possible to reduce them to zero and to make quantitative sense to the resulting fits even in the best case that was achieved.

To conclude this section, it was shown that a reduction of $50\,\text{Hz}$ noise in the measurement setup increased the measured switching current at $P = 0.5$ and significantly decreased the width of the cumulative escape probability by effectively reducing the escape tem-

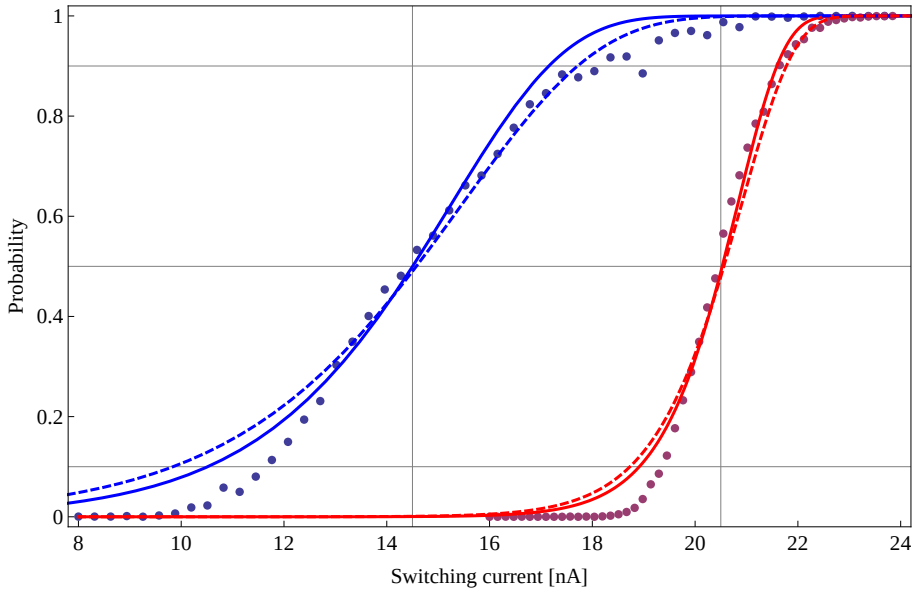

Figure 6.8: The cumulative escape probability histograms of a similar Josephson junction before (blue dots) and after (red dots) resoldering a grounding wire attached to one of the BNC connectors of the leads. The technique of measuring the autocorrelation and FFT was used and finally improved the S-curve. Red solid curve: Fitting to the MQT-regime with the parameters $C_j = 70\,\mathrm{fF}$ and $I_{c0} = 42\,\mathrm{nA}$ whereas the red dashed curve is a fit to the TA-regime with the same fitting parameters plus $T_{esc} = 50\,\mathrm{mK}$. Blue curves: Similar to the red curves but with the best fit parameters $C_j = 10\,\mathrm{fF}$, $I_{c0} = 77\,\mathrm{nA}$ and $T_{esc} = 168\,\mathrm{mK}$. Horizontal grid lines are inserted at P=0.1, 0.5, 0.9 and vertical grid lines at 14.5 nA and 20.5 nA for better visibility.

perature. Applying these observations to the originally measured junction (chapter 5), it could explain the absence of a temperature dependent critical current above T_{co} by an additional current noise which circulates in the measurement setup as observed in section 6.2.3. A low frequency current noise effectively increases the escape temperature without actually heating the Josephson junction, and T_{esc} might be significantly higher than the bath temperature.

This real time diagnostic technique also helped us to choose improved cabling at room temperature to connect the different instruments at room temperature (SMA cables instead of BNC cables are used in the setup).

6.2.5 Characteristics of noise

These methods to identify and uncover noise components and their effects on the switching processes are powerful but they do not help to find directly the sources of noise. This section will begin to address this issue. The resolution of the electronic measuring equipment is also analysed.

The noise spectrum is investigated under varying states of the Josephson junction. To do so, the junction is biased with a constant DC current and the time-resolved voltage response observed. This is done in the superconducting state (i.e. $I_b < I_{c0}$) and also in the normal conducting state (i.e. $I_b > I_{c0}$) of the junction. In order to compare both measured spectra it is necessary to split the voltage response of the junction into a mean value and an additional relative noise term [7]

$$V(t) \quad = \quad \langle V(t) \rangle + \delta V(t) \tag{6.7}$$

where the brackets $\langle \cdot \rangle$ represents the time average.

Table 6.2 lists the relevant values for the noise characterisation in both states of the Josephson junction whereas Δt is the time interval over which the voltage response was recorded

DC current	Samples	Δt	Gain	$\langle V(t)\rangle$	$\sqrt{\langle \delta V(t)^2\rangle}$
$0.0466\,nA$	250000	$1\,s$	$60\,dB$	$2.267\,mV$	$408.254\,\mu V$
$116.6\,nA$	250000	$1\,s$	$60\,dB$	$793.034\,mV$	$408.254\,\mu V$

Table 6.2: Voltage noise characterisation in the superconducting and the normal conducting state.

with a sampling rate of $250\,kHz$. The room temperature amplifier was set to a gain of 60 dB and a low-pass filter of 25 kHz and the mixing chamber is at 20 mK during both measurements. To obtain more information about the frequency contribution of the relative noise term a quantity similar to the autocorrelation of the switching events can be defined. The correlation function for the voltage noise around its mean is described (in time-space) by

$$S_V(t,t') \;=\; 2\,\langle \delta V(t)\cdot \delta V(t')\rangle \tag{6.8}$$

For a stationary mean voltage it is more useful to transform the correlation function in the frequency space which is then called the *noise power spectral density*

$$S_V(f) \;=\; \left|FFT\left(\delta V(t'-t)\right)\right|^2/N^2 \tag{6.9}$$

note that the square-root of $S_V(\omega)$ is called *noise amplitude spectral density* and describes the standard deviation of $\delta V(\omega)$ which is a more relevant measure in this case.

Figure 6.9 shows the noise amplitude spectral density in the frequency interval [0,500] Hz which is calculated from the above recorded voltage response. The spectra obtained for $I_b > I_c$ and $I_b < I_c$ are very similar, there are no additional frequency components occurring nor do the amplitudes of the peaks change. One can therefore conclude that within this frequency range the state of the junction itself does not influence the noise spectrum. In a next step the noise spectrum of the room temperature amplifier was determined by shorting together the two differential inputs. The setup of the amplifier and filtering stays the same as before and one can just measure the output signal by connect-

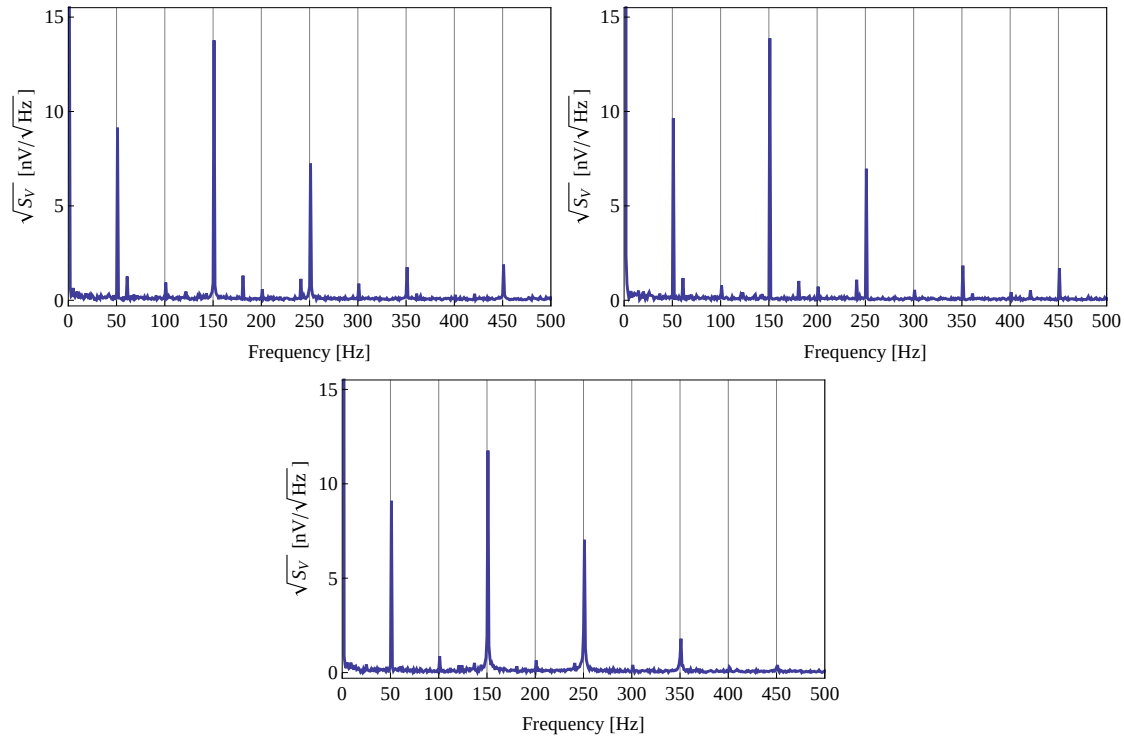

Figure 6.9: Noise amplitude spectral densities. Top left: DC biased in the superconducting state of the junction. Top right: DC biased in the resistive state indicating that state of the junction itself does not have an influence onto the noise spectrum.. Bottom: Noise spectrum of the short circuited amplifier showing that the main contribution to the noise comes from the read-out setup.

ing it to the DAQ board with a sampling rate of 250 kHz. The results can be seen in the lower panel of figure 6.9 with the largest peak at 150 Hz reaching around 11 nV/$\sqrt{Hz}$ which is in good agreement to the manufacturer specified value of 10 nV/$\sqrt{Hz}$ at 60 Hz (note that this is the characteristic power line frequency in the USA) with a gain of 60 dB. To conclude, this amplifier injects mains current noise into the Josephson junction which is a possible candidate for the additional current noise. For a next experiment, a battery powered amplifier should be installed to check this possibility. This was not done yet due to time constrictions. However, simple pickup on the wiring might also be the cause of the noise current in the junction. This also shows how difficult it is to control such noise currents in the nA regime although the measurement setup was carefully build to reduce noise, including low temperature microcoax filters. The measurement of such small Josephson junctions are challenging and the control of the environment is the main difficulty.

6.3 Summary

In this chapter the cumulative switching distribution was measured by applying current pulses. A method was shown to design and calibrate the pulse shape which would be even more important when using very short pulses (in the ns range) as the damping of the leads strongly affects the pulse shape. The absence of a temperature dependence of the switching process lead to the development of a real-time noise analysis method which is based on the autocorrelation calculation of the binary switching array. This method in combination with a Fourier transformation allowed the identification of the frequency components and the strength of the noisy signal. This new technique quickly and easily provides more detailed information about the operation of small Josephson junctions than has been available till now and allowed us to test fixes to the setup in real time.

Chapter 7

Conclusions

The physics of small Josephson junctions shows differences compared to large area junctions. For example, the effect of the low impedance environment near the plasma frequency or the possible appearance of a phase diffusion regime above the cross-over temperature. Although the low temperature regime (i.e. $T < T_{co}$) is dominated by macroscopic quantum tunneling for small and large junctions, the effect on small junctions is larger. The measured critical current was around 3 times lower than the fluctuation free critical current of $I_{c0} \approx 115$ nA at base temperature $T = 17$ mK. The fluctuation free critical current is in agreement with the Ambegaokar-Baratoff relation for an increased critical temperature of $T_c \approx 1.3$ K due to the thickness of the deposited aluminium film. The junction's capacitance was extracted from different measurements to a value of $C_j \approx 65$ fF which is larger than the expected value based on the dimension of the junction's overlap area. The possibility of an additional on-chip capacitance to ground, given by the SiN membrane, was difficult to estimate. The capacitance of the microcoaxial filter is unlikely to affect the effective capacitance of the junction as the filter is outside the corresponding wavelength of the plasma frequency and it would furthermore exceed the total capacitance by far.

The superconducting gap was extracted at $T = 17$ mK from an I(V)-curve and the resulting gap voltage $V_g = 2\Delta(0)/e \approx 400\,\mu$V is in good agreement with the theoretical value

(given $T_c = 1.3\,\mathrm{K}$). The temperature dependence of $\Delta(T)$ was extracted from a set of I(V) characteristic in the range from $17\,\mathrm{mK}$ to $1.1\,\mathrm{K}$ and compares well to the solution of the BCS-theory. At the same time, the critical current of each I(V)-curve was extracted and plotted as a function of temperature and did not show any dependence within the temperature range. The possibility of underdamped phase diffusion was discussed but it was concluded that the effect would be too small. It was later shown that additional low frequency current noise effectively increases the escape temperature of the junction but it is difficult to quantify this effect as the escape process is affected in a more complex way than by just an additional dc offset bias current.

A unique effect of underdamped Josephson junctions is the appearance of a retrapping current. The retrapping current was extracted and plotted as a function of temperature. Comparing this result to theory showed that the environmental impedance has to be taken into account for small junctions. We extracted a resistance at the plasma frequency of around $405\,\Omega$ which is within the range of expected values found in the relevant literature.

The measured subgap resistance was larger than the wiring resistance of the setup and showed an unusual large standard deviation which lead us to the development of a new diagnostic technique to uncover subcritical noise currents in the setup. The new diagnostic technique is based on the measurement of the autocorrelation of the binary switching array data. The presence of these noise currents is not apparent in any measurement of the junctions V(I) characteristic nor in the pulsed cumulative probability measurement. Such noise currents are probably not affecting the measurements of large Josephson junctions due to their high critical currents but they become significant in small area junctions as presented here. Applying this technique with the Josephson junction showed the influence of $50\,\mathrm{Hz}$ and $8\,\mathrm{Hz}$ noise which could not be reduced in this measurement setup. However, performing the same new technique onto a similar junction on the same chip helped to reduce low frequency noise by resoldering a grounding wire. The effect on the cumulative

switching current was significant and mainly decreased the effective escape temperature of the fitted data. Furthermore, the critical current was increased by more than 40%. It is however not simple to calculate the effect of low frequency noise currents on the theoretical escape models as we also observed a change in the junction's capacitance which could not be explained. This means that it is not possible to just add a constant offset current to the bias current as the noise term seems to also alter the effective junction capacitance. The current setup did not allow us to directly measure the junction's capacitance.

Small Josephson junctions are difficult to measure in comparison to larger area junctions due to their small critical currents. The setup used in this thesis to measure such devices was carefully designed and tested. Besides using well shielded cabling and low noise instruments, a microcoax filter was designed and tested at the base temperature to reduce the effect of high frequency noise that arises from a hotter temperature stage and propagates down the experimental wiring. In a next experiment, all efforts to also reduce low frequency current noise should be made. A battery powered low noise amplifier should therefore be installed to further reduce $50\,\mathrm{Hz}$ pickup and a separate sample should be fabricated to directly measure the junction's capacitance by a rf-technique.

Appendix

7.1 Energy levels in the RCSJ model

A fully quantum-mechanical description of the dynamics of a Josephson junctions allows one to calculate the energy levels of it. Thus, the Hamiltonian has to be written down together with the commutation relation of the two conjugate variables [12]

$$H_{JJ} = 4E_c\left(\frac{\hat{q}}{2e} - N_g\right)^2 - E_J\cos\hat{\phi} - \frac{\hbar}{2e}I_b\hat{\phi} \tag{7.1}$$

$$\left[\hat{\phi}, \hat{q}\right] = 2ei \tag{7.2}$$

where N_g is the number of offset charges (or the gate charge number in case of a CPB) and is a continious variable.

The commutation relation (7.2) also allows one to relate the two conjugate variables via $\hat{q} = -2ei\partial_{\hat{\phi}}$. The Hamiltonian reduces to

$$H_{JJ}(I_b = 0) = 4E_c\left(-i\partial_{\hat{\phi}} - N_g\right)^2 - E_J\cos\hat{\phi} \tag{7.3}$$

This is a so called *Mathieu equation* that can be solved analytically in two distinct limits, namely for $E_{\mathrm{J}} \gg E_{\mathrm{C}}$ (tight-binding limit) and for $E_{\mathrm{J}} \ll E_{\mathrm{C}}$ (nearly free-electron limit). In the following the analytical solution is reduced to the calculation of the energy levels

in those two limits. The corresponding wave equations can be found for example in the appendix of [100].

In the tight-binding limit ($E_{\text{J}} \gg E_{\text{C}}$), the cosine term in the Hamiltonian can be approximated by $\cos\hat{\phi} \approx 1 - \hat{\phi}^2/2$, reducing the Hamiltonian to the one of a harmonic oscillator with the following energy levels [12]

$$E_n[q/2e] = E_n^0 + \frac{1}{2}(-1)^{n+1} A_n \cos(\pi q/e) \tag{7.4}$$

$$E_n^0 \equiv \hbar\omega_p \left(n + \frac{1}{2}\right) \tag{7.5}$$

$$A_n \approx \sqrt{\frac{2}{\pi}} E_{\text{C}} \left(\frac{E_{\text{J}}}{2E_{\text{C}}}\right)^{\frac{n}{2}+\frac{3}{4}} \frac{2^{4n+5}}{n!} \exp(-8E_{\text{J}}/\hbar\omega_p) \tag{7.6}$$

The amplitude A_n of the additional cosine term depends exponentially on $-E_J/\hbar\omega_p$ and is therefore very small in the tight-binding regime.

In the opposite limit, i.e. the $E_{\text{J}} \ll E_{\text{C}}$, the Hamiltonian can be rewritten in the charge basis as the charge number N is now the good quantum number

$$H_{JJ} = \sum_{N=-\infty}^{\infty} 4E_c \left(\hat{N} - N_g\right)^2 |N\rangle\langle N| - \frac{E_J}{2}\left(|N\rangle\langle N+1| + |N+1\rangle\langle N|\right) \tag{7.7}$$

$$|\phi\rangle = \frac{1}{\sqrt{2\pi}} \sum_{N=-\infty}^{\infty} e^{i\phi N} |N\rangle \tag{7.8}$$

Equation (7.8) describes the transformation between the phase basis $|\phi\rangle$ and the charge basis $|N\rangle$.In this limit, the energy levels of the Hamiltonian have to be split into two regions of the polarisation charge. The parabolic energy levels in the first region are

$$E_n[q/2e] = 4E_{\text{C}}(q/2e - N_g)^2 \quad for\ \frac{n}{2} < \left|\frac{q}{2e} - N_g\right| < \frac{n+1}{2} \tag{7.9}$$

with an avoided crossing occuring near $\frac{q}{2e} \approx m + \frac{1}{2}$. For simplicity, only the first two energy levels in this region are given analytically as they are of most interest in experiments.

The avoided crossing has a magnitude of E_J for the first two energy levels [12]

$$E_1[q/2e] = E_c + \frac{E_J}{2}\sqrt{1+\left(\frac{2E_c}{E_J}\left(\frac{q}{2e}-\left(m+\frac{1}{2}\right)\right)\right)^2} \; for \; \frac{q}{2e} \approx m+\frac{1}{2} \quad (7.10)$$

$$E_0[q/2e] = E_c - \frac{E_J}{2}\sqrt{1+\left(\frac{2E_c}{E_J}\left(\frac{q}{2e}-\left(m+\frac{1}{2}\right)\right)\right)^2} \; for \; \frac{q}{2e} \approx m+\frac{1}{2} \quad (7.11)$$

Note that the solutions for $E_J = 0$ are free-electron plane waves. With $E_J \neq 0$ they show an avoided crossing of the energy parabolas. The energy level diagram can be seen in figure 1.3 for both limits as a function of the polarisation charge q.

The polarisation charge operator is the canonical conjugate of the phase operator. Thus, they do not commute with each other and they have to satisfy the Heisenberg uncertainty relation. For $E_J \ll E_c$, the corresponding wavefunction is well localised in terms of the phase whereas in the opposite limit, $E_J \gg E_c$, the charge is well localised. A similar distinction can be made for the fluctuations such that $k_B T/\hbar\omega_p$ determines if classical thermal fluctuations or quantum fluctuations play the key role. It is usually difficult to perform a theoretical analysis in the intermediate regime [1, 12].

Bibliography

[1] M. Tinkham. *Introduction to Superconductivity*. Dover Publications, 1996.

[2] J. E. Mooij and Yu V. Nazarov. Superconducting nanowires as quantum phase-slip junctions. *Nature Physics*, 2:169–172, 2006.

[3] O. V. Astafiev, L. B. Ioffe, S. Kafanov, Yu. A. Pashkin, K. Yu. Arutyunov, D. Shahar, O. Cohen, and J. S. Tsai. Coherent quantum phase slip. *Nature*, 282:355–358, 2012.

[4] I. M. Pop, I. Protopopov, F. Lecocq, Z. Peng, B. Pannetier, O. Buisson, and W. Guichard. Measurement of the effect of quantum phase slips in a Josephson junction chain. *Nature Physics*, 10.1038, 2010.

[5] H. K. Onnes. The resistance of pure mercury at helium temperatures. *Commun. Phys. Lab. Univ. Leiden*, 12:120, 1911.

[6] J. Bardeen, L. N. Cooper, and J. R. Schrieffer. Microscopic theory of superconductivity. *Phys. Rev.*, 106:162–164, 1957.

[7] Tero T. Heikkilä. *The Physics of Nanoelectronics*. Oxford Master Series in Physics. OUP Oxford, February 2013.

[8] J. Pekola, R. Schoelkopf, and J. Ullom. Cryogenics on a chip. *Physics Today*, 57:41–47, 2004.

[9] M. M. Leivo, J. P. Pekola, and D. V. Averin. Efficient Peltier refrigeration by a pair of normal metal/insulator/superconductor junctions. *Applied Physics Letters*, 68:1996–1998, 1996.

[10] B. D. Josephson. Possible new effects in superconductive tunnelling. *Physics Letters*, 1:251–253, 1962.

[11] J. Clarke. SQUIDs. *Scientific American*, August:46–53, 1994.

[12] K. K. Likharev and A. B. Zorin. Theory of the Bloch-wave oscillations in small Josephson junctions. *Journal of Low Temperature Physics*, 59:347–382, 1985.

[13] J. Kohlmann and R. Behr. *Superconductivity - Theory and Applications, Chapter 11*. InTech, July 2011.

[14] J. P. Pekola and F. W. J. Hekking. Normal-metal-superconductor tunnel junction as a Brownian refrigerator. *Phys. Rev. Lett.*, 98:210604, 2007.

[15] J. T. Peltonen, M. Helle, A. V. Timofeev, P. Solinas, F. W. J. Hekking, and J. P. Pekola. Brownian refrigeration by hybrid tunnel junctions. *Phys. Rev. B*, 84:144505, 2011.

[16] F. Giazotto, T. T. Heikkilä, A. Luukanen, A. M. Savin, and J. P. Pekola. Opportunities for mesoscopics in thermometry and refrigeration: Physics and applications. *Rev. Mod. Phys.*, 78:217, 2006.

[17] F. Giazotto, T. T. Heikkilä, A. Luukanen, A. M. Savin, and J. P. Pekola. Erratum: Opportunities for mesoscopics in thermometry and refrigeration: Physics and applications. *Rev. Mod. Phys.*, 81:1351, 2009.

[18] J. P. Pekola, J. J. Vartiainen, M. Möttönen, O. P. Saira, M. Meschke, and D. V. Averin. Hybrid single-electron transistor as a source of quantized electric current. *Nature Physics*, 4:120–124, 2008.

[19] Wikipedia. Bloch sphere, April 2013.

[20] J. Q. You and F. Nori. Atomic physics and quantum optics using superconducting circuits. *Nature Review*, 474:589–597, 2011.

[21] J. Clarke and F. K. Wilhelm. Superconducting quantum bits. *Nature Physics*, 453:1031–1042, 2008.

[22] Y. Nakamura, Yu. A. Pashkin, and J. S. Tsai. Coherent control of macroscopic quantum states in a single-Cooper-pair box. *Nature Physics*, 398:786–788, 1999.

[23] V. E. Manucharyan, J. Koch, L. I. Glazman, and M. H. Devoret. Fluxonium: Single Cooper-pair circuit free of charge offsets. *Science*, 326:113–116, 2009.

[24] J. R. Friedman, V. Patel, W. Chen, S. K. Tolpygo, and J. E. Lukens. Quantum superposition of distinct macroscopic states. *Nature Physics*, 406:43–46, 2000.

[25] C. H. van der Wal, A. C. J. ter Haar, F. K. Wilhelm, R. N. Schouten, C. J. P. M. Harmans, T. P. Orlando, Seth Lloyd, and J. E. Mooij. Quantum superposition of macroscopic persistent-current states. *Science*, 290:773–777, 2000.

[26] J. M. Martinis, S. Nam, J. Aumentado, and C. Urbina. Rabi oscillations in a large Josephson-junction qubit. *Phys. Rev. Lett.*, 89:117901, 2002.

[27] M. Fox. *Quantum Optics. An Introduction.* Oxford master series in atomic, optical and laser physics. Oxford University Press, 2006.

[28] H. Paik, D. I. Schuster, L. S. Bishop, G. Kirchmair, G. Catelani, A. P. Sears, B. R. Johnson, M. J. Reagor, L. Frunzio, L. I. Glazman, S. M. Girvin, M. H. Devoret, , and R. J. Schoelkopf. Observation of high coherence in Josephson junction

qubits measured in a three-dimensional circuit QED architecture. *Phys. Rev. Lett.*, 107:240501, 2011.

[29] C. Rigetti, J. M. Gambetta, S. Poletto, B. L. T. Plourde, J. M. Chow, A. D. Córcoles, J. A. Smolin, S. T. Merkel, J. R. Rozen, G. A. Keefe, M. B. Rothwell, M. B. Ketchen, and M. Steffen. Superconducting qubit in a waveguide cavity with a coherence time approaching 0.1 ms. *Phys. Rev. B*, 86:100506, 2012.

[30] G. E. Moore. Cramming more components onto integrated circuits. *Electronics*, 38:8, 1965.

[31] R. P. Feynman. Simulating physics with computers. *International Journal of Theoretical Physics*, 21:467–488, 1982.

[32] D. Deutsch. Quantum theory, the Church-Turing principle and the universal quantum computer. *Proc. R. Soc. Lond. A*, 400:97–117, 1985.

[33] P. W. Shor. Algorithms for quantum computation: discrete logarithms and factoring. *Proceedings of the 35th Annual Symposium on Foundations of Computer Science (Shafi Goldwasser, ed.), IEEE Computer Society Press*, pages 124–134, 1994.

[34] L. K. Grover. A fast quantum mechanical algorithm for database search. *Proceedings of 28th Annual ACM Symposium on Theory of Computing (STOC)*, pages 212–219, 1996.

[35] L. M. K. Vandersypen, M. Steffen, G. Breyta, C. S. Yannoni, M. H. Sherwood, and I. L. Chuang. Experimental realization of Shor's quantum factoring algorithm using nuclear magnetic resonance. *Nature Physics*, 414:883–887, 2001.

[36] A. Wallraff, D. I. Schuster, A. Blais, L. Frunzio, R.-S. Huang, J. Majer, S. Kumar, S. M. Girvin, and R. J. Schoelkopf. Strong coupling of a single photon to a super-

conducting qubit using circuit quantum electrodynamics. *Nature*, 431:162–167, 2004.

[37] I. Chiorescu, Y. Nakamura, C. J. P. M. Harmans, and J. E. Mooij. Coherent quantum dynamics of a superconducting flux qubit. *Science*, 299:1869–1871, 2003.

[38] H. Nyquist. Thermal agitation of electric charge in conductors. *Phys. Rev.*, 32:110–113, 1928.

[39] H. B. Callen and T. A. Welton. Irreversibility and generalized noise. *Phys. Rev.*, 83:34–40, 1951.

[40] B. Reulet, J. Senzier, and D. E. Prober. Environmental effects in the third moment of voltage fluctuations in a tunnel junction. *Phys. Rev. Lett.*, 91:196601, 2003.

[41] Yu. Bomze, G. Gershon, D. Shovkun, L. S. Levitov, and M. Reznikov. Measurement of counting statistics of electron transport in a tunnel junction. *Phys. Rev. Lett.*, 95:176601, 2005.

[42] B. Reulet, J. Gabelli, L. Spietz, and D.E. Prober. *Perspectives of Mesoscopic Physics*. World Scientific, 2010.

[43] V. Ambegaokar and A. Baratoff. Tunneling between superconductors. *Phys. Rev. Lett.*, 10:486–489, 1963.

[44] V. Ambegaokar and A. Baratoff. Tunneling between superconductors (erratum). *Phys. Rev. Lett.*, 11:104–104, 1963.

[45] A. T. Johnson, C. J. Lobb, and M. Tinkham. Effect of leads and energy gap upon the retrapping current of Josephson junctions. *Phys. Rev. Lett.*, 65:1263–1266, 1990.

[46] M. H. Devoret, D. Esteve, H. Grabert, G.-L. Ingold, H. Pothier, and C. Urbina. Effect of the electromagnetic environment on the Coulomb blockade in ultrasmall tunnel junctions. *Phys. Rev. Lett.*, 64:15, 1990.

[47] G. L. Ingold and Y. V. Nazarov. *Charge Tunneling Rates in Ultrasmall Junctions*. Plenum Press, New York, 1992.

[48] G.-L. Ingold and H. Grabert. Cooper-pair current through ultrasmall Josephson junctions. *Phys. Rev. B*, 50:395–402, 1994.

[49] H. Grabert and G.-L. Ingold. Mesoscopic Josephson effect. *Superlattices and Microstructures*, 25:915–923, 1994.

[50] A. O. Caldeira and A. J. Leggett. Quantum tunnelling in a dissipative system. *Annals of Physics*, 149:374–456, 1983.

[51] U. Weiss. *Quantum dissipative systems*. World Scientific Publishing Company, 2008.

[52] Yu. M. Ivanchenko and L. A. Zil'berman. Destruction of Josephson current by fluctuations. *JETP Letters*, 8:113–115, 1968.

[53] L. S. Kuzmin, Yu. V. Nazarov, D. B. Haviland, P. Delsing, and T. Claeson. Coulomb blockade and incoherent tunneling of Cooper pairs in ultrasmall junctions affected by strong quantum fluctuations. *Phys. Rev. Lett.*, 67:1161–1164, 1991.

[54] M. Watanabe and D. B. Haviland. Quantum effects in small-capacitance single Josephson junctions. *Phys. Rev. B*, 67:094505, 2003.

[55] H. A. Kramers. Brownian motion in a field of force and the diffusion model of chemical reactions. *Physica*, 7 (4):284–304, 1940.

[56] A. Wallraff, A. Lukashenko, C. Coqui, A. Kemp, T. Duty, and A. V. Ustinov. Switching current measurement of large area Josephson tunnel junctions. *Review of scientific instruments*, 74:8, 2003.

[57] V. Ambegaokar and B. I. Halperin. Voltage due to thermal noise in the dc Josephson effect. *Phys. Rev. Lett.*, 22:1364–1366, 1969.

[58] R. L. Kautz and J. M. Martinis. Noise-affected I-V curves in small hysteretic Josephson junctions. *Physical Review B*, 42 (16), 1990.

[59] H. Grabert, G. L. Ingold, and B. Paul. Phase diffusion and charging effects in Josephson junctions. *Europhysics Letters*, 44, 1998.

[60] A. Steinbach, P. Joyez, A. Cottet, D. Esteve, M. H. Devoret, M. E. Huber, , and John M. Martinis. Direct measurement of the Josephson supercurrent in an ultra-small Josephson junction. *Phys. Rev. Lett.*, 87:137003, 2001.

[61] R. F. Voss and R. A. Webb. Macroscopic quantum tunneling in 1-um nb Josephson junctions. *Phys. Rev. Lett.*, 47:265–268, 1981.

[62] M. H. Devoret, J. M. Martinis, and J. Clarke. Measurements of macroscopic quantum tunneling out of the zero-voltage state of a current-biased Josephson junction. *Phys. Rev. Lett.*, 55:1908–1911, 1985.

[63] T. A. Fulton and L. N. Dunkleberger. Lifetime of the zero-voltage state in Josephson tunnel junctions. *Phys. Rev. B*, 9:4760–4768, 1974.

[64] H. Grabert and U. Weiss. Crossover from thermal hopping to quantum tunneling. *Physical Review Letters*, 53:1787–1790, 1984.

[65] J. M. Kivioja, T. E. Nieminen, J. Claudon, O. Buisson, F. W. J. Hekking, and J. P. Pekola. Observation of transition from escape dynamics to underdamped phase diffusion in a Josephson junction. *Phys. Rev. Lett.*, 94:247002, 2005.

[66] D. Vion, M. Goetz, P. Joyez, D. Esteve, and M. H. Devoret. Thermal activation above a dissipation barrier: Switching of a small Josephson junction. *Phys. Rev. Lett.*, 77:3435–3438, 1996.

[67] D. Vion, A. Aassime, A. Cottet, P. Joyez, H. Pothier, C. Urbina, D. Esteve, and M. H. Devoret. Manipulating the quantum state of an electrical circuit. *Science*, 296:886–889, 2002.

[68] I. Chiorescu, P. Bertet, K. Semba, Y. Nakamura, C. J. P. M. Harmans, and J. E. Mooij. Coherent dynamics of a flux qubit coupled to a harmonic oscillator. *Nature*, 431:159–162, 2004.

[69] J. M. Martinis and R. L. Kautz. Classical phase diffusion in small hysteretic Josephson junctions. *Physical Review Letters*, 63 (14), 1989.

[70] Y. Yoon, S. Gasparinetti, M. Möttönen, and J. Pekola. Capacitively enhanced thermal escape in underdamped Josephson junctions. *Journal of Low Temperature Physics*, 163:164–169, 2011.

[71] G.J. Dolan and J.H. Dunsmuir. Very small (>= 20 nm) lithographic wires, dots, rings, and tunnel junctions. *Physica B: Condensed Matter*, 152:7–13, 1998.

[72] J. M. Martinis, K. B. Cooper, R. McDermott, M. Steffen, M. Ansmann, K. D. Osborn, K. Cicak, S. Oh, D. P. Pappas, R. W. Simmonds, and Clare C. Yu. Decoherence in Josephson qubits from dielectric loss. *Phys. Rev. Lett.*, 95:210503, 2005.

[73] I. M. Pop, T. Fournier, T. Crozes, F. Lecocq, I. Matei, B. Pannetier, O. Buisson, and W. Guichard. Fabrication of stable and reproducible submicron tunnel junctions. *Journal of Vacuum Science and Technology B*, 30, 2012.

[74] MicroChem. *LOR and PMGI Resists Datasheet*.

[75] MicroChem. *Microposit S1800 series photo resists Datasheet*.

[76] K. W. Vogt, P. A. Kohl, W. B. Carter, R. A. Bell, and L. A. Bottomley. Characterization of thin titanium oxide adhesion layers on gold: resistivity, morphology, and composition. *Surface Science*, 301:203–213, 1993.

[77] H. Hieber. Aging properties of gold layers with different adhesion layers. *Thin Solid Films*, 37:335–343, 1976.

[78] L. Frunzio, A. Wallraff, D. Schuster, J. Majer, and R. Schoelkopf. Fabrication and characterization of superconducting circuit QED devices for quantum computation. *IEEE transactions on applied superconductivity*, 15:860–863, 2005.

[79] N. Devlin and D. Brown. Dose determinaiton using ZEP520A resist as a model. Technical report, Nanotechnology Research Center, Georgia Institute of Technology, 2010.

[80] G. J. Dolan. Offset masks for liftoff photoprocessing. *Applied Physics Letters*, 31:337, 1977.

[81] J. Niemeyer and V. Kose. Observation of large dc supercurrents at nonzero voltages in Josephson tunnel junctions. *Applied Physics Letters*, 29:380, 1976.

[82] Wu Yu-Lin, Deng Hui, Yu Hai-Feng, Xue Guang-Ming, Tian Ye, Li Jie, Chen Ying-Fei, Zhao Shi-Ping, and Zheng Dong-Ning. Fabrication of Al/AlOx/Al Josephson junctions and superconducting quantum circuits by shadow evaporation and a dynamic oxidation process. *Chin. Phys. B*, 22:060309, 2013.

[83] C. N. Lau, N. Markovic, M. Bockrath, A. Bezryadin, and M. Tinkham. Quantum phase slips in superconducting nanowires. *Physical Review Letters*, 87(217003), 2001.

[84] W. Guichard and F. W. J. Hekking. Phase-charge duality in Josephson junction circuits: Role of inertia and effect of microwave irradiation. *Phys. Rev. B*, 81:064508, 2010.

[85] S. Corlevi. *Quantum effects in nanoscale Josephson junction circuits*. PhD thesis, KTH Stockholm, 2006.

[86] Frank Pobell. *Matter and Methods at Low Temperatures*. Springer, 2007.

[87] G. White and P. Meeson. *Experimental Techniques in Low-Temperature Physics*. OUP Oxford, 2002.

[88] www.cryoconcept.com, 2012.

[89] A. B. Zorin. The thermocoax cable as the microwave frequency filter for single electron circuits. *Rev. Sci. Instrum.*, 66, 1995.

[90] John M. Martinis, Michel H. Devoret, and John Clarke. Experimental tests for the quantum behavior of a macroscopic degree of freedom: The phase difference across a Josephson junction. *Phys. Rev. B*, 35:4682–4698, 1987.

[91] D. Vion, P. F. Orfila, P. Joyez, D. Esteve, and M. H. Devoret. Miniature electrical filters for single electron devices. *J. Appl. Phys.*, 77:2519, 1995.

[92] C. Y. Ho and T. K. Chu. Electrical resistivity and thermal conductivity of nine selected AISI stainless steels, CINDAS report 45. Technical report, American Iron and Steel Institute, 1977.

[93] F. C. Wellstood, C. Urbina, and J. Clarke. Hot-electron effects in metals. *Phys. Rev. B*, 49:9, 1994.

[94] J. T. Muhonen, M. Meschke, and J. P. Pekola. Micrometre-scale refrigerators. *Rep. Prog. Phys.*, 75:046501, 2012.

[95] F. Gross, B. S. Chandrasekhar, D. Einzel, K. Andres, P. J. Hirschfeld, H. R. Ott, J. Beuers, Z. Fisk, and J. L. Smith. Anomalous temperature dependence of the magnetic field penetration depth in superconducting UBe13. *Z. Phys. B*, 64:175–188, 1986.

[96] P. N. Chubov, V. V. Eremenko, and Yu. A. Pilipenko. Dependence of the critical temperature and energy gap on the thickness of superconducting aluminium films. *Soviet Physics JETP*, 28:389–395, 1969.

[97] M. Iansiti, Qing Hu, R.M. Westervelt, and M. Tinkham. Noise and chaos in a fractal basin boundary regime of a Josephson junction. *Phys. Rev. Lett.*, 55:746–749, 1985.

[98] Quentin Le Masne. *Asymmetric current fluctuations and Andreev states probed with a Josephson junction*. PhD thesis, Research Group in Quantum Electronics, CEA-Saclay, France, 2009.

[99] K. M. Lang, S. Nam, J. Aumentado, C. Urbina, and John M. Martinis. Banishing quasiparticles from Josephson-junction qubits: Why and how to do it. *IEEE Transactions on applied superconductivity*, 13:989–993, 2003.

[100] J. Koch, T. M. Yu, J. Gambetta, A. A. Houck, D. I. Schuster, J. Majer, A. Blais andM. H. Devoret, S. M. Girvin, and R. J. Schoelkopf. Charge-insensitive qubit design derived from the Cooper pair box. *Phys. Rev. A*, 76:042319, 2007.